Monitoring in-situ processing of solid surfaces with real-time x-ray photoelectron spectroscopy

Thesis

Submitted to

The University of Wales, Aberystwyth

by

Gruffudd Trefor Williams MPhys (Hons)

in candidature for the degree of

Doctor of Philosophy (PhD)

2011

Declaration

This work has not previously been accepted in substance for any degree and is not being concurrently submitted in candidature for any degree.

Signed ..... (candidate)

Date .....

Statement 1

This thesis is the result of my own investigations, except where otherwise stated. Where correction services have been used the extent and nature of the correction is clearly marked in a footnote(s).

Other sources are acknowledged by footnotes giving explicit references. A bibliography is appended.

Signed ..... (candidate)

Date .....

Statement 2

I hereby give consent to my thesis, if accepted, to be made available for photocopying and for inter-library loan, and for the title and summary to be made available to outside organisations.

Signed ..... (candidate)

Date .....

Acknowledgements

First and foremost I should like to thank my supervisor, Prof. Andrew Evans, for providing an interesting research topic and for all the guidance and encouragement during my time at Aberystwyth. Secondly I should like to thank Dr. Stephen Evans for many invaluable discussions on all matters in this work and Dr. Martin Allen of the University of Canterbury, New Zealand, for providing the zinc oxide samples and for an enjoyable week working together. Thirdly I should like to thank Research Technician Mr. Mathew Gunn, Mr. David Francis and Mr. John Parry of the mechanical workshop, and Mr. Les Dean and Mr. David Lewis of the electronic workshop for their support during the research. Finally I should like to thank my co-workers during my time at Aberystwyth, Dr. Owain Roberts, Dr. Geraint Jones, Dr. Andrew McGlynn and Mr. Simon Cooil.

I should like to acknowledge the following funding sources; University of Wales Postgraduate Research Scholarship, Aberystwyth University Gooding Fund, Centre for Advanced Functional Materials and the Institute of Physics Research Student Conference Funds.

Abstract

This thesis details the use of x-ray photoelectron spectroscopy to monitor in-situ surface processing of solid surfaces in real-time. The processing methods investigated were annealing, deposition of thin organic films and exposure to oxygen and hydrogen produced by in-situ microwave plasmas. Three solid surfaces were investigated; metals, diamond and zinc oxide.

Clean copper and gold were annealed up to 1000 K while monitoring with real-time XPS. A temperature-dependent shift of the Cu $2p_{3/2}$ and Au $4f_{7/2}$ core-level to lower binding energy was measured, -1.29 ± 0.04 meV / 10 K and -2.36 ± 0.01 meV / 10 K respectively. The shift was identified as being due to a thermal expansion of the lattice. The removal of argon ion induced damage to the copper surface was monitored in real-time and a critical temperature of 680 ± 20 K for the removal of the damage was measured. The formation of an interface between aluminium and copper phthalocyanine was monitored in real-time.

Hydrogen and oxygen terminated (111) natural diamond surfaces were prepared in-situ and surface reconstruction by annealing up to 1200 K was monitored in real-time. Large reversible shifts to core-level binding energies were attributed to a surface photovoltage that was persistent at high temperature on the hydrogen and oxygen terminated surfaces. A model of the surface photovoltage is given where the bulk resistance of the diamond is identified as sustaining the photovoltage at elevated temperature.

The zinc oxide (0001) surface was found to have a temperature-dependent core-level binding energy shift that was fully reversible up to 900 K and symmetric with cooling. The shift was attributed to a diffusion of oxygen vacancies from the bulk into the sub-surface. The zinc oxide $(000\bar{1})$ surface was found to exhibit different temperature dependence to the (0001) surface that was fully reversible up to 700 K but not symmetric with cooling. The shift was attributed to an additional disruption to stabilizing charge transfer between the polar surfaces. The formation of interfaces between the (0001) surface with copper phthalocyanine and C60 were monitored in real-time.

Publications

Langstaff DP, Roberts OR, **Williams GT**, Evans DA, *A system for real-time in-situ photoelectron spectroscopy*, Diamond Light Source Proceedings, **1**, e111, (2011)

Evans DA, Roberts OR, **Williams GT**, Langstaff DP, *Characterisation of organic semiconductor growth using real-time electron spectroscopy*, MRS Proceedings, **1318**, mrsf10-1318-uu09-05, (2011)

Evans DA, Vearey-Roberts AR, Roberts OR, Brieva AC, Bushell A, **Williams GT**, Langstaff DP, Cabailh G, McGovern IT, *Real-time monitoring of the evolving morphology and molecular structure at an organic-inorganic semiconductor interface : SnPc on GaAs (001)*, Journal of Vacuum Science and Technology B, **28**, 4, C5F5-C5F11, (2010)

Evans DA, Roberts OR, **Williams GT**, Vearey-Roberts AR, Bain F, Evans S, Langstaff DP, Twitchen DJ, *Diamond metal contacts : interface barriers and real-time characterisation*, Journal of Physics Condensed Matter, **21**, 36, 364223, (2009)

Table of Contents

1. Introduction

Understanding solid surfaces has underpinned materials physics for generations and although surface science today has evolved into the study of solid-liquid and liquid-gas interfaces [1-4], understanding solid surfaces is as relevant today as it ever has been.

Materials engineers are interested in improving materials and this is often done by some form of processing. This may be annealing the material, alloying of metals, doping of semiconductors, reaction of surfaces with activated gases or the addition of thin films. For the engineer a prior knowledge of the processing is required and this is often supplied by the surface scientist through extensive investigations with a myriad of techniques, a small example of which are photoelectron spectroscopy, diffraction and scanning tunnelling microscopy [5]. However surface science techniques are difficult due to experimental constraints such as the need to move the solid surfaces outside the vacuum for processing and between vacuum chambers for measuring, and are also aimed at static surfaces where measurements are taken before and after surface processing. The effect of exposure to the ambient is highly important to consider when undertaking surface science and this is illustrated in Figure 1.1 which shows a metal surface having been exposed to air. A thick level of contamination has developed consisting of an oxide layer, absorbed water, organic contamination and adsorbed gases. This level of contamination is a major problem as the metal surface is completely obscured by the contamination and surface science techniques will probe the contamination rather than the actual surface. The development of a system capable of performing surface processing and measuring in the same environment is therefore required.

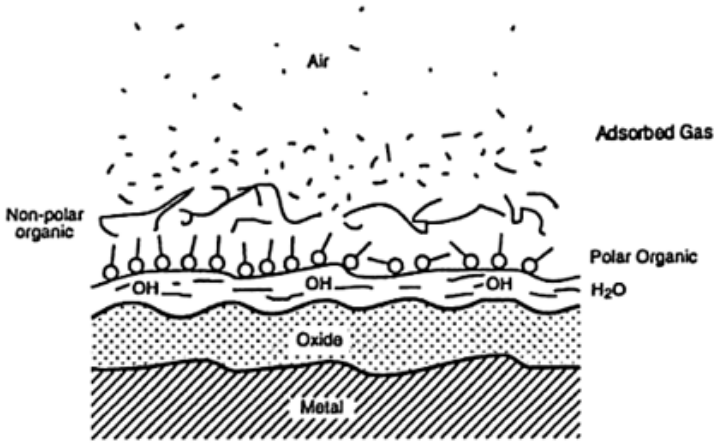

Figure 1.1 Schematic of a sample surface having been exposed to air. Illustration from [6].

A significant improvement would be the ability to perform common surface processes, such as exposure to activated gasses, annealing and thin-film deposition, in-situ, without exposure to the ambient, and to couple this with a measurement system that can measure the surface in real-time during the surface processing.

X-ray photoelectron spectroscopy (XPS) is a technique that is highly suited for measuring chemical state, energetics and surface morphology of solid surface. Like the majority of surface science techniques it has been limited in the past to static surfaces, those surfaces which are unchanging during the measurement, due to the long measurement time. The recent development of position sensitive electron detectors has brought the measuring times of the technique into the sub-second regime, and by performing XPS during allowing surface processing to be monitored in real-time.

Examples of the use of real-time photoelectron spectroscopy may be found in the literature, mainly by research groups developing position sensitive electron detectors. At Aberystwyth the technique has been used to investigate the diamond surface by Bushell [7], Roberts [8] and Evans et al [9, 10]. All have made use of a custom built discrete channel detector,

publications on which may be found by Langstaff and Evans [11-13]. A major contributor to the real-time photoelectron spectroscopy field has been the group of Paolucci at the ELETTRA synchrotron radiation source, Trieste, Italy [14], who published one of the first reports of a real-time measurement on the adsorption of CO onto Pt (111) [15]. The Fadley group at the Lawrence Berkeley National Laboratory have also published real-time photoelectron spectroscopy results [16].

This thesis the use of real-time XPS to monitor the surface processing of three solid surfaces; metals, boron doped diamond and zinc oxide. Metals are the foundation of the materials industry being used from catalysis to electrical contacts. The measurement of metals at high temperature and during thin-film deposition is therefore of importance to the materials engineer. Boron doped diamond has extreme electrical, thermal, mechanical and chemical properties and has the potential to supersede silicon as the material of choice for electronic applications [17]. Zinc oxide has been known for decades as a remarkable material for which new applications are consistently being found [18, 19]. The physics of the polar surfaces of zinc oxide are yet to be fully understood and measuring the processing of those surfaces during high temperature annealing and thin-film deposition is attractive to a wide array of scientists and engineers.

The thesis has been arranged with a section on essential theory underpinning the work, a description and characterisation of the equipment, three sections for the three materials under investigation, followed by an overall summary.

References

1. Lovelock, K.R.J., et al., *Photoelectron Spectroscopy of Ionic Liquid-Based Interfaces.* Chemical Reviews, 2010. **110**(9): p. 5158-5190.
2. Krepelova, A., et al., *The nature of nitrate at the ice surface studied by XPS and NEXAFS.* Physical Chemistry Chemical Physics, 2010. **12**(31): p. 8870-8880.
3. Ghosal, S., et al., *Electron spectroscopy of aqueous solution interfaces reveals surface enhancement of halides.* Science, 2005. **307**(5709): p. 563-566.
4. Verdaguer, A., et al., *Molecular structure of water at interfaces: Wetting at the nanometer scale.* Chemical Reviews, 2006. **106**(4): p. 1478-1510.
5. Woodruff, D.P. and T.A. Delchar, *Modern techniques of surface science*. 2 ed. 1999, Cambridge, UK: Cambridge University Press.
6. Kern, W., ed. *Handbook of semiconductor wafer processing*. Materials science and process technology series, ed. R.F. Bunshah and G.E. McGuire. 1993, Noyes Publications: Park Ridge, NJ, USA.
7. Bushell, A., *A new multi-channel detector for electron spectroscopy and its application to single crystal diamond*. 2005, Univeristy of Wales, Aberystwyth: Aberystwyth.
8. Roberts, O.R., *The Application of Real-Time Photoelectron Spectroscopy to Carbon-Based Semiconductors*. 2009, Aberystwyth University: Aberystwyth.
9. Evans, D.A., et al., *Diamond-metal contacts: interface barriers and real-time characterization.* Journal of Physics-Condensed Matter, 2009. **21**(36).
10. Evans, D.A., et al., *Direct observation of Schottky to Ohmic transition in Al-diamond contacts using real-time photoelectron spectroscopy.* Applied Physics Letters, 2007. **91**(13): p. 132114-3.
11. Langstaff, D.P., et al., *A fully integrated multi-channel detector for electron spectroscopy.* Nuclear Instruments and Methods in Physics Research Section B: Beam Interactions with Materials and Atoms, 2005. **238**(1-4): p. 219-223.
12. Langstaff, D.P. and T. Chase, *A multichannel detector array with 768 pixels developed for electron spectroscopy.* Nuclear Instruments and Methods in Physics Research Section A: Accelerators, Spectrometers, Detectors and Associated Equipment, 2007. **573**(1-2): p. 169-171.
13. Langstaff, D.P., et al., *Progress on the Aberystwyth electron counting array.* Nuclear Instruments and Methods in Physics Research Section A: Accelerators, Spectrometers, Detectors and Associated Equipment, 2009. **604**(1-2): p. 133-135.
14. Baraldi, A., et al., *Real-time X-ray photoelectron spectroscopy of surface reactions.* Surface Science Reports, 2003. **49**(6-8): p. 169-224.
15. Baraldi, A., et al., *Time resolved core level photoemission experiments with synchrotron radiation.* Journal of Electron Spectroscopy and Related Phenomena, 1995. **76**: p. 145-149.
16. Nambu, A., et al., *An ultrahigh-speed one-dimensional detector for use in synchrotron radiation spectroscopy: first photoemission results.* Journal of Electron Spectroscopy and Related Phenomena, 2004. **137-140**: p. 691-697.
17. Wort, C.J.H. and R.S. Balmer, *Diamond as an electronic material.* Materials Today, 2008. **11**(1-2): p. 22-28.
18. Ozgur, U., et al., *A comprehensive review of ZnO materials and devices.* Journal of Applied Physics, 2005. **98**(4): p. 041301-103.
19. Look, D.C., *Recent advances in ZnO materials and devices.* Materials Science and Engineering: B, 2001. **80**(1-3): p. 383-387.

2. Theory

In this section essential theory underpinning the work is presented.

2.1. Ultra High Vacuum

For the study of surfaces a basic requisite is a vacuum environment for two primary reasons; to prepare and maintain clean surfaces, and to measure electron emission and scattering from surfaces. Vacuum is measured in terms of the amount of material present in the form of residual gas molecules. The ideal gas law can be used to relate the amount of material in a given volume to the pressure with (2.1), where n is the gas density, N the number of gas molecules, V the volume, P the pressure, k the Boltzmann constant, and T the temperature.

$$n = \frac{N}{V} = \frac{P}{kT} \tag{2.1}$$

Pressure is measured in Pascal however the non-SI unit mbar is often used where 100 Pa = 1 mbar. By applying kinetic gas theory, where gas molecules are modelled as spheres of finite diameter within a finite volume, the necessity for vacuum can be demonstrated by considering the distances molecules can travel without colliding with each other and the number of molecules colliding with a surface per unit time. The average distance between gas molecule collisions, or the mean free path is given in (2.2) and the flux of molecules colliding with a surface, known as the Hertz-Knudsen equation, is given in (2.3), where λ is the mean free path, k the Boltzmann constant, m the molecular mass, T the temperature, σ the collision cross-section, F the molecular flux, and P the pressure.

$$\lambda = \frac{1}{\sqrt{2}\sigma}\frac{kT}{P} \tag{2.2}$$

$$F = \frac{P}{\sqrt{2\pi mkT}} \tag{2.3}$$

The mean free path provides an absolute minimum value for the gas pressure for particles to travel from a sample to a measuring device without being scattered by the residual gas molecules. For typical distances of 1 m the required pressure would be less than 10^{-4} mbar. The molecular flux on a surface can be used to estimate the time taken for a monolayer of residual gas to form on a surface (2.4), where t_{ML} is the monolayer formation time.

$$t_{ML} = \frac{10^{19}}{F} \tag{2.4}$$

It can be shown with (2.3) and (2.4) that at a pressure of 10^{-6} mbar a monolayer of contamination would form in 1 s provided that all incident molecules stick to the surface (sticking coefficient of 1). Table 2.1 lists the properties of four vacuum regimes commonly encountered. For performing surface science experiments the ultra high vacuum regime is considered a minimum. At base pressure of 10^{-10} mbar a sample can expect to be free from residual contamination for 10^4 s, or 3 hours, allowing ample time for measuring clean surfaces after preparation.

Vacuum Regime	Pressure 10^x (mbar)	Particle density 10^x (cm^{-3})	Mean free path 10^x (m)	ML time 10^x (s)
Atmospheric	3	25	-8	-9
Low	1	22	-5	-6
Medium	-3	19	-2	-3
High	-6	16	2	1
Ultra high	-10	12	5	4

Table 2.1 Pressure regimes with typical values for the particle density, mean free path and monolayer formation time.

2.2. In-situ processing

In this work three methods of in-situ processing were used; activated gases, thin film deposition and annealing.

2.2.1. Activated gases

Processing a surface through exposure to a low-pressure gas in-situ will not produce the desired result in a satisfactory time-frame as ground-state gases are too un-reactive. An activated gas is much more reactive due to the presence of atomic and excited species. The production of activated species is therefore required for in-situ gas processing. Processing with activated gases is extremely varied and examples in the literature include hydrogen [1, 2], oxygen [3, 4] and fluorine [5, 6]. There is also the entire field of Chemical Vapour Deposition (CVD) of materials [7, 8]. The ability to perform gaseous processing in-situ is highly advantageous as it allows ultra-clean surfaces to be produced. A method of promoting molecules into their excited states and forming activated species is therefore required, and a method of achieving this is with a low-pressure, non-thermal plasma.

A plasma is a state of matter composed of ions and free electrons. Plasmas may broadly categorised as being thermal or non-thermal depending on the energies (temperature) of the ions. In a thermal plasma the ions have energies equivalent to several thousand degrees Kelvin while in non-thermal plasmas the ions have negligible energies. For both cases the free electrons have high energies.

Two types of electron recombination are of prevalent in non-thermal plasma: radiative and dissociative recombination [9]. In radiative recombination (2.5) an energetic electron (e^-) is captured by an ion (X^+) producing a neutral excited species (X^*). In dissociative

recombination (2.6) a diatomic ion is dissociated into its two constituent atoms by the capture of an energetic electron. Plasmas therefore contain excited and dissociated species and therefore may be used to activate gas molecules.

$$X^+ + e^- \longrightarrow X^* \quad (2.5)$$

$$XY^+ + e^- \longrightarrow X + Y \quad (2.6)$$

To create and sustain a plasma ions and free electrons have to be continually produced otherwise all species would eventually become neutral through electron recombination. In the laboratory the most common method of generating a non-thermal plasma is the hot filament method where a filament is heated until thermionic electrons are generated, a proportion of which will have enough energy to dissociate gas molecules and to ionize molecules and atoms through collisions. The use of this technique requires the filament to be very close to the sample surface and the entire chamber at an elevated partial pressure of the desired gas species. The main drawbacks of this method is the low yield of activated species and deposition of the filament material on the sample surface. A more suitable method is to use microwave energy to sustain the plasma, provided there is an initial source of ions and free electrons. The plasma state is sustained by energising free electrons with microwaves which then collide with neutral molecules producing excited ions. This method is more suitable since the plasma may be generated remotely from the sample surface allowing for a cleaner environment with minimal surface damage.

Activated oxygen

Three methods of producing activated oxygen with microwave plasma have been identified in the literature – the dissociation of molecular oxygen [10], the dissociation of nitrogen and reacting with nitric oxide [11], and the dissociation of nitric oxide [12]. Using nitric oxide as the source gas was reported to achieve a more stable flux of active oxygen than oxygen gas [12] therefore this method was chosen.

Excited nitric oxide systems are very reactive and several complex reactions are possible [13]. The principal reactions are the dissociation of nitric oxide into atomic oxygen and atomic nitrogen (2.7), the recombination of atomic nitrogen and oxygen to form diatomic nitrogen (N_2) and oxygen (O_2) (2.8 and 2.9), and the recombination of nitric oxide with atomic nitrogen to form diatomic nitrogen and atomic oxygen (2.10).

$$NO \longrightarrow N^* + O^* \tag{2.7}$$

$$N + N \longrightarrow {N_2}^* \tag{2.8}$$

$$O + O \longrightarrow {O_2}^* \tag{2.9}$$

$$NO + N \longrightarrow {N_2}^* + O^* \tag{2.10}$$

The radiative recombination of nitrogen and oxygen produce photons in the VUV, optical and infra-red. The VUV emission is of great benefit to the production of active oxygen as diatomic oxygen absorbs VUV radiation and dissociates into active oxygen [14].

2.2.2. Thin films

Depositing one material onto another is a common surface processing method. Usually one material is a substrate (B) and the other evaporated from a molecular beam source. The flux from such a source, as given in (2.3), provides a number of molecules per unit time which may adsorb onto the substrate surface. The single molecules may remain at their adsorption site or diffuse along the surface, depending on the bonding strength with the substrate, but may also be lost from the surface through several mechanisms including re-evaporation, diffusion into the substrate and capture by other single molecules or by traps [15]. The kinetics of the single molecules determines the nature of the thin film, in particular the growth mode of the film on the substrate.

In a review in 1958 Ernst Bauer [16] identified three primary thin film growth modes reported in the literature as illustrated in Figure 2.1. The first is Volmer-Weber (clustered) growth where no complete layers are formed and the material clusters on the substrate due to weak bonding between the molecules and the substrate. The second is Frank-van der Merwe (layer-by-layer) where the material forms complete layers due to strong bonding between the molecules and the substrate. Thirdly is Stranski-Krastanov growth where layer-by-layer growth proceeds for a few monolayers followed by cluster growth.

The growth mode is influenced predominately by the surface energy of the substrate (γ_B), overlayer (γ_A) and the interface energy (γ^*) [15]. Clustered growth of material B on A will occur if inequality (2.11) is satisfied while layer-by-layer growth of material B on A will occur if inequality (2.12) is satisfied. Stranski-Krastanov growth represents the transition from layered growth to clustered growth, therefore (2.11) is satisfied only for the first few layers.

The transition is due to an increase in the interface energy as the number of layers increases due to factors such as the strain and molecular orientation of the growing film.

$$\gamma_B > \gamma_A + \gamma^* \quad (2.11)$$

$$\gamma_B < \gamma_A + \gamma^* \quad (2.12)$$

For inorganic materials there is a major importance on lattice matching, that is matching the substrate and overlayer crystalline spacing and orientation, to prevent the formation of lattice defects. Lattice defects introduce non-characteristic energy levels and have inferior electrical, thermal and mechanical properties. Organic materials, having relatively weak van der Waals bonding, are less cohesively bonded to the substrate and are able to form crystalline structure on mismatched lattices without compromising the crystallinity [17].

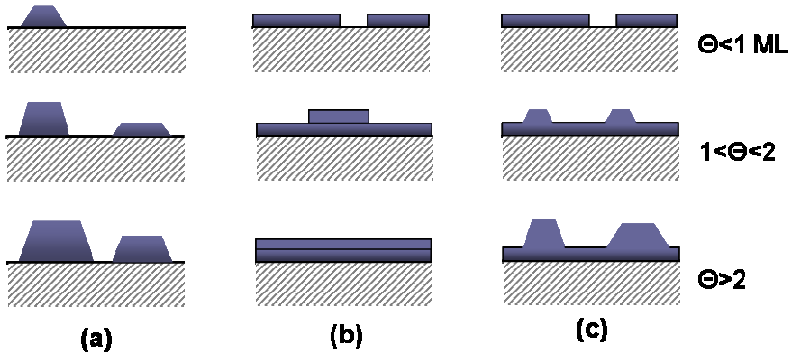

Figure 2.1 Three growth modes encountered, with film thicknesses progression from top to bottom, overlayer dark shaded and sample light shaded. Image a) shows Volmer-Weber (cluster) growth, b) layer-by-layer growth, and c) Stranski-Krastanov growth. Illustration from [18].

Metal phthalocyanines

Metal Phthalocyanine (MPc) have the chemical formula $C_{32}H_{16}N_8M$, where M is a metal atom. Traditionally they have been used in the textile industries however their semiconducting properties have brought these molecules into the forefront of materials research. The structure, shown in Figure 2.2 (with copper as the metal atom), has four benzene rings and four pyrrole rings, the pyrrole sharing two carbon atoms with the benzene. The thirty-two carbon atoms are in two chemical environments; twenty-four in the benzene configuration and eight in the pyrrole configuration. The eight nitrogen atoms are in two chemical environments; four in a C-N-C configuration and four in a Metal-N configuration. The total molar ratios expected in XPS are therefore C / Metal = 32, N / Metal = 8 and C / N = 4, while the C 1s core-level should contain two chemical components in a 3 : 1 ratio, and the N 1s core-level two components in a 1 : 1 ratio. Copper Phthalocyanine, used in this work, has the copper atom in the second oxidative state, bandgap of 2.3 eV [19], work function of 4.2 eV [20] and p-type characteristic [21].

Buckminsterfullerene

Buckminsterfullerene, also known as C60, is a spherical structure composed of 60 carbon atoms, illustrated in Figure 2.3, discovered in 1985 by Kroto et al [22]. It was the first of the family of the fullerenes to be discovered, fullerenes being the fourth carbon allotrope known (amorphous, graphite, diamond, fullerene). The structure is mathematically known as a truncated icosahedron and is a collection of 20 carbon hexagons and 12 carbon pentagons, the carbon being covalently bonded. Having sp^2 carbon-carbon bonds C60 is highly conductive, has a bandgap of 2.1 eV [23], work function of 4.7 eV [20] and has n-type character [24].

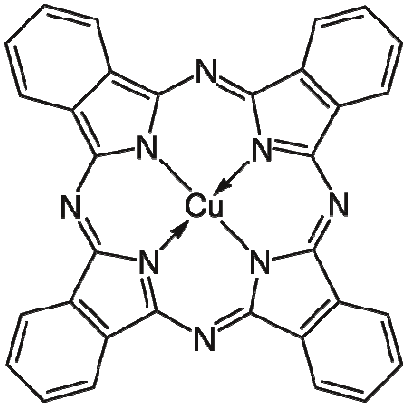

Figure 2.2 Copper Phthalocyanine molecular structure. The central copper atom is bonded to four nitrogen atoms. Image from [25].

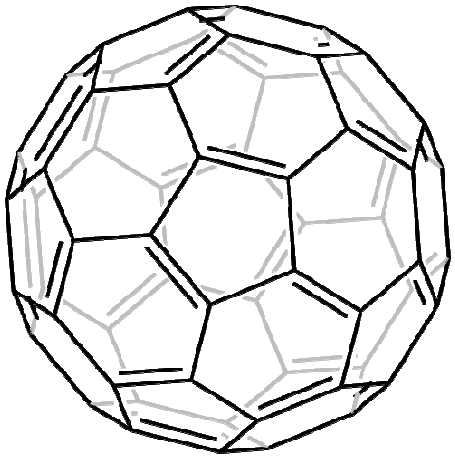

Figure 2.3 Buckminsterfullerene molecule, also known as C60. Illustration from [26].

2.3. Photoelectron Spectroscopy

Photoelectron spectroscopy is a technique that may be used to determine orbital ionization energies, chemical composition, compound stoichiometry, work function and overlayer thickness and morphology. The principle of the technique is that by measuring the spectrum of photoelectrons emitted from a material due to the photoelectric effect the electronic energy levels may be directly determined. Photoelectrons may be emitted from open electron shells (valence electrons) or from closed electron shells (core-level electrons), and in this work focus is given to the core-level electrons only. Core-levels appear in a photoelectron spectrum as discrete lines the position and intensity of which are of interest. The lines exhibit an energy shift, known as a chemical shift, that is related to the chemical environment of the atom, giving additional lines at higher and lower energy to the main line, which may be used to determine the chemical environment of the atom.

Two basic components are required for photoelectron spectroscopy; a high energy (>1 keV) photon source to irradiate a sample and produce photoelectrons (photoelectric effect) and an electron analyser to measure the spectrum of the emitted photoelectrons. The sample and electron analyser must be in vacuum to avoid scattering of the photoelectrons by residual gas molecules and for maintaining a clean sample surface.

Figure 2.4 shows a material with a core-level, Fermi level and vacuum level and a spectrometer with a Fermi level and vacuum level in electrical contact with the material. The core-level has an ionization energy defined as the energy required to remove an electron from that level into the vacuum. By considering conservation of energy any electron removed from the core-level will have a kinetic energy equal to the difference between the photon energy and the ionization energy. This is given in (2.13) where hv is the photon

energy, E_K the electron kinetic energy, E_B^{EF} the core-level binding energy and ϕ_M the work function of the material. Because the Fermi level is aligned between the material and spectrometer (2.14) may be written. By combining (2.13) with (2.14) an expression for the binding energy of the core-level may be written that is independent of the material work function, and this is given in (2.15). By measuring the kinetic energy of the photoelectrons reaching the spectrometer (E_K') the core-level binding energies may be directly measured.

$$h\nu - E_K = E_B^{EF} + \Phi_M \tag{2.13}$$

$$E_K + \Phi_M = E_K' + \phi_S \tag{2.14}$$

$$E_B^{EF} = h\nu - E_K' - \phi_S \tag{2.15}$$

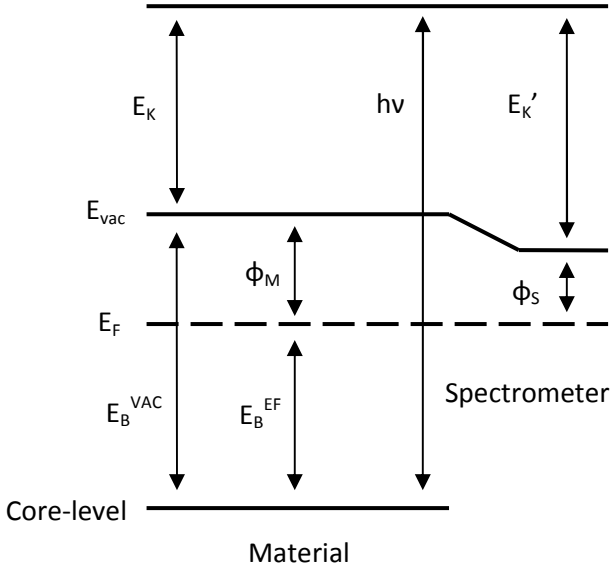

Figure 2.4 Energy level alignment between a material and spectrometer. The material has a work function of ϕ_M and a core-level in a sample has a binding energy of E_B' relative to the vacuum level and E_B^{EF} relative to the Fermi level. The spectrometer has a work function of ϕ_S. A photon of energy hν has removed an electron from the core-level into the vacuum where is has a kinetic energy E_K in the sample and E_K' in the spectrometer.

2.3.1. Binding energy

The binding energy of a core-level may be understood when the total energy of the atom before and after absorption are considered, as illustrated in Figure 2.5. A ground state neutral atom is said to be in an initial state and has a total energy equal to the initial state energy, $E_{initial}$. After absorption of a photon the atom has a total energy equal to the initial state energy plus the photon energy, hν, as given in (2.16). Following the emission of a photoelectron (which carries away energy as kinetic energy, E_K) the atom, now an ion, is said to be in a final state and has a total energy known as the final state energy, E_{final}. The total energy of the ion and the photoelectron may be written as (2.17), and through conservation of energy (2.16) must be equal to (2.17). The binding energy of the core-level is then understood as being the difference between the initial and final state energies, as given in (2.18). When considering a solid rather than an atom (2.18) must be modified by subtracting the work function from the RHS, giving the same expression as (2.15).

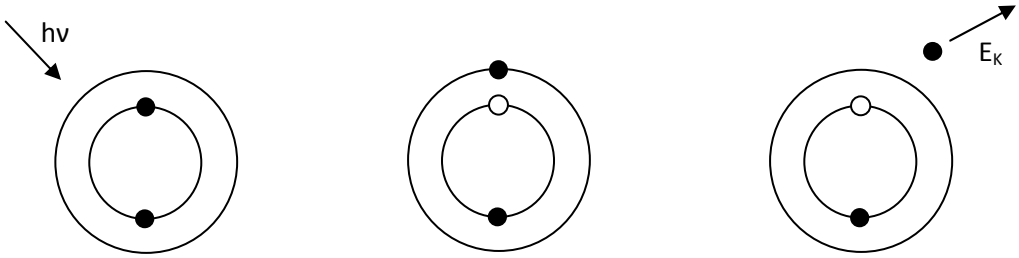

Figure 2.5 Photoemission process with total energies given; a) neutral atom before photon absorption; b) excited neutral atom after photon absorption, c) ion and a photoelectron.

$$E_{initial} + h\nu \tag{2.16}$$

$$E_{final} + E_K \tag{2.17}$$

$$E_B = E_{final} - E_{initial} = h\nu - E_K \tag{2.18}$$

The initial and final state energies therefore influence the binding energies of core-levels, and perturbations to those energies result in the chemical shift. Models of binding energies have been developed and a discussion may be found by Hüfner [27] and by Mårtensson and Nilsson [28]. The current understanding is that the binding energy has two main contributors; the orbital energy (ε) and the relaxation energy (E_{Relax}), as given in (2.19).

$$E_B = -\varepsilon + E_{Relax} \tag{2.19}$$

The orbital energy is the energy associated with the core-level orbital, which may be calculated from quantum mechanics, and is the same for the neutral atom and the ion. The equivalence of the neutral atom and ion orbitals is an approximation often referred as the frozen orbital theory. The relaxation energy is the energy associated with the ion re-distributing charge due to the presence of the core-hole. If the relaxation energy were zero then the binding energy would simply be equal to the negative of the orbital energy, and this result is known as Koopmans' theorem, i.e that the binding energy may be directly calculated.

Variations to the initial state energy are generally changes to the chemical environment of the atom such as chemical bonding and stoichiometry. Other examples include whether the atoms being measured are in the bulk or at the surface of the material and if the material is alloyed. An additional initial state effect is that of thermal expansion. A material measured at two different temperatures would have a different inter atomic spacing and thus the orbital energy would be different resulting in a different binding energy. A chemical shift in proportion to the fractional change in distance is therefore expected, as given in (2.20), where δx/x represents the fractional length change, α the linear thermal expansion coefficient and Δθ the temperature change. The effect is discussed by Hüfner [27] who

noted that a shift to lower binding energy is expected. Such a shift has been observed for aluminium [29] and copper [30], however a shift to higher binding energy has been reported for the group I and II metals [31]. A general model of the effect has been presented by Riffe et al [31] and agreement was found for most of the group I and II elements (with the exception of lithium), however the predicted values for aluminium were inaccurate leading to the conclusion that the model required refining.

$$\frac{\delta x}{x} = \alpha(\Delta\theta) \tag{2.20}$$

It is also necessary to consider how the deposition of a material on a surface may cause a chemical shift in the substrate and the overlayer due to charge transfer between the overlayer and substrate. For the overlayer a shift is expected due to charge transfer to occur during the first monolayer of overlayer material, and such a shift is known as band-bending. For a metallic substrate no shift is expected to substrate core-levels however for a semiconductor substrate the presence of adsorbate energy levels at the interface may result in significant charge transfer resulting in a shift.

A change in the secondary electron cut-off may occur, usually due to a change to the surface work function or due to band-bending change in the overlayer. A change to the work function represents a change to the vacuum level of the surface, and to correctly determine this the changes to the band-bending in the overlayer must be considered.

2.3.2. Auger effect

Following the photoemission process the ion (with a core-hole) is energetically unstable and may become more stable through either x-ray fluorescence or through the Auger process. Fluorescence is simply the filling of a core-hole with an electron from a higher energy shell with the emission of a photon. In the Auger process the core-hole is filled by an electron from a higher shell, however energy is released by the emission of an electron from another shell. The atom therefore self-ionizes (becoming doubly ionized in the process). The ejected electron is known as an Auger electron and its kinetic energy is given by (2.20) where E_K is the kinetic energy, E_C the binding energy of the core-hole level, E_B the binding energy of transiting electron level, and $E_{C'}$ the binding energy of the Auger electron level.

$$E_K = E_C - E_B - E_{C'} \tag{2.21}$$

When labelling Auger electrons the convention is to use x-ray notation; first noting the core-hole level, second noting the transiting electron level, and third noting the Auger level. For example $KL_1L_{2,3}$ refers to a transition where a core-hole was created in the K shell, an electron from the L_1 shell filled the core-hole, and an Auger electron was emitted from the $L_{2,3}$ shell. Transitions where the core-hole is filled by an electron from the same shell are known as Coster-Kronig transitions (such as $L_1L_{2,3}M_1$ transitions) [32]. The photon emission and Auger processes are competitive and the Auger yield is dependent on the atomic number; lighter atoms favour Auger emission while heavier elements favour photon emission.

2.3.3. Inelastic scattering

Photoelectron spectrum of core-levels have additional intensity to lower kinetic energy and this is due to photoelectrons scattered during travel through the solid. A characteristic length, known as the electron attenuation length (EAL), may be defined where the probability of scattering drops by e^{-1} [27]. The EAL is dependent on the photoelectron energy and on the properties of the solid and is of the order of nanometres. Workers have collected values for EALs across a range of kinetic energy values for a variety of materials and collated tables are available [33].

The photoelectron intensity is therefore a function of depth from the surface and for emission normal to the surface may be written as (2.22), where I is the measured intensity, I_0 the intensity for an infinitely thick sample, d the depth and λ the EAL. From (2.22) the analysis depth of XPS may be evaluated; 65% of the photoelectron intensity will originate within λ of the surface, 85% from < 2λ, and 95% from < 3λ [34]. 3λ is therefore considered the standard analysis depth for photoelectron spectroscopy and is also of the order of nanometres, resulting in the high surface sensitivity.

$$I = I_0 e^{(-d/\lambda)} \tag{2.22}$$

The EAL may be determined by the overlayer method where the photoelectron intensity is measured for a clean surface and with an overlayer of known thickness. The rate of material deposition may be included into (2.22) giving (2.23), where r is the rate in nm/s and t the time in seconds, giving a relationship between photoelectron intensity and coverage.

$$\ln\left(\frac{I}{I_0}\right) = \left(-\frac{r}{\lambda}\right) t \tag{2.23}$$

2.3.4. Photon source

For a photoelectron spectrum to correctly represent energy levels the photon source must consist of a single narrow energy (monochromatic). If a broad or continuous distribution were used then photoelectrons with a range of energies would be produced from each energy level and severely impair interpretation of the spectrum.

It should also be evident that the deepest energy level accessible is determined by the photon energy, with higher photon energies permitting the excitation of deeper levels. The shallowest electrons are the valence electrons and have binding energies in the range of zero to 25 eV. The remaining electrons, those in closed electron shells, are collectively termed core-electrons, and may have binding energies up to several keV.

It is therefore desirable to have a photon source with an energy of at least 1 keV that is intense and has a narrow linewidth. Such a photon source may be obtained by passing a continuous spectrum of light through a monochromator. At present the only continuous light source with sufficient emission in the x-ray region is synchrotron radiation [35], however synchrotron radiation is generally provided at a central facility and is not suitable for laboratory use.

For a laboratory based photon source characteristic x-ray radiation emitted by atoms may be used since this is both intense and has a narrow linewidth. Table 2.2 gives the x-ray emission lines of suitable materials. Characteristic x-ray emission may be obtained through the creation of core-holes in a material and this may be done by irradiating a material with high energy electrons. Such a source is known as an x-ray tube and is a regularly used for laboratory based photoelectron spectroscopy. In addition to characteristic radiation an x-ray

tube will also produce a continuous background due to the rapid deceleration of the electrons. The background is characterised by a sharp cut-off at high energy determined by the maximum kinetic energy of the incident electrons, as in (2.24), where E_{max} is the high energy cut-off, e the electronic charge and V_0 the accelerating voltage. For electrons with energies greater than a few keV the background tends to be in the x-ray region of the spectrum.

$$E_{max} = eV_0 \tag{2.24}$$

The background may be removed by passing the light through a monochromator. This also narrows the linewidth, for example the linewidth of aluminium Kα x-rays may be reduced from 0.9 eV to 0.4 eV with a monochromator. A consequence of using a monochromator is a large loss in intensity therefore this is not suitable for real-time XPS.

Element	Energy (eV)	FWHM (eV)
Mg	1253.6	0.7
Al	1486.6	0.9
Si	1739.6	1.0
Cr	5417.0	2.1

Table 2.2 Selected characteristic x-ray emission lines. Data taken from [34].

2.3.5. Electron analyser

Over the years different techniques have been used to measure electron spectrum including time of flight, deceleration in an electric field, or orbit change in a magnetic field [27]. The use of electric fields was first described by Purcell [36], and several analyser designs have been manufactured including Cylindrical Mirror (CMA), Cylindrical Deflection (CDA) and Hemispherical Sector (HSA). Today the HSA is the most widely used analyser design.

Hemispherical Sector Analyser

The HSA is based on two hemispheres, separated by a distance of the order of 1 cm, that are electrically isolated. At one end of the hemispheres is an entrance plane containing an entrance slit, while on the opposite side is an exit plane. The 180° geometry of the HSA provides perfect focus of electrons from the entrance slit to the exit plane without distortion, making it superior to other analyser designs [37].

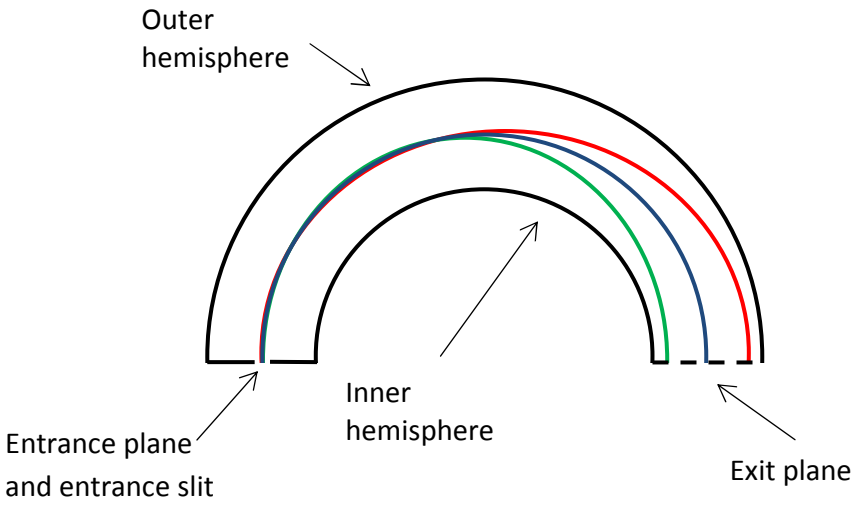

Figure 2.6 Schematic of an analyser. The main body of the analyser is composed of two hemispheres, inner and outer. Three electron paths are shown successfully traversing the hemispheres from the entrance slit to the exit plane.

Photoelectrons are collected and retarded by a lens and are focused onto the entrance slit. The voltages applied to the two hemispheres result in electrostatic dispersion of the electrons and only those having the correct trajectory will traverse to the exit plane. The energy of those electrons following a perfect trajectory through the analyser is known as the pass energy, and this is given by (2.25) where ΔE_{pass} is the electron pass energy, q the electron charge, ΔV the voltage difference between the hemispheres, R_2 and R_1 the outer and inner hemisphere radii and k the analyser constant [34]. This is shown schematically in Figure 2.6 where a beam of electrons incident on the entrance slit is dispersed by the potential applied to the hemispheres. Three trajectories are shown representing perfect trajectory and those offset in energy by an amount determined by (2.25).

$$\Delta E_{pass} = (-q)\Delta V\left(\frac{R_1 R_2}{R_2^2 - R_1^2}\right) = (-q)k\Delta V \tag{2.25}$$

Along the exit plane the electron energy window is dispersed in energy along one axis and angularly dispersed along the orthogonal axis [37], the energetic dispersion being determined by the electron pass energy. A relationship between electron energy and position along the exit plane is given by (2.26), where ΔE_K represents kinetic energy, D the dispersion in eV/mm, and Δx distance along the plane.

$$\Delta E_K = D(\Delta x) \tag{2.26}$$

For determining the electron energy spectrum it is necessary to count the number of electrons as a function of energy. Originally this was done by having an exit slit mounted in the centre of the exit plane, in line with the entrance slit, and to have an electron counter mounted behind the exit slit. For a given set of analyser voltages only electrons of a known energy could traverse to the electron counter. Thus by varying the analyser voltages the

electron energy distribution could be measured. However such an approach is inefficient since all electrons with trajectories outside the exit slit are lost. Since the actual energy of those electrons is known through (2.32), workers realised that is would be possible to place additional exit slits and detectors either side of the central exit slit. Some analysers are available in this configuration, for example the VG ESCALAB Mk3 has three exit slits/detectors, while the SPECS Phoibos MCD-9 detector has nine [38]. However this is still not very efficient, and a new approach, that of measuring spectrum across the entire exit plane using position sensitive detectors, is now used.

Position sensitive detectors

Position sensitive detectors (PSD's) allow for spatially resolved electron counting at the analyser exit plane [39]. Four classes of PSD are noted in the literature; discrete channel, coincidence array, charge division and optical image detectors, the first and last of which will be discussed.

Discrete channels are a series of collecting channels positioned along the exit plane, each channel being connected to discriminator and pulse counting hardware, that directly count the number of incident electrons. Such a detector was demonstrated by Manning et al [40] that had 40 channels and was followed by Gori et al [41] who produced a detector with 96 channels. Further increases in the channel density becomes difficult due to the associated hardware and cross-talk between the channels. By incorporating the channels and pulse counting hardware as part of a single assembly much of the noise and geometric difficulties is addressed. Nambu et al [42] and Langstaff et al [43] reported on 768 channel detectors.

The optical image method is an indirect method relying on the conversion of electrons to photons using a phosphorescent screen and imaging the screen with a Charge Coupled Device (CCD). The phosphor screen/CCD configuration has an advantage over the discrete channel method in that it may measure the exit plane in two dimensions allowing the energy and angular distribution of the electrons to be determined, and was used in this work.

The CCD, invented by Boyle and Smith [44], is a two dimensional array of metal-oxide-semiconductor (MOS) capacitors that accumulate charge in proportion to the intensity of incident light. Photons with energies greater than the band-gap of silicon (1.1 eV) produce an electron-hole pair which dissociates with the electron being accumulated. At the end of each row of is a measurement capacitor, amplifier circuit and an analogue to digital converter. Following exposure to light each row of capacitors transfers the charge to the next capacitor resulting in the measurement capacitor being filled. The charge is then converted into a voltage, amplified and converted into a digital signal. By repeating this transfer of charge each capacitor in the array can be read and converted into a digital signal. The photons generated by the phosphorescent screen are thus digitally encoded by the CCD, allowing the electron distribution across the exit plane of the analyser to be determined. Each capacitor represents a pixel and thus CCDs are specified by the number of pixels.

Amplification

Due to the low number of electrons produced by the photoemission process some form of amplification is required prior to the phosphor screen that is capable of preserving the spatial distribution of the electrons. This is provided by a Micro Channel Plate (MCP), a high-density collection of Channel Electron Multipliers (CEMs) [39].

CEMs are thin glass tubes lined with electron emissive material that have a potential difference of several kV applied between the two ends. A single electron entering the tube will collide with the side and cause the emission of several additional electrons, each of which will then collide with the sides and produce more electrons, resulting in a gain. By housing CEMs with a typical spacing of 12.5 μm [45] in an assembly electron amplification is achieved in which the spatial distribution is preserved. A typical MCP may have a gain of 10^4, however further gain may be achieved by combining MCPs in stages, with two stages producing a overall gain of 10^6 and three stages for an overall gain of near 10^8 [45].

Operating mode

An electron analyser with a CCD may be used in two modes for measuring photoelectron spectrum; scanning and snapshot modes.

Scanning mode is recording the electron intensity at each pixel of the CCD while changing the analyser voltages from a start to an end point, the start and end voltages corresponding to the energy range of interest. Each pixel will record a photoelectron spectrum having an energy offset to each other that is determined by the spatial position of the pixel, as given in (2.32) for the exit plane of the analyser. By using matrix algebra methods all the individual pixel spectrum may be combined to produce and overall spectrum by correct consideration of the energy offset between the pixels, and this is typically automatically done by the CCD hardware/software.

Snapshot mode is where the analyser voltages remain fixed giving an electron energy window of several electron volts wide on the CCD and the spectrum is given by the intensity recorded by each pixel of the CCD. This mode of operation was first suggested by Manning et

al [40] and allows spectrum with a comparable resolution to scanning mode to be measured in an instant (the time limited by the integration time of the CCD).

$$\Delta E_B = -C(\Delta d) \tag{2.27}$$

For a snapshot spectrum a relative binding energy scale may be written with (2.27) where ΔE_B represents binding energy, C the dispersion and Δd the pixel number. This equation has been introduced in (2.26) in a slightly different form where the dispersion at the exit plane was given in terms of eV/mm rather than eV/pixel and the energy scale was in kinetic energy rather than binding energy.

Resolution

A perfect electron analyser would measure a delta distribution when mono-energetic electrons are incident, however as with all measuring apparatus there is a measuring resolution. For the HSA the resolution is given by (2.28) where ΔE is the resolution, E_P the pass energy, w the entrance slit width and R_0 the mean hemisphere radius.

$$\Delta E = E_P \frac{w}{2R_0} \tag{2.28}$$

The MCP/CCD will also have a measuring resolution corresponding to the minimum number of pixels/channels recording a signal when a narrow beam of electrons is incident. The Point Spread Function (PSF) of the MCP/CCD is due to the amplification process, conversion of electrons to photons and to adjacent pixels incorrectly registering a charge.

The linewidth of the photon source also limits the measuring resolution. By adding the analyser resolution to the photon linewidth in quadrature an expression for the overall

resolution is given (2.29), where ΔE_{an} is the analyser resolution and ΔE_{photo} is the light source linewidth.

$$\Delta_{\mathrm{total}} = \left(\Delta \mathrm{E}_{\mathrm{an}}^2 + \Delta \mathrm{E}_{\mathrm{photo}}^2\right)^{1/2} \tag{2.29}$$

It can be shown that in addition to the resolution the individual contributions affect the line-shape. The analyser has a Gaussian line-shape, the energy level a Lorentzian, and the photon source is either Gaussian for a monochromator, Lorentzian for x-ray gun. As a result the core-level spectrum measured are a convolution of Gaussian and Lorentzian line-shapes, known a Voight line-shape [27, 46].

2.3.6. Quantification

Photoelectron spectroscopy allows the concentration of different atomic species present in a sample to be determined due to the unique photoionization cross-section of energy levels.

It should be obvious that the number of photoelectrons excited from a particular energy level in a single atom is dependent on the number of photons incident onto the atom and the photoionization cross-section of the energy level. For a homogeneous sample the number of photoelectrons excited is a product of the number of atoms with an identical energy level. There is an additional dependency on the electron attenuation length and the transmission of the spectrometer. Therefore for a sample consisting of a species i with a concentration N_i, the number of photoelectrons produced from an energy level x is given by (2.30), where J is the photon flux, N_i the concentration of species i, σ the photoionization cross-section of energy level x, T the transmission function of the spectrometer, λ the electron attenuation length, E_k the kinetic energy of the photoelectrons, x the energy level of interest and hν the photon energy.

$$I(E_k, x) = J(h\nu) \cdot N_i \cdot \sigma(h\nu, x) \cdot T(E_k) \cdot \lambda(E_k) \tag{2.30}$$

By defining a sensitivity factor that encompasses the photoionization cross-section, electron attenuation length and analyser transmission, the percentage of atomic species present in an analysis volume may be expressed with (2.31), where x is an atomic species, A_x the atomic concentration of species x, I_x a photoelectron intensity from an energy level in species x, and S_x the sensitivity factor for the said energy level. For correct use of (2.31) a single energy level for each species is chosen, typically the most intense photoelectron intensity.

$$A_x = \frac{I_x/S_x}{\sum I/S} \times 100\% \tag{2.31}$$

For multi-species compounds the molar ratios are known via a chemical formula (R_1 : ... : R_n for n chemical species). For example the formula of Copper Phthalocyanine, $C_{32}N_8Cu$ (hydrogen being undetectable in XPS) would be expressed in molar ratio form as 32 : 8 : 1. The atomic concentration of species x would then be calculated using (2.32), and directly compared to that determined by XPS.

$$A_x = \left(\sum_{i=1}^{n} \frac{R_i}{R_x} \right)^{-1} \times 100\% \tag{2.32}$$

For example the percentage of nitrogen expected in an XPS spectrum of CuPc would be :

$$A_N = \left(\frac{32}{8} + \frac{8}{8} + \frac{1}{8} \right)^{-1} \times 100\% = 19.5\%$$

Quantitative analysis by XPS is extremely powerful as chemically shifted components may be quantified allowing bonding configurations to be identified.

2.3.7. Charging effects

Since photoelectron spectroscopy is a charge-oriented technique electrostatic charging effects may be observed. The most common effect is positive charging, where binding energies are reported erroneously high, and this is often observed for insulators. The mechanism is due to an in-balance in the number of electrons leaving the sample (as photoelectrons) to the number of electrons entering the sample, leading to a build-up of holes in the sample. Samples are required to be in Ohmic contact with ground to allow a flow of electrons (referred to as the sample drain current) to replenish the electrons lost through photoemission. The positive charge constitutes an additional barrier for the electrons, leading to a reduction in their kinetic energy, and hence an increase in their apparent binding energy. Samples with poor Ohmic contacts (rectifying contacts), low doped semiconductors, and insulators, are prone to charging.

A less common effect which is limited to semiconductors is surface photovoltage charging. This effect is due to the dissociation of electron-hole pairs in the semiconductor depletion region and the accumulation of either electrons or holes at the sample surface, with the reduction of surface band-bending and an apparent flat band surface. For p-type semiconductors an accumulation of electrons at the surface occurs leading to erroneously low binding energies being reported. For n-type semiconductors an accumulation of holes at the surface occurs leading to erroneously high binding energies being reported. The effect is proportional to the number of electron-hole pairs that are dissociated, and this is proportional to the number of photons irradiating the sample. High flux sources (synchrotron or flood x-ray sources) are therefore likely to produce this effect.

The photovoltage effect was modelled by Hecht [47] and was successfully used to clarify contradictory results on semiconductor-metal barrier heights in the literature. For a p-type semiconductor the effect is illustrated in Figure 2.7. In panel 1 a photon creates an electron-hole pair in a semiconductor with some surface band-bending, the magnitude of which is known as the barrier height for the holes. The electron-hole pair is then dissociated in the semiconductor depletion region, the electron driven by the electric field to the surface and the hole driven to the bulk. The accumulation of electrons at the surface results in the situation in panel 2 where the bands are flattened. However the presence of electrons at the surface attracts holes from the bulk as depicted in panel 3. Providing the holes have enough thermal energy to overcome the barrier all the surface electrons are removed through recombination. The effect is generally a low-temperature effect as the holes are unable to overcome the barrier at low temperature. Panel 5 depicts the electrical circuit analogy of the situation, where a current source, diode and resistance are in parallel.

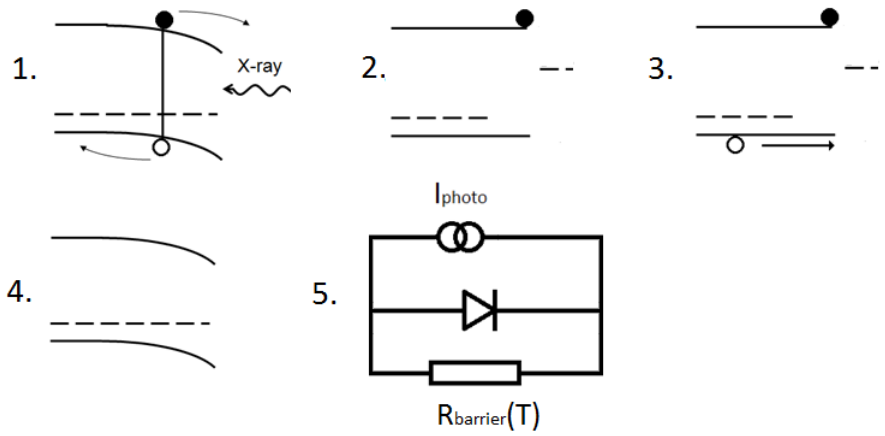

Figure 2.7 Representation of the Hecht photovoltage mechanism. 1) Creation of an electron-hole pair and separation of charges in the depletion region, 2) electron accumulation at the surface causes flattening of the bands, 3) hole current drawn from the bulk neutralises the electrons, 4) equilibrium situation at room temperature, 5) circuit.

Several semiconductor systems have been reported to exhibit surface photovoltage effect. Synchrotron radiation measurements of gallium phosphide [48], zinc selenide [49] and zinc sulphide [50], ultraviolet radiation measurements on silicon [51] and diamond [52], and non-monochromatic Mg Kα measurements on gallium nitride [53] have all revealed surface photovoltage of up to 1.5 eV depending on the experimental conditions. Importantly silicon was shown to have a completely saturated photovoltage (flat bands) at 20 K with high UV flux or at 50 K with mild UV flux, revealing the maximum surface photovoltage shift is equal to the true barrier height. Similarly diamond was shown to have a small surface photovoltage at 300 K which increased rapidly with decreasing temperature, reaching 0.6 eV at 170 K. The gallium nitride results with Mg Kα are more significant since the surface photovoltage is sustained even at high temperature, with p-type GaN exhibiting a photovoltage up to 600 K. The data reveals the Fermi level to shift by 1.5 eV during cooling from 600 K to 300 K at a rate of 55 meV / 10 K, with no sign of approaching saturation value. Since the barrier height on GaN is known to be 2.55 eV there is a possible 1.05 eV shift remaining. The authors report that the Hecht model was unable to account for the surface photovoltage persisting above 300 K since the thermal energy should be enough to overcome the barrier. They note that an unidentified mechanism is sustaining the photovoltage at high temperature.

2.4. References

1. Küttel, O.M., et al., *The preparation and characterization of low surface roughness (111) and (100) natural diamonds by hydrogen plasma.* Surface Science, 1995. **337**(1-2): p. L812-L818.
2. Nandhra, P.S. and et al., *The passivation of Be acceptors in GaAs by exposure to a hydrogen plasma.* Semiconductor Science and Technology, 1988. **3**(4): p. 356.
3. Klauser, R., et al., *The interaction of oxygen and hydrogen on a diamond C(111) surface: a synchrotron radiation photoemission, LEED and AES study.* Surface Science, 1996. **356**(1-3): p. L410-L416.
4. Coppa, B.J., et al., *Structural, microstructural, and electrical properties of gold films and Schottky contacts on remote plasma-cleaned, n-type ZnO{0001} surfaces.* Journal of Applied Physics, 2005. **97**(10).
5. Denisenko, A., et al., *Surface structure and surface barrier characteristics of boron-doped diamond in electrolytes after CF4 plasma treatment in RF-barrel reactor.* Diamond and Related Materials, 2010. **19**(5-6): p. 423-427.
6. Cadman, P., J.D. Scott, and J.M. Thomas, *Identification of functional groups on the surface of a fluorinated diamond crystal by photoelectron spectroscopy.* Journal of the Chemical Society, Chemical Communications, 1975(16): p. 654-655.
7. Balmer, R.S., et al., *Chemical vapour deposition synthetic diamond: materials, technology and applications.* Journal of Physics: Condensed Matter, 2009. **21**(36): p. 364221.
8. Davis, R.F., *III-V NITRIDES FOR ELECTRONIC AND OPTOELECTRONIC APPLICATIONS.* Proceedings of the IEEE, 1991. **79**(5): p. 702-712.
9. Fridman, A., *Plasma Chemistry*. 2008: Cambridge University Press. 1024.
10. Evans, S., et al., *Ultra-violet and X-ray photoelectron spectroscopy studies of oxygen chemisorption on copper, silver and gold.* Faraday Discussions of the Chemical Society, 1974. **58**: p. 97-105.
11. Azmi, B.Z., et al., *An atomic oxygen source for simulation of lower-earth orbit environment.* Journal of solid state technology letters, 1994. **1**(2): p. 5-10.
12. Evans, S. and J.M. Thomas, *The Chemical Nature of Ion-Bombarded Carbon: A Photoelectron Spectroscopic Study of "Cleaned" Surfaces of Diamond and Graphite.* Proceedings of the Royal Society of London. A. Mathematical and Physical Sciences, 1977. **353**(1672): p. 103-120.
13. Kistiakowsky, G.B. and G.G. Volpi, *Reactions of Nitrogen Atoms. I. Oxygen and Oxides of Nitrogen.* The Journal of Chemical Physics, 1957. **27**(5): p. 1141-1149.
14. Vig, J.R., *UV/ozone cleaning of surfaces.* Journal of Vacuum Science & Technology A: Vacuum, Surfaces, and Films, 1985. **3**(3): p. 1027-1034.
15. Venables, J.A. and et al., *Nucleation and growth of thin films.* Reports on Progress in Physics, 1984. **47**(4): p. 399.
16. Bauer, E., *Phänomenologische Theorie der Kristallabscheidung an Oberflächen. I.* Zeitschrift für Kristallographie, 1958. **110**(1-6): p. 372-394.
17. Forrest, S.R., *Ultrathin organic films grown by organic molecular beam deposition and related techniques.* Chemical Review, 1997. **97**: p. 1793.
18. Wikipedia commons. *Growth modes*. Available from: http://en.wikipedia.org/wiki/File:GrowthModes.png.
19. Hill, I.G., et al., *Charge-separation energy in films of pi-conjugated organic molecules.* Chemical Physics Letters, 2000. **327**(3-4): p. 181-188.
20. Molodtsova, O.V. and M. Knupfer, *Electronic properties of the organic semiconductor interfaces CuPc/C60 and C60/CuPc.* Journal of Applied Physics, 2006. **99**: p. 053704.
21. Bao, Z., A.J. Lovinger, and A. Dodabalapur, *Organic field-effect transistors with high mobility based on copper phthalocyanine.* Applied Physics Letters, 1996. **69**(20): p. 3066-3068.
22. Kroto, H.W., et al., *C60: Buckminsterfullerene.* Nature, 1985. **318**(6042): p. 162-163.

23. Lof, R.W., et al., *Band gap, excitons, and Coulomb interaction in solid C_{60}.* Physical Review Letters, 1992. **68**(26): p. 3924.
24. Brumbach, M., D. Placencia, and N.R. Armstrong, *Titanyl Phthalocyanine/C60 Heterojunctions: Band-Edge Offsets and Photovoltaic Device Performance.* The Journal of Physical Chemistry C, 2008. **112**(8): p. 3142-3151.
25. Wikipedia commons. *Copper Phthalocyanine*. Available from: http://commons.wikimedia.org/wiki/File:Copper_phthalocyanine.svg.
26. Wikipedia commons. *Buckminsterfullerene 2D skeletal*. Available from: http://commons.wikimedia.org/wiki/File:Buckminsterfullerene-2D-skeletal.png.
27. Hüfner, S., *Photoelectron spectroscopy. Principles and applications*. 3rd ed. 2003, Berlin: Springer.
28. Martensson, N. and A. Nilsson, *On the origin of core-level binding energy shifts.* Journal of Electron Spectroscopy and Related Phenomena, 1995. **75**: p. 209.
29. Theis, W. and K. Horn, *Temperature-dependent line broadening in core-level photoemission spectra from aluminum.* Physical Review B, 1993. **47**(23): p. 16060.
30. Knapp, J.A., et al., *Temperature dependence of bulk and surface energy bands in copper using angle-resolved photoemission.* Physical Review B, 1979. **19**(6): p. 2844.
31. Riffe, D.M., et al., *Thermal and surface core-electron binding-energy shifts in metals.* Physical Review B, 1992. **45**(11): p. 6216.
32. Coster, D. and R.D. L. Kronig, *New type of auger effect and its influence on the x-ray spectrum.* Physica, 1935. **2**(1-12): p. 13-24.
33. Powell, C.J. and A. Jablonski (2011) *NIST Electron effective attenuation length database*.
34. Watts, J.F. and J. Wolstenholme, *An introduction to surface analysis by XPS and AES*. 2003, Chichester: Wiley. 212.
35. Duke, P., *Synchrotron Radiation: Production and Properties*. Oxford Series on Synchrotron Radiation, ed. J. Chikawa, J.R. Helliwell, and S.W. Lovesey. 2000, Oxford, UK: Oxford University Press. 266.
36. Purcell, E.M., *The Focusing of Charged Particles by a Spherical Condenser.* Physical Review, 1938. **54**(10): p. 818.
37. Kevan, S.D., *Design of a high-resolution angle-resolving electron energy analyzer.* Review of Scientific Instruments, 1983. **54**(11): p. 1441-1445.
38. SPECS GmbH. *Extended Range Channel Electron Multiplier (CEM)*. Available from: http://www.specs.de/cms/front_content.php?idcat=181.
39. Richter, L.J. and W. Ho, *Position-sensitive detector performance and relevance to time-resolved electron energy loss spectroscopy.* Review of Scientific Instruments, 1986. **57**(8): p. 1469-1482.
40. Manning, P.P., et al., *A fast and flexible multichannel electron detector with parallel readout for photoelectron spectroscopy.* Nuclear Instruments and Methods in Physics Research Section A: Accelerators, Spectrometers, Detectors and Associated Equipment, 1997. **392**(1-3): p. 345-348.
41. Gori, L., et al., *An embedded control and acquisition system for multichannel detectors.* Nuclear Instruments and Methods in Physics Research Section A: Accelerators, Spectrometers, Detectors and Associated Equipment, 1999. **431**(1-2): p. 338-346.
42. Nambu, A., et al., *An ultrahigh-speed one-dimensional detector for use in synchrotron radiation spectroscopy: first photoemission results.* Journal of Electron Spectroscopy and Related Phenomena, 2004. **137-140**: p. 691-697.
43. Langstaff, D.P. and T. Chase, *A multichannel detector array with 768 pixels developed for electron spectroscopy.* Nuclear Instruments and Methods in Physics Research Section A: Accelerators, Spectrometers, Detectors and Associated Equipment, 2007. **573**(1-2): p. 169-171.

44. Boyle, W.S. and G.E. Smith, *Charge coupled semiconductor devices.* Bell System Technical Journal, 1970. **49**(4): p. 587.
45. Hamamatsu Photonics, *MCP & MCP Assembly. Selection Guide*. 2007.
46. Fairley, N. and A. Carrick, *The Casa Cookbook*. 2005, Cheshire, UK: Acolyte Science.
47. Hecht, M.H., *Photovoltaic effects in photoemission studies of Schottky barrier formation.* Journal of Vacuum Science & Technology B: Microelectronics and Nanometer Structures, 1990. **8**(4): p. 1018-1024.
48. Evans, D.A., et al., *The interaction of platinum with GaP(110) - band bending and surface photovoltage effects.* Applied Surface Science, 1992. **56-8**: p. 233-241.
49. Evans, D.A., et al., *Metal overlayers on the MBE-grown ZnSe(001) surface.* Applied Surface Science, 1996. **104**: p. 240-247.
50. Wolffframm, D., et al., *Gold and silver Schottky barriers on ZnS(110).* Journal of Applied Physics, 2000. **87**(8): p. 3905-3911.
51. Demuth, J.E., et al., *Photoemission-Based Photovoltage Probe of Semiconductor Surface and Interface Electronic Structure.* Physical Review Letters, 1986. **56**(13): p. 1408.
52. Bandis, C. and B.B. Pate, *Room temperature photovoltaic charging in photoemission from diamond.* Surface Science, 1996. **345**(1-2): p. L23-L27.
53. Long, J.P. and V.M. Bermudez, *Band bending and photoemission induced surface photovoltages on clean n- and p-GaN (0001) surfaces.* Physical Review B, 2002. **66**: p. 121308.

3. Instrumentation

In this section details of the instruments used in this work is presented.

3.1. Vacuum system

The vacuum system consisted of three stainless steel chambers; an analysis chamber, a preparation chamber, and a fast load-lock; each isolated from each other with a UHV hand-valve, and a gas-line system. A schematic of the system is presented in Figure 3.1 and a photograph in Figure 3.2.

The analysis chamber was pumped by an ion pump and a titanium sublimation pump (TSP) and had a base pressure of around $1x10^{-10}$ mbar. The chamber was equipped with a twin anode x-ray gun, electron analyzer, rear-view LEED unit, a double k-cell for depositing CuPc and C60 and an aluminium k-cell. The k-cells had were collimated and shuttered and were positioned to avoid contamination of the analyser lens and x-ray head. A photograph of the sample stage during real-time XPS annealing is given in Figure 3.3.

The preparation chamber was pumped by a turbo pump and TSP filaments and had a base pressure of $5x10^{-10}$ mbar. The chamber was equipped with an ion gun, mass spectrometer and a silver k-cell.

The load-lock was pumped by a turbo pump and had a base pressure of $5x10^{-7}$ mbar. A magnetic arm was attached for moving samples between chambers. A flange with a Hoke Gyrolock ¼-inch pipe fitting was attached to the load-lock, above which a stainless steel plate, into which a second ¼-inch pipe fitting had been fastened, was attached. A Pyrex glass capillary was set between the pipe fittings, with Teflon ferrules to form a vacuum seal, which

reached within 20 mm of the sample surface. The capillary served as a gas inlet and as a principle component of the in-situ microwave plasma source. A tungsten filament was included for sample heating.

A system of ¼ inch stainless steel piping was used to connect gas bottles to the vacuum system. The gas-lines were pumped by a turbo and rotary pump for quick evacuation and a high vacuum base pressure. The lines were connected to the glass capillary via a needle-valve for pressure control.

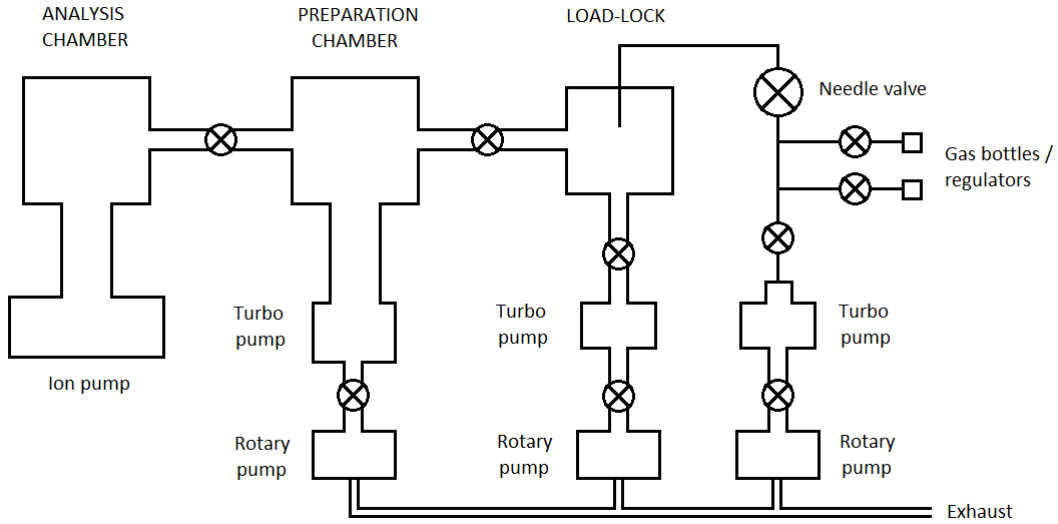

Figure 3.1 Chamber arrangement with pumping components. The gas-line system is on the right-hand side, connected to the load-lock.

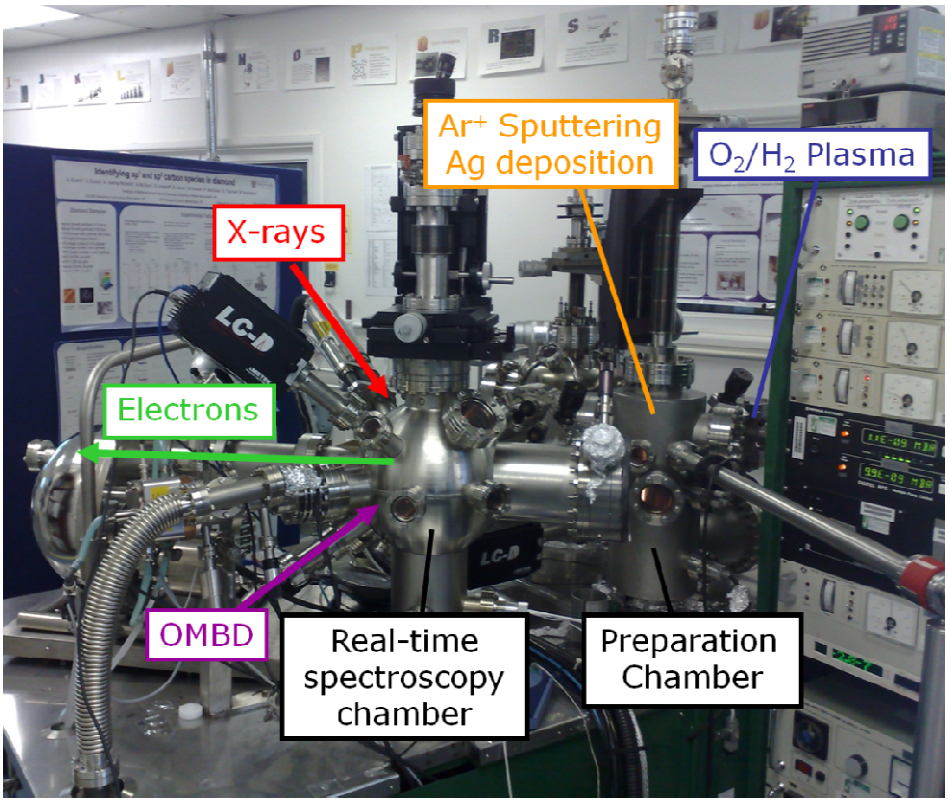

Figure 3.2 Photograph of the equipment

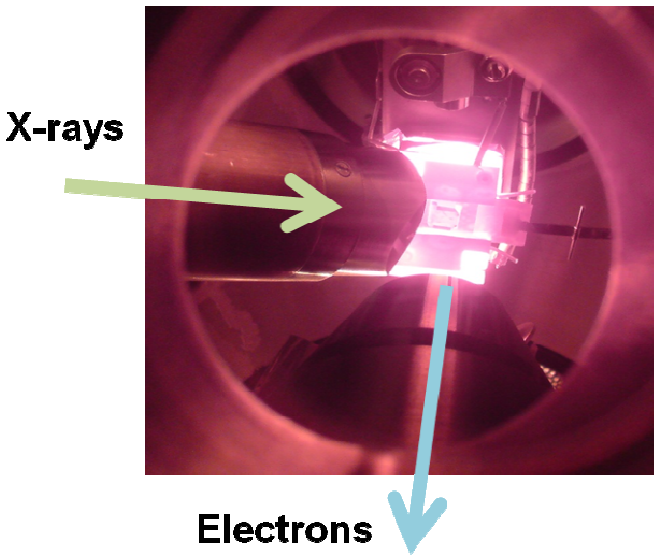

Figure 3.3 Photograph of the sample stage, x-ray gun and electron analyser during a real-time XPS heating cycle. The sample may be seen at the centre of the image. The x-ray flux and photoelectron signal is indicated.

3.2. X-ray source

A VG XR3E2 twin anode x-ray source operated at 20 mA, 15 kV, provided non-monochromatic x-rays of either 1253.6 eV at 0.7 eV line-width from magnesium or 1486.6 eV at 0.9 eV line-width from aluminium.

The x-ray anode to sample distance was determined by measuring the sample drain current as a function of x-ray emission current at two x-ray gun positions, and the data is presented in Figure 3.4. By considering the x-ray flux to be proportional to the inverse square of the distance the ratio of the gradients of the data at the two x-ray gun positions gives the relative flux change, giving (3.1), where m represents the gradient. From this relationship the value of r is found to be 76.9 ± 5.9 mm.

$$\frac{m_r}{m_{r+15mm}} = \left(\frac{r_{r+15mm}}{r}\right)^2 \qquad (3.1)(4.5)$$

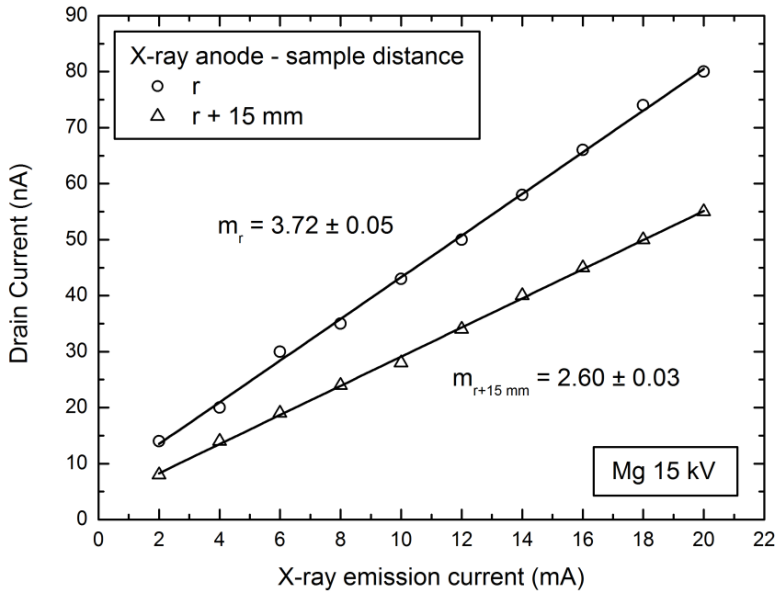

Figure 3.4 Drain current measured on (111) diamond with Mg anode, 15 kV, for varying emission currents, at two linear drive settings.

3.3. Electron Analyser

The electron analyser was a SPECS Phoibos 100 with a mean hemisphere diameter of 100 mm and spacing of 50 mm. The 1.5 kV power supply was used and the Large Area lens mode. A 3 mm entrance slit was used for all work with no exit slits and the iris aperture was used at the 10 mm setting (± 3° acceptance).

A 640 x 480 pixel PixelFly CCD detector was used in conjunction with a P43 phosphorescent screen and 40 mm double micro-channel plate (MCP) operating at 1.4 kV. The CCD had a 12-bit analogue-to-digital converter allowing 4095 levels of intensity. A schematic of the exit plane, MCP and CCD detector is shown in Figure 3.5. The exit plane had an usable area of 40 mm x 20 mm which in conjunction with the CCD allowed 477 pixels across the energy dispersive direction for snapshot spectrum.

Software

A computer running Microsoft Windows XP was used to run software for controlling the electron analyser and communicating with other instruments and collecting data. The analyser was supplied with control software, known as SPECSLAB2, that facilitated full control of the analyser and CCD detector for performing conventional scanned spectra. For analysis of the photoelectron spectroscopy data CasaXPS was used, allowing core-level component fitting, background subtraction, satellite subtraction, and quantification.

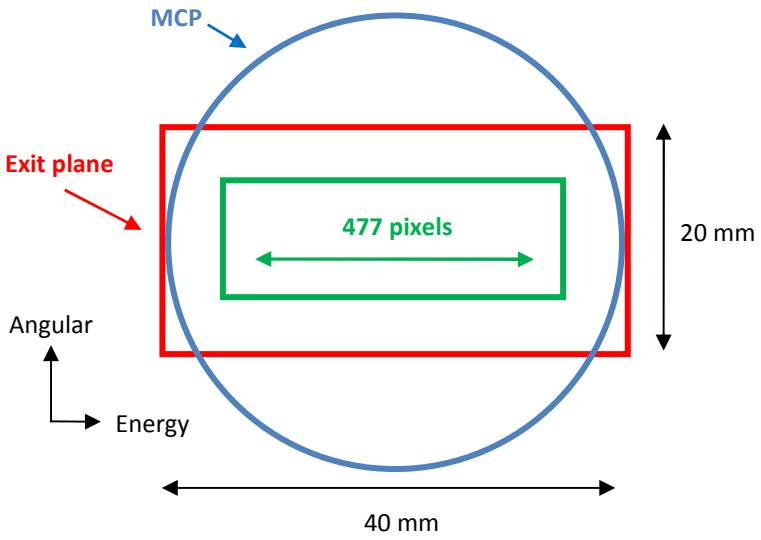

Figure 3.5 Schematic of the exit plane of the analyser, the exit plane shown in red, the MCP in blue and the CCD image in green. Energy and angular directions have been indicated.

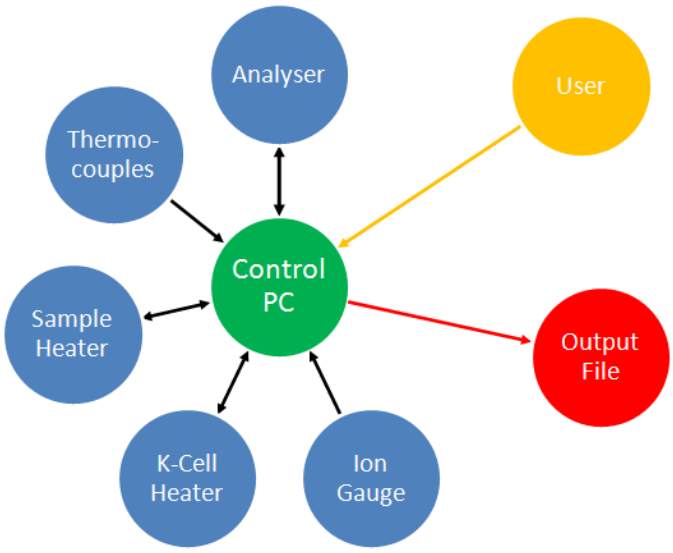

Figure 3.6 Data flow in the real-time photoelectron spectroscopy measurements.

For performing real-time spectroscopy software was written in-house with assistance from Dr. D. P. Langstaff, Aberystwyth University, using National Instruments LabView for controlling the analyser, acquiring data from the CCD and several instruments and writing output data files. Additional software allowed data to be acquired from a pressure gauge and nine thermocouples and to control a programmable power supply unit that supplied power for the sample heater and the k-cells. Figure 3.6 shows the data flow during a real-time photoelectron spectroscopy experiment.

The output of a real-time spectroscopy experiment is a single file which contained the experimental variables (time, pressure, nine temperatures, heater current, heater voltage) and the snapshot spectrum. Files were composed of 14 columns of experimental variables and 477 columns of CCD pixel intensities, with each row representing one measurement.

The intensity measurements were converted into VAMAS files which could then be sequentially fitted in CasaXPS. The fitted spectrum data was then combined with the experiment variables in OriginLab Origin Pro 8 for analysis.

The snapshots were fitted in CasaXPS with a GL(30) line-shape (Voight function having a 30% Lorentzian contribution) with a Shirley background [1]. The fit parameters were smoothed with an adjacent-averaging algorithm; the peak positions smoothed with a 5 point average, the widths with a 20 point average, and the intensities with a 20 point average.

Energy scale

For scanned spectrum the analyser binding energy scale was calibrated by referencing to the standard values of Cu $2p_{3/2}$ and Au $4f_{7/2}$ core-levels, 932.66 eV and 84.00 eV respectively. A copper sample with a gold wire pressed into the surface was sputter-annealed and a survey spectrum of the as-loaded and clean surface are presented in Figure 3.7 left hand panel a) and b) respectively, along with the core-levels in the right hand panel.

The dispersion at the exit plane in eV/pixels was determined by measuring the peak position of a narrow core-level with different values of applied bias (causing known energy shifts). The gradient of a linear fit of applied bias against peak position gives the dispersion constant, which are listed in Table 3.1, along with the maximum energy window measurable. A binding energy scale was established for each snapshot spectrum settings by comparing a snapshot spectrum to a scanned spectrum of a core-level and applying (2.34).

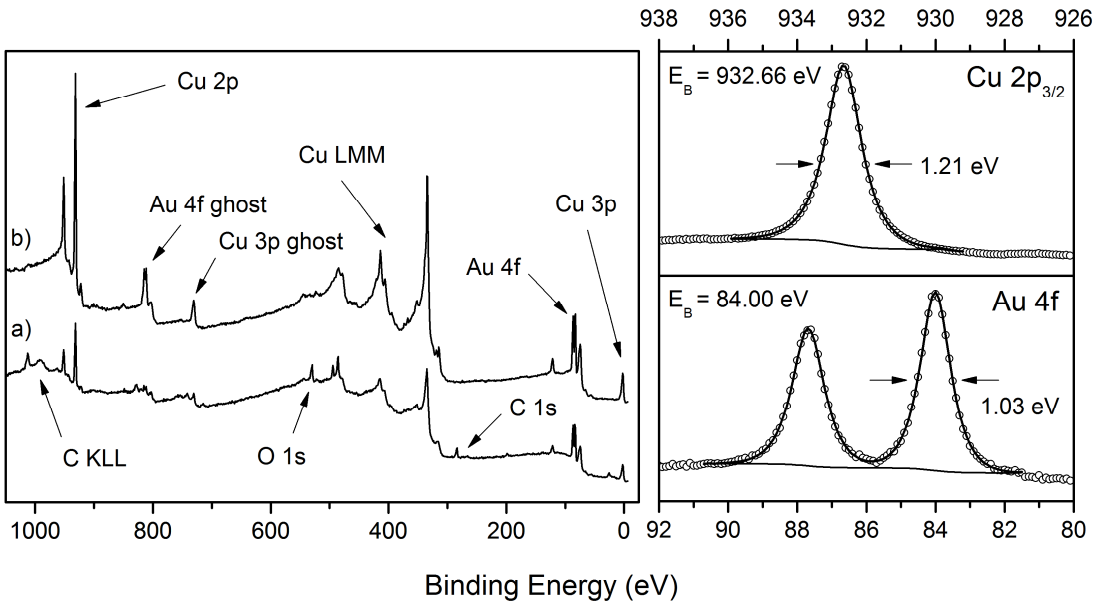

Figure 3.7 Calibration sample. Spectrum shown in left hand panel are a) as-loaded, b) sputtered. Spectrum shown in right hand panel are Cu $2p_{3/2}$ and Au 4f, fitted by a single GL component and double GL component respectively, with a Shirley background.

Pass energy (eV)	Dispersion ± 0.5 (meV / pixel)	Maximum energy window (eV)
100	35	16.7
60	22	10.5
40	14	6.7
20	7	9.5

Table 3.1 Values of the energy dispersion determined in the applied bias method for various pass energies.

Resolution

Using (2.35) the resolution of the analyser (mean diameter 100 mm and 3 mm entrance slit) at 100 eV and 20 eV pass energy is calculated to be 1.5 eV and 0.30 eV respectively. The x-ray source has a linewidth of 0.7 eV and using (2.36) the resolution at 100 eV and 20 eV pass energy is 1.66 eV and 0.76 eV respectively.

The effect of changing the pass energy on the width and intensity of snapshot spectrum was measured for a narrow and intense core-level. Figure 3.8 shows snapshots of the C 1s core-level of diamond at four pass energy values, each spectrum having been normalised in intensity. A shift to higher pixel number is observed with decreasing pass energy; this is a property of the analyser and prohibits comparison of energies measured at different pass energies unless a correction factor is applied. The intensity (determined from the area) and width of the snapshots as a function of pass energy are presented in Figure 3.9. The intensity values have been normalised to the intensity of 100 eV pass energy. The widths are expressed both in terms of pixels and in energy. At 40 eV pass energy the FWHM of the snapshot spectrum (1.5 eV) was found to be slightly broader than the FWHM of the same core-level measured by scanning at 20 eV pass energy (1.4 eV).

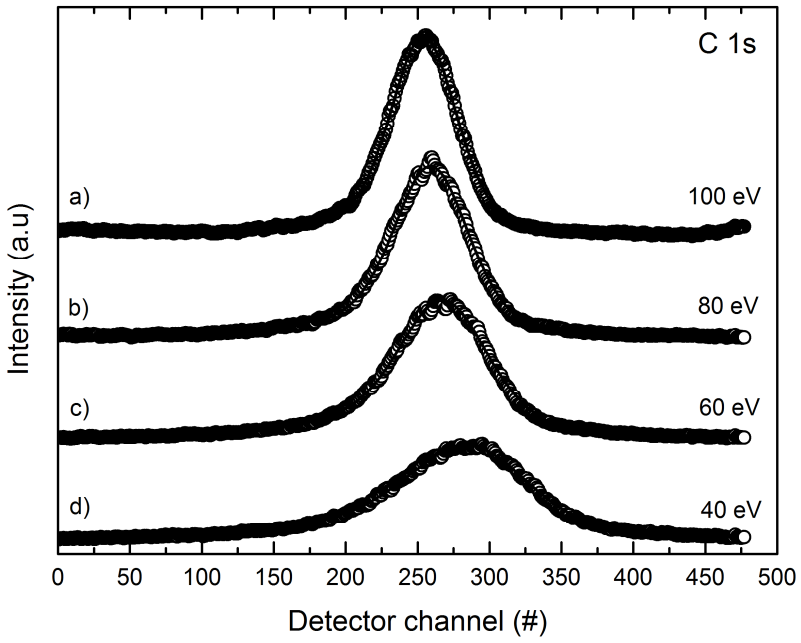

Figure 3.8 Snapshot spectrum of C 1s of diamond measured with different pass energy.

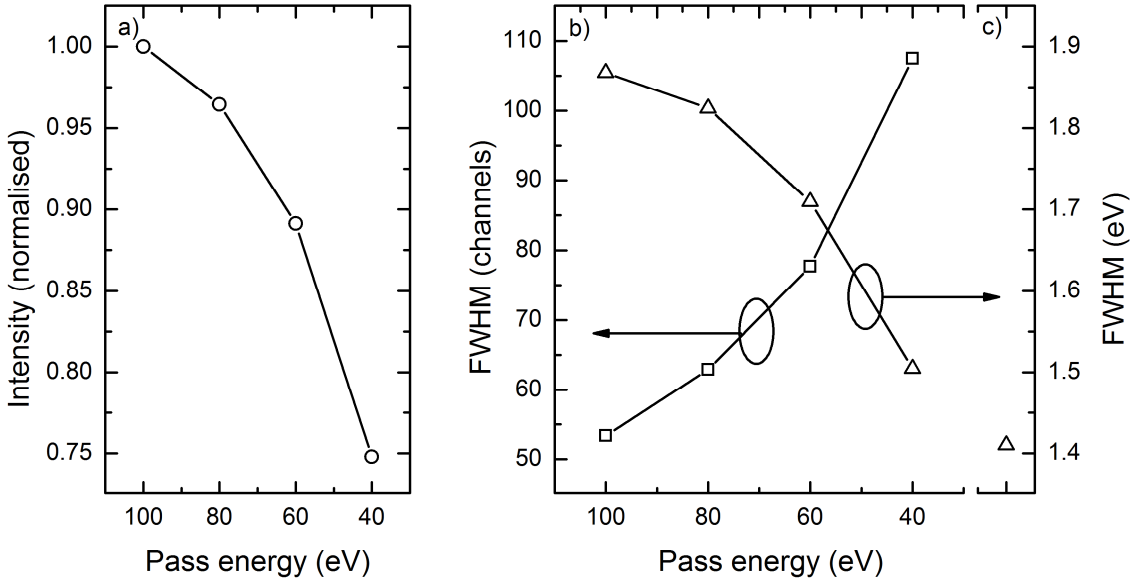

Figure 3.9 Intensity and width of snapshot spectrum; panel a) gives the intensity variation, panel b) the width in number of pixels and energy, and panel c) the same core-level measured in scanning mode with 20 eV pass energy.

3.4. Sample stage and sample holder

The sample stage was constructed around a Boraelectric® heater (boron nitride with graphitic tracks) measuring 24 mm x 34 mm. The faceplate, shown in Figure 3.10, left hand, was 0.3 mm tantalum with two 1 mm tantalum wires spot-welded onto the back as guide rails for the sample holders. A photograph of the sample stage is given in Figure 3.11.

An insulated wire attached to a vacuum feedthrough on the manipulator allowed for drain current measurements and biasing of the sample. A thermocouple was bolted to the front of the faceplate to directly measure the temperature.

The sample holder was made out of 0.125 mm molybdenum and a schematic is shown in Figure 3.10, right hand. Samples were held onto the sample holder by sliding underneath a molybdenum template that was held under the foldable sides.

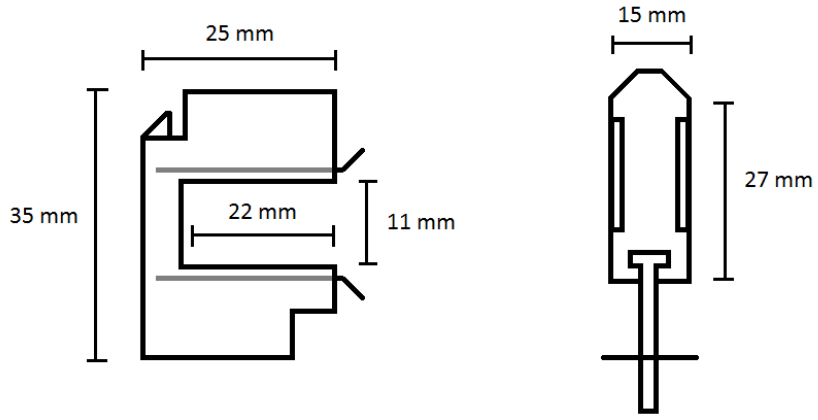

Figure 3.10 Drawings of the faceplate (left) and the sample holder (right). The faceplate had a 3 mm orthogonal turn to act as an end-stop for the sample holders. Two tantalum wires on the reverse that act as guide rails are shown in grey.

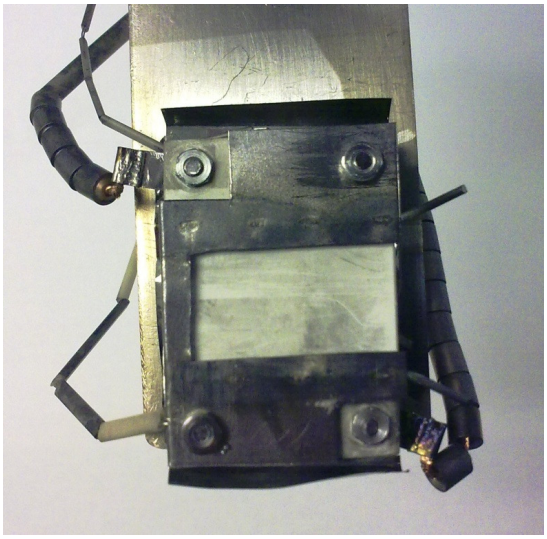

Figure 3.11 Photograph of the stage assembly. Foreground is the faceplate, followed by the Boraelectric® heater (white). First heat shield can be seen above and below the heater. Top left and bottom right are the heater power wires, with ceramic insulation. Bottom left is the faceplate thermocouple, while the ceramic insulation of the second thermocouple can be seen above the top left heater connector.

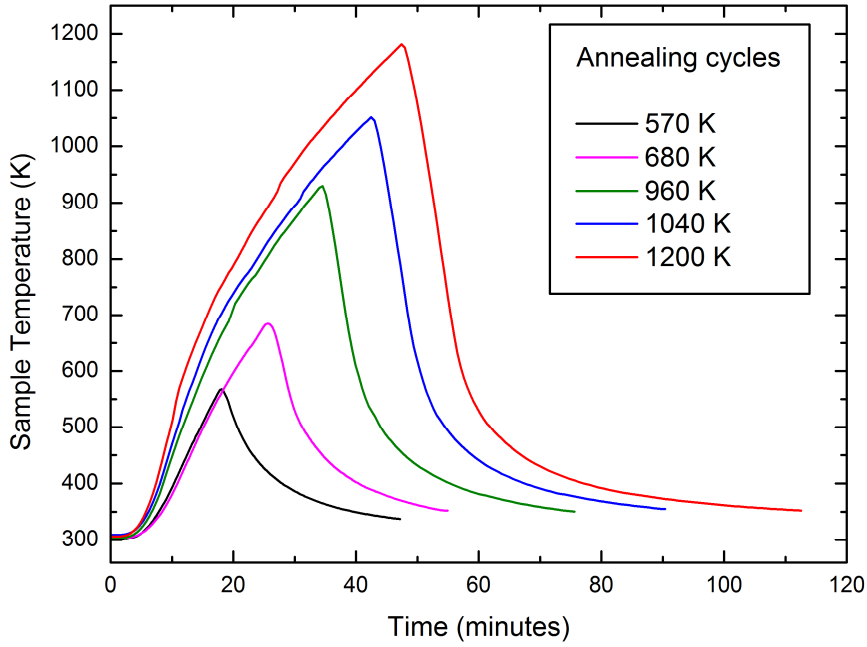

Figure 3.12 Temperature-time profile of heating cycles used in this work. The rate of cooling was found to be linear between high temperature and 570 K. Below 570 K the cooling became exponential.

Standardised annealing cycles were used in this work through programmed current profiles on the computer controlled PSU. Figure 3.12 shows the temperature-time profile of the annealing cycles used in the work. Table 3.2 lists the heating parameters (rate of change of temperature, heater current and voltage) during the heating part of the cycle, and Table 3.3 the rate of change of the temperature during cooling to 680 K.

Maximum sample temperature (K)	Heating cycle				
	Time (min)	Peak heater		Rate of change	
		Current (A)	Power (W)	Sample temperature (K min^{-1})	Heater power (W min^{-1})
570	16.7	1.7	20.1	34.2	1.2
680	25.0	2.4	33.9	27.2	1.4
920	33.3	4.5	102.1	27.6	3.1
960	36.7	5.0	125.7	26.2	3.4
1040	41.7	6.0	172.7	25.0	4.1
1200	46.7	8.0	310.4	25.7	6.7

Table 3.2 Heating cycles parameters used in this work; the time taken to reach maximum temperature from room temperature, the heater current and power at maximum temperature, and the rate of change of sample temperature and heater power above 680 K.

Maximum sample temperature (K)	Cooling to 570 K	
	Time (min)	Sample temperature rate of change (K min^{-1})
680	2.7	48.0
920	6.0	59.4
960	7.0	56.4
1040	8.5	55.8
1200	10.3	58.2

Table 3.3 Cooling parameters between high temperature and 570 K where the temperature change was linear. Below 570 K the change become exponential.

3.5. In-situ microwave plasma source

An in-situ microwave excited plasma source was built to generate active oxygen and active hydrogen for surface processing. The source was adapted from a system used by Dr. S. Evans of the University of Wales, Aberystwyth [2], and is similar to other systems reported in the literature [3, 4].

The plasma source was created around the glass capillary set into the load-lock chamber of the vacuum system. A brass microwave was held in the centre of the unit by two micro manipulators capable of movement in orthogonal directions, with the capillary running through an opening in the cavity. A tuning stub allowed the resonance frequency of the cavity to be adjusted, and an air inlet allowed compressed air to be used for cooling as the unit dissipated a large amount of heat when in operation.

Microwave power was provided by an EMS200 Mark II Microtron at 2.45 GHz with a maximum output of 200 W. A reflected power meter was connected between the generator and the cavity to aid tuning of the cavity which was done by adjustment of the tuning stub.

The resonance cavity was 100 mm from the sample and the capillary 25 mm from the sample. This modification is different to that reported by Evans [2], and later Raftery [5], due to the closer proximity of the cavity to the sample and the guiding action of the capillary for the gas molecules.

It was expected that the plasma would emit UV photons due to the emission lines of the gasses being used [6]. UV radiation is a direct hazard to the skins and eyes but also an in-direct hazard through the production of ozone by interaction of 185 nm photons with atmospheric oxygen [7]. Since Pyrex glass does not transmit below 310 nm [8] only long

wave (UVA) photons were emitted and consequently no ozone was produced during operation of the unit. To filter out the remaining UVA photons the unit was encased in a sheet of transparent plastic which did not transmit below 400 nm. Figure 3.13 is a photograph of the unit while being used.

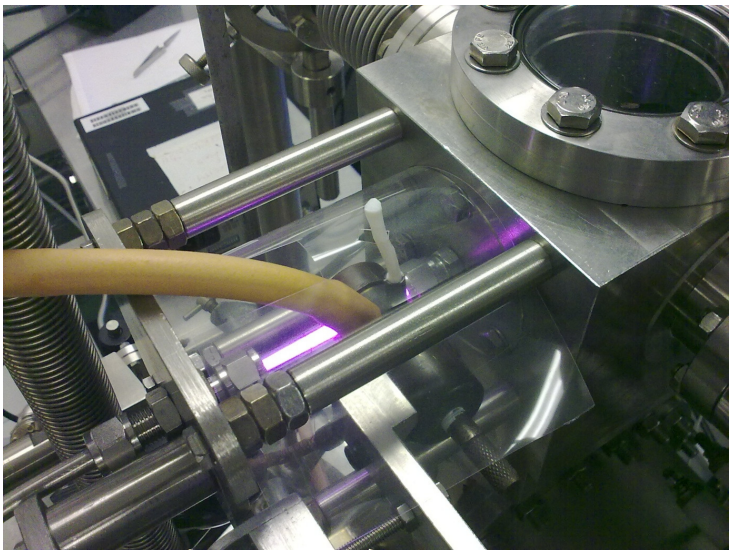

Figure 3.13 Microwave plasma source in operation. The resonance cavity is at the centre of the image with the Pyrex capillary (with glowing plasma) set through the middle. The orange tubing is the cooling air supply. The load lock loading window can be seen at the top-right.

Oxygen plasma was created with a pressure of 4×10^{-4} mbar of nitric oxide, 100 W of microwave power with 5 W of reflected power was used.

Hydrogen plasma was created with a pressure of 4×10^{-4} mbar of hydrogen gas, 120 W of microwave power and 5 W of reflected power. The radiative heating filament was operated at 30 W (white hot) in a base vacuum of 6×10^{-8} mbar, ensuring at all times the sample surface was not exposed to the filament (only the back of the sample holder).

3.6. Sputter ion gun

A Physical Electronics model 04-131 sputter ion gun was used to argon ions sputter samples and was positioned approximately 5 cm from the sample. The angle of the sample relative to the sputter gun could be adjusted between normal and glancing incidence allowing control of the sputtering rate. A partial pressure of $5x10^{-5}$ mbar argon was required for sufficient ion production.

3.7. Thin film materials

Silver wire was 99.99%, 0.5 mm diameter from Advent Materials and Aluminium was 99.999%, 1.0 mm diameter also from Advent Materials. The evaporation rate of silver was determined with a quartz crystal oscillator at three K-cell heater powers to provide high and low evaporation rates. Figure 3.14 shows the coverage against time with linear fits giving the evaporation rates. The geometry factor is a correction for the substrate distance from the cell compared to the crystal oscillator distance.

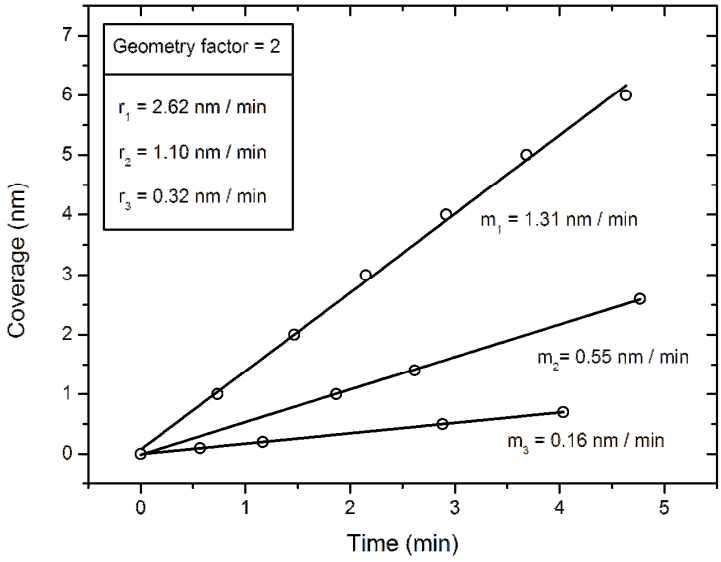

Figure 3.14 Silver rate determined from a crystal oscillator. The geometry factor reflects the difference in distance between the sample stage and the crystal.

The organic materials used were provided by Sigma Aldrich; CuPc (CAS 147-14-8, Aldrich 546683-2G, >99% dye content) and C60 (CAS 99685-96-8, Sigma-Aldrich 572500-500MG, 99.9% sublimed).

CuPc was evaporated onto a silver substrate followed by evaporation of C60 onto the CuPc film. A survey spectrum of CuPc and C60 is presented in Figure 3.15. For the CuPc the atomic concentration is given in Table 3.4, the C 1s, N 1s and Cu $2p_{3/2}$ core-levels in Figure 3.16 and the fitting parameters in Table 3.6. For the C60 the C 1s core-level is presented in Figure 3.17 and the fitting parameters in Table 3.5.

The chemical composition of the CuPc film is exactly as expected for the chemical structure of CuPc. Component fitting of the C 1s core-level reveals two chemical environments with a satellite structure giving four peaks in all, while the N 1s core-level was fitted with a main component and a satellite peak. The relative intensity of the components is the same as reported by other workers on the CuPc molecule [9, 10], revealing the molecule to remain intact after thermal evaporation.

The C 1s core-level of C60 was fitted with a single peak and the plasmon structure was fitted with numerous peaks similar to the measurements of Leiro et al [11] who based their component fitting on theoretical calculations of the C60 molecule by Enkvist et al [12]. The component fits are surprisingly similar; the relative positions, width and intensities are all in agreement. The measurement reveals the C60 film retains the fullerene character following thermal evaporation. A small nitrogen core-level is observed at a binding energy of 400 eV in the C60 survey spectrum, due to insufficient coverage to fully attenuate the CuPc film substrate.

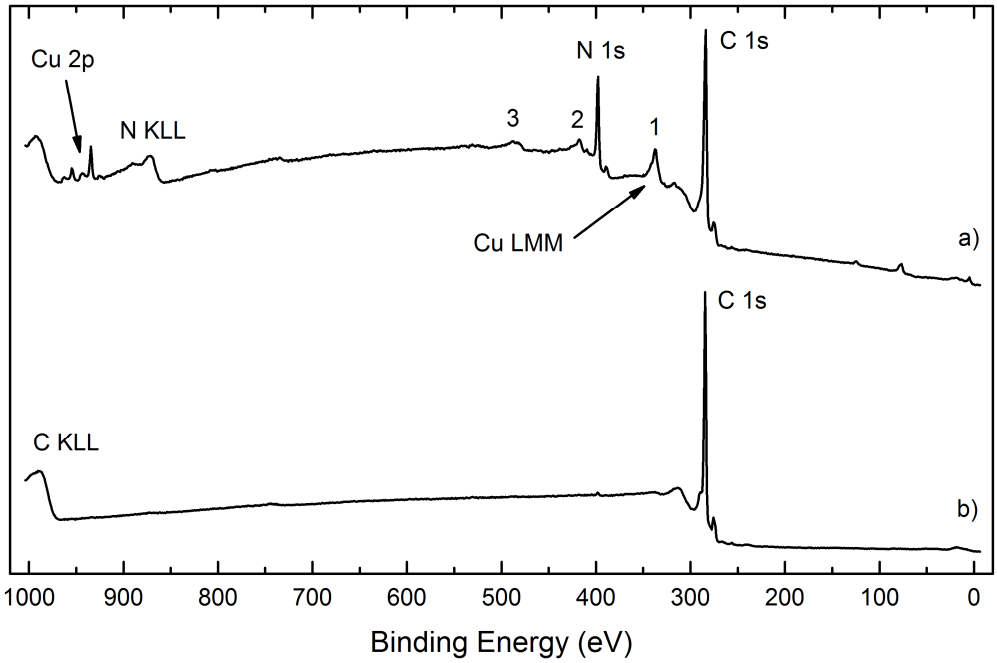

Figure 3.15 Survey spectrum of the two organic compounds; a) CuPc and b) C60. The Cu LMM structure is labelled 1, 2, 3 in the CuPc spectrum.

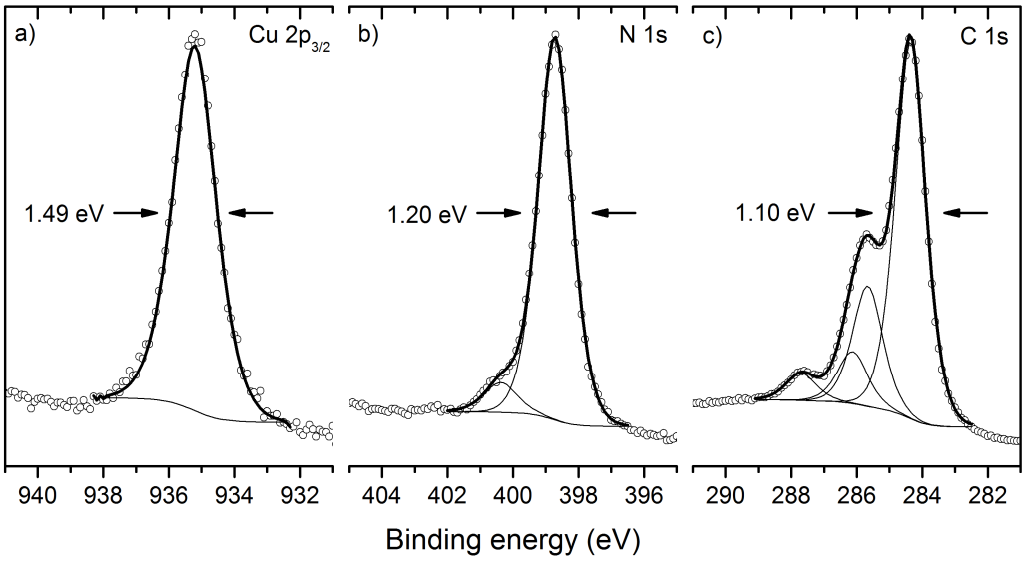

Figure 3.16 CuPc core-levels; a) Cu $2p_{3/2}$, b) N 1s, and c) C 1s

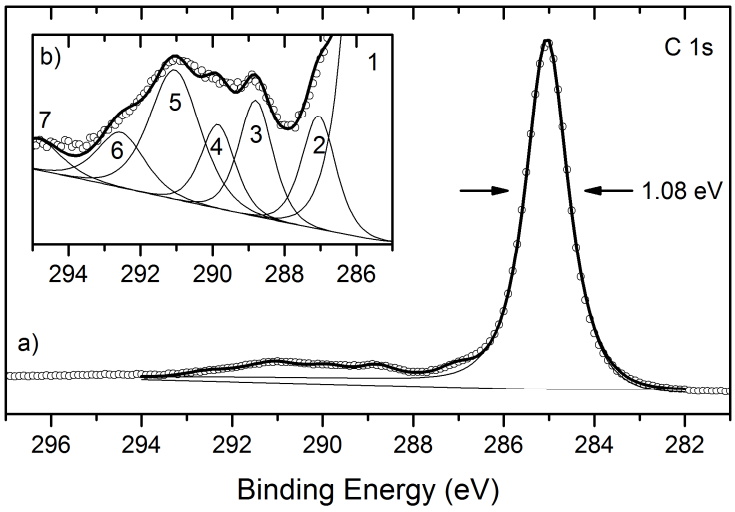

Figure 3.17 C60 C 1s core-level. Inset is the plasmon region.

Element	Concentration (%)	
	Calculated	Measured ± 1.0
C	78.0	78.5
N	19.5	19.5
Cu	2.4	2.5

Table 3.4 Component fitting parameters for the C 1s and N 1s core-levels of copper phthalocyanine.

Component	Binding Energy (eV)		FWHM (eV)	Lineshape	Relative intensity (%)
	Absolute	Relative			
1	285.05	-	1.10	GL(84)	100
2	287.05	2.00	1.10	GL(60)	4.6
3	287.95	2.90	1.10	GL(60)	1.5
4	288.80	3.75	1.10	GL(60)	4.7
5	289.85	4.80	1.10	GL(60)	3.4
6	291.05	6.00	1.65	GL(60)	7.8
7	292.55	7.50	1.54	GL(60)	3.1

Table 3.5 Component fitting parameters for the C 1s core-level of C60.

Peak	Component	Binding Energy (eV)		FWHM (eV)	Lineshape	Concentration (%)		C-N Ratio	
		Absolute	Relative			Component	Total	Component	Total
C 1s	C-C	284.35	0	1.09	GL(68)	52.9	80.2	3.01	4.05
	C-C satellite	286.12	1.77	1.09	GL(66)	7.3			
	C-N	285.66	1.31	1.12	GL(58)	16.1			
	C-N satellite	287.69	3.34	1.12	GL(58)	3.9			
N 1s	C-N / C-N-Cu	854.61	0	1.19	GL(63)	18.2	19.8	-	
	C-N satellite	852.89	1.72	1.19	GL(63)	1.6			

Table 3.6 Component fitting parameters for the C 1s and N 1s core-levels of copper phthalocyanine.

3.8. References

1. Fairley, N. and A. Carrick, *The Casa Cookbook*. 2005, Cheshire, UK: Acolyte Science.
2. Evans, S. and J.M. Thomas, *The Chemical Nature of Ion-Bombarded Carbon: A Photoelectron Spectroscopic Study of "Cleaned" Surfaces of Diamond and Graphite.* Proceedings of the Royal Society of London. A. Mathematical and Physical Sciences, 1977. **353**(1672): p. 103-120.
3. Cairns, R.B. and J.A.R. Samson, *Total Absorption Cross Section of Atomic Oxygen below 910A.* Physical Review, 1965. **139**(5A): p. A1403.
4. B.Z.Azmi, et al., *An atomic oxygen source for simulation of lower-earth orbit environment.* Journal of solid state technology letters, 1994. **1**(2): p. 5-10.
5. Raftery, E., *Applications of electron spectroscopy in inorganic and surface chemistry*. 1985, University of Wales: Aberystwyth.
6. Lide, D.R., ed. *CRC Handbook of Chemistry and Physics*. 73rd ed., CRC Press.
7. Calvert, J.G. and J.N. Pitts, *Photochemistry*. 1966, Wiley: New York. p. 205-209, 687-705.
8. ESCO Products. *Pyrex® (Corning 7740)*. Available from: http://www.escoproducts.com/html/pyrex_r_.html.
9. Evans, D.A. and et al., *Copper phthalocyanine on InSb(111)A—interface bonding, growth mode and energy band alignment.* Journal of Physics: Condensed Matter, 2003. **15**(38): p. S2729.
10. Schwieger, T., et al., *Electronic structure of the organic semiconductor copper phthalocyanine and K-CuPc studied using photoemission spectroscopy.* Physical Review B, 2002. **66**(15): p. 155207.
11. Leiro, J.A., et al., *Core-level XPS spectra of fullerene, highly oriented pyrolitic graphite, and glassy carbon.* Journal of Electron Spectroscopy and Related Phenomena, 2003. **128**(2-3): p. 205-213.
12. Enkvist, C., et al., *C1s shakeup spectrum of C60: Global charge-transfer satellites and their relation to the x-ray threshold singularities in macroscopic systems.* Physical Review B, 1993. **48**(19): p. 14629.

4. Metals

In this section details of the investigations into the surface processing of metals is presented. Of particular interest is the effect of annealing and the formation of organic interfaces.

4.1. Introduction

There is much interest in the surfaces of metals and their oxides due to their use as catalysts; gold [1], titanium dioxide [2], oxides [3] being examples. Metals are also used universally as electrical contact materials, with gold and copper most widely used. Alloyed metals are extremely important due to their electrical, thermal and mechanical properties [4] but also due to their use as catalysts [5, 6].

Metals are typically polycrystalline being composed of many small crystals known as grains. The size of the grains and the boundaries between the grains are important in determining the physical properties of the metal. Metals that are composed of a single crystal have superior mechanical, electrical and thermal properties compared to polycrystalline metals. However single crystal metal require energetically demanding methods as the Czochralski process for production and are therefore used only for the most demanding applications, such as turbine blades [7].

Annealing a metal may alter the surface by the removal of adsorbed species, diffusion of species from the bulk into the surface and surface structure reconstruction, and is therefore expected to alter the chemical and electronic properties of the surface. Metal surfaces may be modified with organic semiconductor thin-films, for example C60 has been shown to passivate aluminium, preventing oxidation [8]. Organic semiconductors may also be used to create electronic devices and their interfaces with metal surfaces are of interest. Organic

based devices show great promise for cheaper, flexible, low power-consumption and low weight electronic devices [9]. An important example is photovoltaic devices, where conversion of sunlight into electrical power is possible with organic semiconductors, first reported in 1986 [10]. Presently copper [11] and tin [12] phthalocyanine are among the most promising organic semiconductor materials. Knowledge of the effects of the surface processing of metals is therefore essential for the optimization of applications such as catalysis and X-ray Photoelectron Spectroscopy (XPS) may be used to provide this information.

XPS has been extensively used to probe metal surfaces and a review of investigations into single crystal surfaces may be found in Woodruff and Delchar [13]. Studies of the surface processing of metals have relied on measuring the surface before and after processing, rather than during the actual process. The ability to perform XPS during the surface processing of metals is highly desirable as it offers a probe of chemistry and energetics during the processing. Such real-time information is useful to reliably determine optimum processing conditions and times.

4.2. Experimental

Three metal surfaces were investigated; copper (9 mm x 17 mm x 0.75 mm) and gold (11 mm x 7 mm x 0.25 mm) from Advent Materials (99.99 % purity) and a thick aluminium film evaporated in-situ. The Al film was evaporated onto a sputter cleaned stainless steel foil, and the chamber pressure during evaporation was 5×10^{-9} mbar.

Ex-situ preparation of the copper and gold samples was cleaning with Brasso® fluid followed by rubbing with paper. Samples were then agitated in acetone before affixing in a pre-annealed sample holder and loading into the system. In-situ preparation of the copper and gold surfaces consisted of numerous cycles of oxygen plasma followed by annealing at 1000 K. The surfaces were then either sputtered-annealed or sputtered-only. The argon ion sputtering was performed normal incidence in a pressure of 5×10^{-5} mbar of argon at 700 V for either 20 or 30 minutes and the by post-sputtering annealing at 1000 K.

Real-time measurements were performed with the parameters given in Table 4.1. When the secondary electron cut-off was desired a bias of -5 V had to be applied to the sample, and all kinetic energy values had to be increased by +5 V to allow for this.

Peak	Energy (eV)		Acquisition time (s)
	Kinetic	Pass	
Au 4f	1163	60	2
Al 2s	1130	60	1
C 1s	963	60	2
N 1s	849	60	2
O 1s	716	60	2
Cu 2p	315	40	2
Cut-off	5	20	0.1

Table 4.1 Parameters used for real-time spectroscopy of metal surfaces.

4.3. Results

Results on the in-situ processing of metal surfaces are presented in this section.

4.3.1. Clean surfaces

Survey spectrum of copper, aluminium and gold are presented in Figure 4.1 and the principal core-levels presented in Figure 4.2. With the exception of aluminium the surfaces were clean and each core-level fitted with a single component. The aluminium surface was found to contain oxygen and the Al 2s core-level was fitted with two components and the O 1s fitted with a single component, with the fitting parameters given in Table 4.2. The fitting parameters of the sputter-annealed copper surface and sputtered-only copper surface is given in Table 4.3.

Real-time XPS annealing up to 1000 K was performed on the clean copper and gold surfaces and the binding energy change of the Cu $2p_{3/2}$ and Au $4f_{7/2}$ during heating are presented in Figure 4.3. All core-levels exhibited a shift with temperature to lower binding energy which were fully reversible and symmetric with cooling. A linear fit has been calculated for each and the gradient given inset.

Two sputtered-only copper surfaces were investigated with real-time XPS annealing; a 20 minute sputtered surface and a 30 minute sputtered surface. The binding energy change of the Cu $2p_{3/2}$ core-level is presented in Figure 4.4, panel a) showing a 680 K annealing cycle on the 20 minute sputtered surface and panel b) a 980 K annealing cycle on the 30 minute sputtered surface. A linear fit has been calculated for the core-level shift during the regions 300 K to 600 K, 620 K to 680 K, and during cooling from the maximum temperature to 300 K, with the gradients given inset.

Both sputtered-only copper surfaces exhibited a similar binding energy shift of -0.5 meV / 10 K up to 600 K. There was a transition point at 610 ± 10 K where the binding energy rapidly increases, shifting 5.7 meV / 10 K, which was mirrored on both copper surfaces. For the 20 minute sputtered surface a shift of -1.1 meV / 10 K was measured during cooling. For the 30 min sputtered surface a second transition point was measured during heating at 740 ± 20 K where a reversal in the peak shift occurs. The shift continued to lower binding energy above 740 K and did not show any sign of saturating. During cooling to room temperature a shift of -1.3 meV / 10 K was measured.

Core-level / component	**O 1s**	**Al 2s**	
	Al-O	**Al**	**Al-O**
BE (eV)	532.4	118.0	120.5
FWHM (eV)	2.09	2.05	1.88
Lineshape	GL(30)	GL(80)	GL(50)
Ratio	-	1.00	0.30
	1.00	-	0.65

Table 4.2 Fitting parameters for aluminium surface.

Core-level		**Surface**	
		Sputtered	**Sputter-annealed**
Cu $2p_{3/2}$	**BE**	932.55	932.63
	FWHM	1.36	1.34
	Lineshape	GL(89)	GL(92)

Table 4.3 Fitting parameters for sputtered and sputter-annealed copper

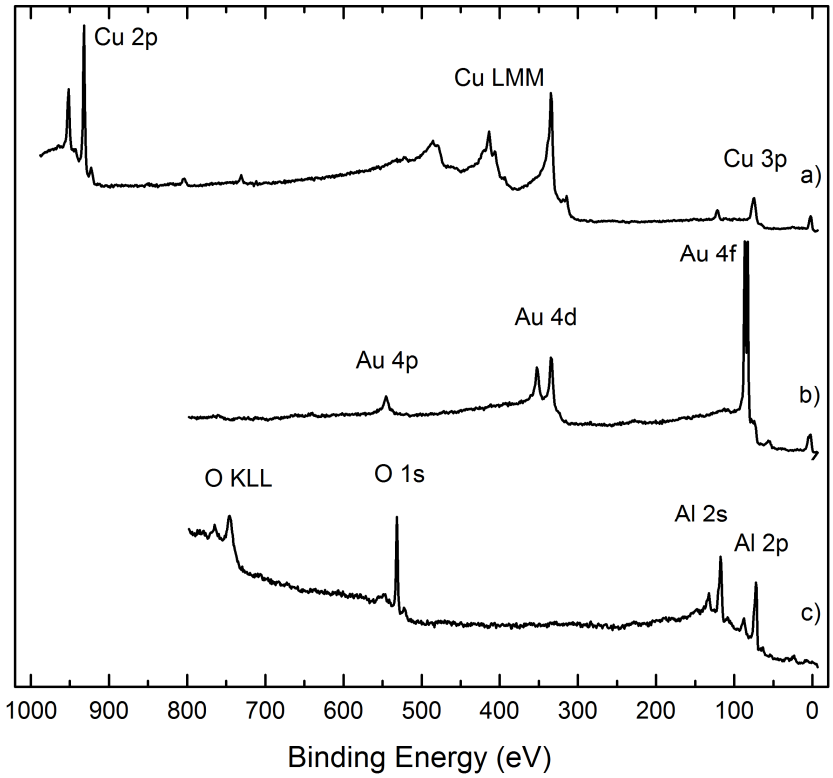

Figure 4.1 Survey spectrum of the metal surfaces; a) Cu, b)Au and c) Al.

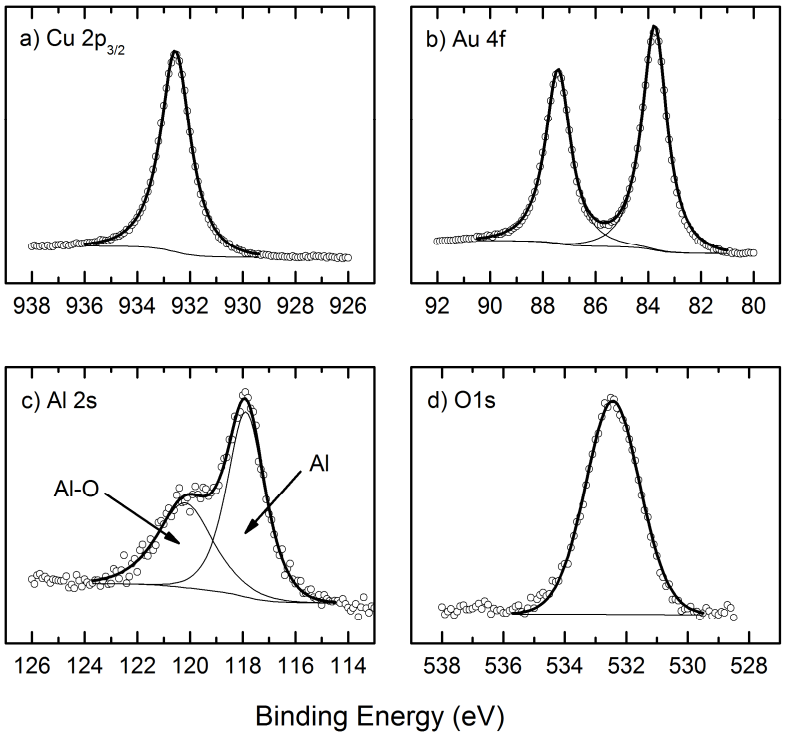

Figure 4.2 Core-level spectrum of the metal surfaces; a) Cu, b) Au, c) Al and d) O 1s (from Al surface).

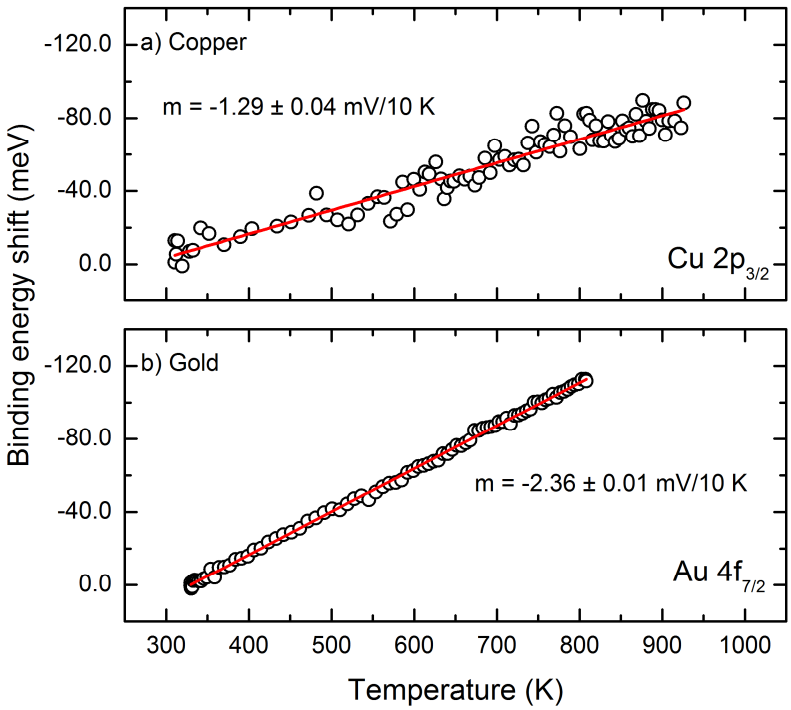

Figure 4.3 Real-time annealing cycles on sputtered-annealed metal surfaces; panel a) Cu and panel b) Au. Heating part of data only shown since shift was symmetrical and reversible.

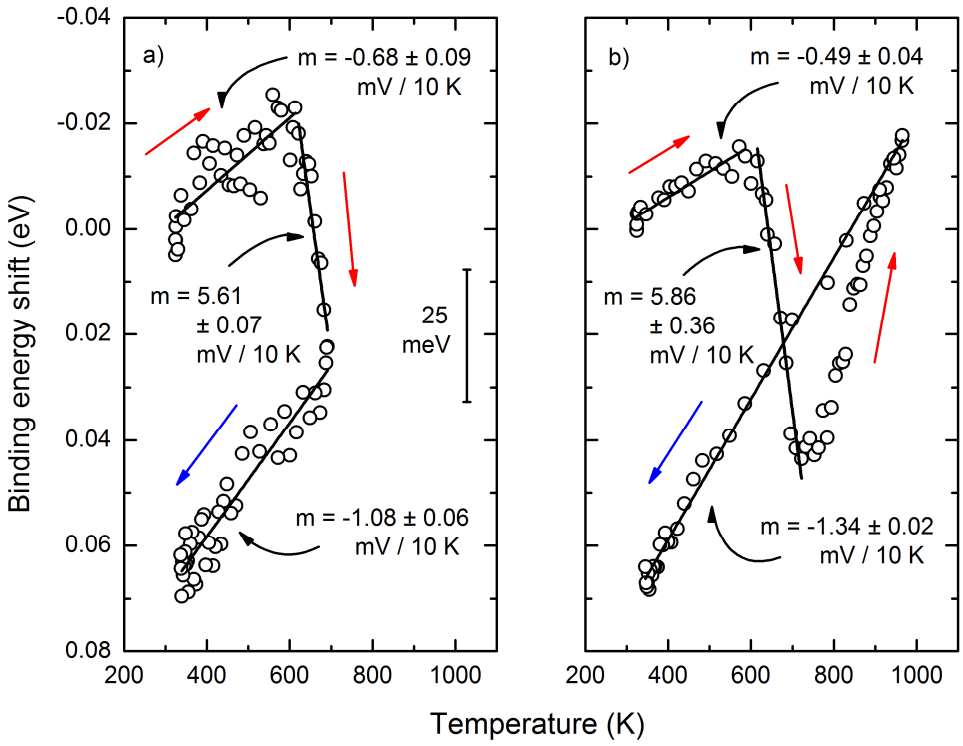

Figure 4.4 Real-time XPS annealing of two sputtered-only Cu surfaces showing binding energy shift with temperature; panel a) 20 min sputtered, 680 K cycle and panel b) 30 minute sputtered, 980 K cycle.

4.3.2. Al/C60 interface

The aluminium surface was exposed to a flux of C60 until spectral features from the aluminium could not be detected and the Al 2s, O 1s, C 1s and secondary electron cut-off were measured in real-time during deposition.

Snapshots of the Al 2s, C 1s and secondary electron cut-off are presented in Figure 4.5, initial snapshots in panels a), b) and c) and final snapshots in panels d), e) and f), along with the fits of the Al 2s and C 1s core-levels. The natural logarithm of the ratio of the intensity to the initial intensity of the Al 2s and the O 1s core-levels are given as a function of time in Figure 4.6. A linear fit was calculated for the attenuation and the gradient is given inset. Electron attenuation lengths are given for Al 2s and O 1s from Evans et al [14]. A contour plot of the normalised secondary electron cut-off snapshots is presented in Figure 4.7 as a function of energy and time, the heavier contour being the normalised intensity 0.25. The binding energy shift of the Al 2s, O 1s and C 1s core-levels as a function of time is presented in Figure 4.8. The shift for the Al 2s and O 1s is given relative to the initial binding energy while the shift for the C 1s is given relative to the final binding energy. The deposition rate of C60 is calculated with reference to the Al 2s and the O 1s core-level to be 0.09 ± 0.02 nm/min :

$$\begin{aligned} r_{al\ 2s} = m_{al\ 2s}\,\lambda &= (0.0007\ s^{-1}) \times 1.81\ nm \\ &= 0.08\ \pm 0.01\ nm/min \\ r_{o\ 1s}\ = m_{o\ 1s}\ \lambda &= (0.0011\ s^{-1}) \times 1.43\ nm \\ &= 0.10\ \pm 0.02\ nm/min \end{aligned}$$

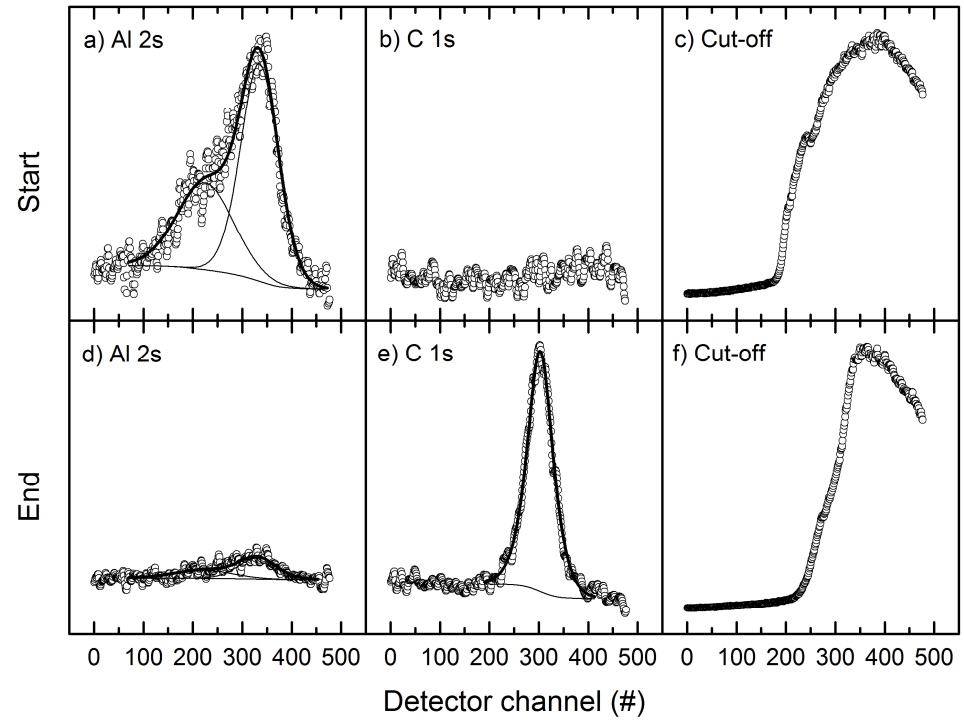

Figure 4.5 Snapshots taken at the start and end of the C60 deposition. Initial and final snapshots; Al 2s panel a) and d), C 1s panel b) and e), cut-off panel c) and f), respectively.

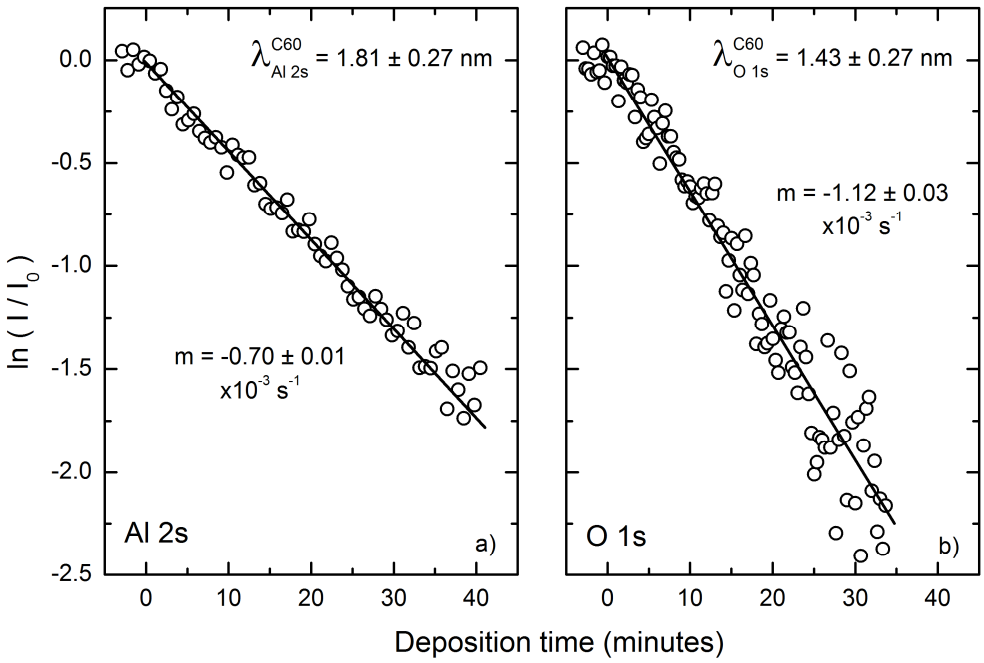

Figure 4.6 Aluminium core-levels during deposition of C60; a) Al 2s and b) O 1s. Linear fit gradient given inset, as is the electron attenuation coefficient.

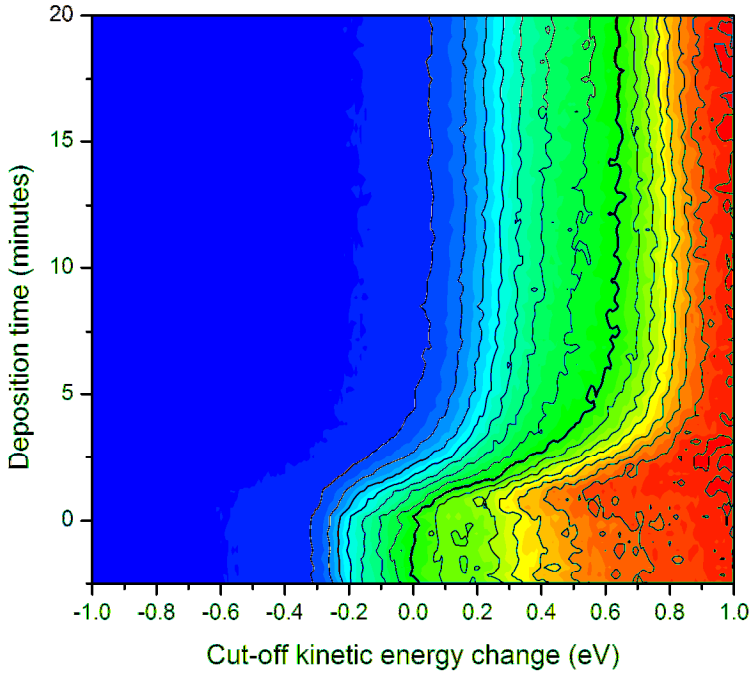

Figure 4.7 Evolution of the secondary electron cut-off during deposition of C60 on aluminium. The heavy contour line indicates 0.25.

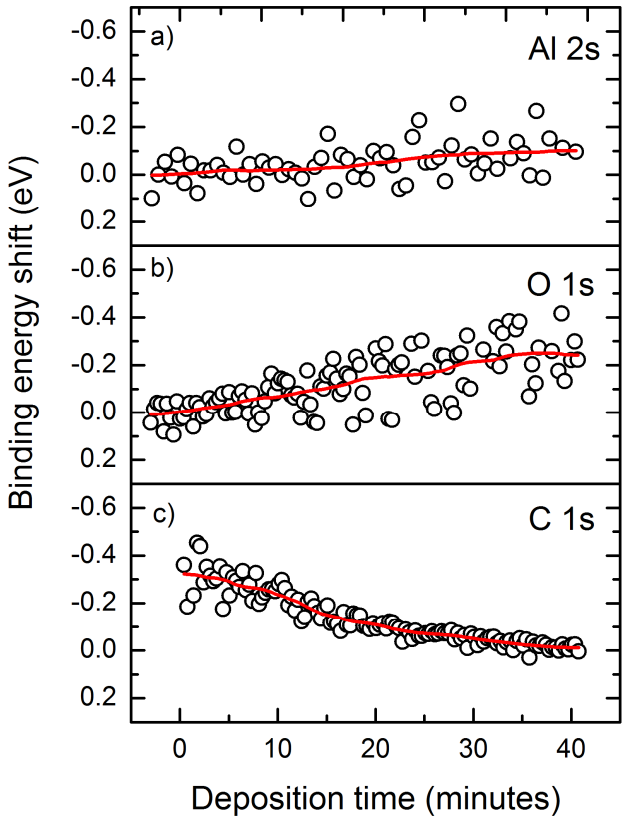

Figure 4.8 Binding energy shift of the core-levels during deposition; substrate panels a) and b), over-layer panel c). Substrate shift relative to the initial energy, overlayer shift relative to the final energy. The red line is a rolling average of the data and serves as a guide.

4.4. Discussion

Copper and gold surfaces free of contamination could be obtained by combination of oxygen plasma, sputtering and annealing. The aluminium film had a surface oxide which had been expected due to the high reactivity of aluminium. From the area ratio of the O 1s core-level to the Al-O component in the Al 2s core-level (1 : 0.65), an Al_2O_3 configuration was determined, confirming the oxygen is not a surface contaminant. The area ratio of the oxide component to the metal component in the Al 2s core-level (1 : 0.3) allows the thickness of the layer to be approximated as being of the order of λ, since the overlayer component (the oxide) is dominant. The electron attenuation length of 1130 eV electrons through Al_2O_3 is 2.3 nm giving a reasonable approximation for the thickness [15].

4.4.1. Real-time XPS annealing

A shift to lower binding energy with temperature was measured for the two metals, each metal exhibiting a different rate of the shift. Of the effects outlined that may cause a shifting of core-levels with temperature the surface photovoltage and sample charging may be discounted as the samples are metallic. The surface chemistry change is discounted as the shifts are reversible and survey spectrum and core-level measurements show the surfaces to be clean. The remaining effect is thermal expansion changing the local potential which manifests as a reduction in the core-level binding energies.

Within the literature comparative results are scarce however a synchrotron radiation study of Al (111) and Al (110) by Theis and Horn [16] measured a shift to lower binding energy with temperature of the Al 2p core-level of 0.5 meV / 10 K. Copper has also been reported to exhibit shifts to lower binding energy with temperature; a synchrotron radiation study of Cu

(111) by Knapp et al [17] found shifts between 1.5 and 2.0 meV / 10 K in the d-bands of copper, and 2.7 meV / 10 K for the surface state. These values are of similar magnitude to those measured in this work and Table 4.4 lists the values measured as shift per Kelvin and shift per percentage expansion, with the two literature values included for comparison.

Within the literature all the investigations of thermal shifts have been single crystals measured with soft x-rays probing shallow core-levels. This work has measured the binding energy shift of two polycrystalline group 11 metals with 1253 eV x-rays probing a deep (Cu 2p) and fairly shallow (Au 4f) core-level. The different shift with percentage expansion for copper and gold suggests a different rate of change of potential for the Cu 2p and Au 4f environments when undergoing thermal expansion. The different electron shell and orbital (848 eV difference in binding energy) may account for this.

Surface	**Thermal expansion (x 10^{-6} K)**	**Core-level**	**Shift meV / 10 K**	**Shift meV / % (dx/x)**
Cu	16.5	$2p_{3/2}$	-1.29 ± 0.04	-79 ± 2
Au	14.2	$4f_{7/2}$	-2.36 ± 0.01	-166 ± 1
Al (111) [16]	23.0	$2p_{3/2}$	-0.57	-37.5
Cu (111) [17]	16.5	5d	-1.5 / -2.0	-91 / -121

Table 4.4 Values for the binding energy shift of copper and gold in terms of temperature and linear thermal expansion. Included is aluminium from [16] and copper from [17].

Narrowing of the order of 0.2 eV was observed in the FWHM of both copper and gold during the real-time XPS annealing. Core-level narrowing with temperature is counter-intuitive as broadening due to electron-phonon interactions would normally be expected. Electron-phonon interactions are observed for single crystals where broadening of the order of 50

meV may occur, however such an effect would be insignificant in a polycrystalline sample as the dominant mechanism is an increase in crystallinity at elevated temperatures. Increasing the crystallinity would result in a reduction to the FWHM, with the lower limit being the phonon-broadened width of a single crystal.

A comparison of sputtered-annealed and sputtered-only copper surfaces (Table 4.3) revealed a 0.1 eV difference in binding energy, a small broadening of the core-level and a slight lineshape change. Such binding energy changes are normally ignored in XPS as changes of this magnitude are commonplace after moving samples between chambers and when setting analyser voltages (0.1 eV is 0.03 % of 321 eV, the kinetic energy of Cu $2p_{3/2}$ core-level). Due to the experimental setup of real-time XPS annealing, where the sample position is not changed and the analyser is set to measure a single core-level, there is a greater reliability in the energy scale and changes to the binding energy within the fitting uncertainty (estimated to be 25 meV) are measurable.

The shift of the Cu $2p_{3/2}$ core-level on the two sputtered-only surfaces was unexpected. Both surfaces shifted to lower binding energy but at a much lower rate than the sputter-annealed surfaces. A clear transition point is observed at 610 ± 10 K for both surfaces and an additional transition point at 720 ± 20 K for the 30 minute sputtered surface. The nature of the first transition point is hypothesised to be the start of the removal of implanted argon and sputter-induced damage. The identical behaviour of both cycles up to 680 K and the similarity of the surfaces after annealing supports this hypothesis. The second transition point is considered to be the temperature where the removal of sputter-induced damage was completed for the second surface. The fact that this is at a higher temperature than the other surface is easily explained by the fact that the surface had been sputtered for 30

minutes rather than 20 minutes, which would induce more damage. It is proposed that within the experimental uncertainty that the second surface during heating above 800 K had the same rate of shifting as that during the cooling. This leaves a region between 720 K and 800 K where a rapid change to the binding energy occurred. This gives a common rate of shifting of -1.2 ± 0.1 meV / 10 K for all copper surfaces that have been annealed above a critical temperature of 610 ± 10 K, with the annealing time dependent on the amount of sputter-induced damage.

The nature of the sputter-induced damage requires addressing. Workers have reported since the earliest days of surface science that a diffraction pattern from a single crystal may only be obtained after sputtering away surface contaminants followed by annealing. Given that the contaminants were removed by the sputtering, annealing was thought to promote atoms back into their crystalline position after being dislodged by the sputtering ions. Since a clean polycrystalline sample does not exhibit a clear diffraction pattern a conceptual similarity between a sputtered single crystal and a polycrystalline sample may be made, both being approximately random [18]. In this work clean polycrystalline copper has been found to exhibit a shifting of the Cu $2p_{3/2}$ core-level to lower binding energy, and this shift was similar to the shift of the 5d level of single crystal copper reported in the literature. This suggests that the nature of sputter-induced damage is not a decrease in crystallinity. An implantation of the sputtering ions into the surface would severely disrupt the local potential causing not only a binding energy shift relative to the sputter-annealed surface, but also a much lower rate of shift with temperature. Although no argon signal was detected in the XPS the presence of below detection limit quantity of argon is likely [18].

The constant gradient of the Cu $2p_{3/2}$ core-level shift up to 980 K poses the question what would happen at even higher temperatures? A possible result is that measured by Theis and Horn [16, 19] for aluminium, where the smooth shift to the binding energy was interrupted at 900 K by a sudden increase of 80 meV. This was reasoned to be the point of surface melting of the aluminium which has a literature value of 933.5 K [20]. The literature value for the melting temperature of copper is 1357.8 K [20]. Since the heater system is quoted to achieve 1400 K and the maximum measured thermocouple temperature was 1200 K, real-time XPS annealing of copper to the maximum heater power may be a useful temperature calibration experiment, assuming a similar discontinuity in the core-level binding energy would occur at the melting temperature.

4.4.2. Al/C60 interface

A precise deposition rate was determined for the C60 by monitoring two widely-spaced core-levels from the aluminium substrate by fitting the natural logarithm of the attenuation of the intensity. Due to the different electron attenuation length from the core-levels a different attenuation gradient was observed for each, and this provided two rate values that were the same within the experimental uncertainty. The accuracy of the deposition rate, 0.09 ± 0.02 nm / min, cannot be commented upon since the actual deposition rate is not known. The growth mode of C60 on aluminium is determined to be layer-by-layer since the substrate core-levels attenuate at a constant rate until undetectable. The total C60 coverage is therefore calculated to be 3.6 nm, which corresponds to 2 λ for electrons from the Al 2s core-level. This is consistent with a hint of Al 2s in the snapshot after 40 minutes since the probing depth of XPS is of the order of 3 λ.

During C60 deposition onto aluminium a binding energy shift was observed for the Al 2s, O 1s and C 1s core-levels, the substrate core-levels shifting to lower binding energy and the overlayer core-level shifting to higher binding energy. For the substrate a different shift was measured for the core-levels, the Al 2s shifting -100 meV and the O 1s shifting -200 meV, while the C 1s core-level of the overlayer exhibited a shift of +300 meV. The data suggests that the carbon environment is becoming more positive while the substrate environment is becoming more negative. A charge transfer between the overlayer and the substrate where electrons are transferred from the C60 layer into the oxygen environment of the aluminium is consistent with the results. Since 3 oxygen atoms are bonded to 2 aluminium atoms in the oxide layer a small binding energy shift would be expected to the Al-O component in the Al 2s, while the main Al-Al component would be expected to remain stationary. While it was not possible to discern a different shift for the two chemical components in the Al 2s (Al-Al and Al-O) due to the resolution, the entire Al 2s core-level does appear to shift to lower binding energy. This may be due to small charging occurring in the oxide causing an apparent shift to the Al-Al component. The secondary electron cut-off change is extremely simple; upon exposure of the surface to C60 the a gradual shift of the cut-off to higher kinetic energy is observed, corresponding to an increase in the work function, saturating at +0.65 eV after 7.5 minutes of deposition, corresponding to 0.68 ± 0.15 nm of C60. This shift is identical to that measured by Seo et al [21] for the secondary electron cut-off change for Al / C60 with UPS. The monolayer thickness of C60 is around 1 nm, therefore the change is associated with the deposition of the first monolayer of C60. The saturation coverages for the secondary electron cut-off and the band-bending are different, the cut-off saturating at 0.68 nm of C60 and the band-bending after 1.80 nm of C60.

The vacuum level change of the aluminium / C60 interface is calculated by taking into account the binding energy change of the overlayer (+300 meV) and the kinetic energy change of the secondary electron cut-off (+0.65 eV), giving a vacuum level change of 0.95 eV. Since the work function of C60 is known to be 4.7 eV [22], the work function of the aluminium surface is determined to be 3.75 eV. Clean polycrystalline aluminium deposited in the 10^{-10} mbar pressure range is quoted to have a work function of 4.28 eV, while oxygen contamination is reported to decrease the work function; values of 3.8 eV have been reported for Al_2O_3 [23, 24], therefore the measured value is reasonable. This is in contrast to the group 11 metals, Cu, Ag and Au, where the work function of the oxide is much greater than the clean metal [25].

4.5. Future work

Two group 11 metal surfaces have been measured with real-time XPS annealing, copper and gold, and a logical next surface to investigate would be silver. Platinum is also a ns^1 metal and may also be relevant to the dataset. Since aluminium has been reported in the literature for s-XPS measurements measuring aluminium would also be logical. It has been a tenet of this work that energetically the behaviour of polycrystalline materials should be similar to single crystal materials. The measure of a single crystal sample, preferably copper, would assist in confirming the binding energy shift mechanism. For the nature of the sputter-induced damage further investigations with longer sputtering times or higher sputtering voltages would be logical. The use of a lighter (neon) or heavier (xenon) gas may also be useful, in particular when sputtering a single crystal metal, since a correlation between the ion size and the crystal structure may be made. Calculation of the activation energy for the process may lead to a greater understanding of the process, especially if sputtering conditions are varied.

For the organic interfaces the adaption of the system to couple to a synchrotron light source would be highly beneficial; real-time s-XPS OMBD would be extremely powerful due to the enhanced resolution and surface sensitivity.

4.6. References

1. Bond, G.C. and D.T. Thompson, *Catalysis by gold.* Catalysis Reviews-Science and Engineering, 1999. **41**(3-4): p. 319-388.
2. Diebold, U., *The surface science of titanium dioxide.* Surface Science Reports, 2003. **48**(5-8): p. 53-229.
3. Campbell, C.T., *Ultrathin metal films and particles on oxide surfaces: Structural, electronic and chemisorptive properties.* Surface Science Reports, 1997. **27**(1-3): p. 1-111.
4. Huttunen-Saarivirta, E., *Microstructure, fabrication and properties of quasicrystalline Al-Cu-Fe alloys: a review.* Journal of Alloys and Compounds, 2004. **363**(1-2): p. 154-178.
5. Ponec, V., *Alloy catalysts: the concepts.* Applied Catalysis a-General, 2001. **222**(1-2): p. 31-45.
6. Hammer, B. and J.K. Nørskov, *Electronic factors determining the reactivity of metal surfaces.* Surface Science, 1995. **343**(3): p. 211-220.
7. Rolls-Royce. *High temperature materials*. 2011; Available from: http://www.rolls-royce.com/technology_innovation/material_tech/high_temperature_materials.jsp.
8. Hamza, A.V., et al., *Reaction and passivation of aluminum with C60.* Surface Science, 1994. **318**(3): p. 368-378.
9. Sun, S.S. and N.S. Sariciftci, eds. *Organic photovoltaics: mechanisms, materials and devices*. 3 ed. 2005, Taylor and Francis: London, UK.
10. Tang, C.W., *Two-layer organic photovoltaic cell.* Applied Physics Letters, 1986. **48**(2): p. 184.
11. Xue, J., et al., *4.2% efficient organic photovoltaic cells with low series resistances.* Applied Physics Letters, 2004. **84**(16): p. 3013-3015.
12. Li, N., et al., *Open circuit voltage enhancement due to reduced dark current in small molecule photovoltaic cells.* Applied Physics Letters, 2009. **94**(2): p. 023307-3.
13. Woodruff, D.P. and T.A. Delchar, *Modern techniques of surface science*. 2 ed. 1999, Cambridge, UK: Cambridge University Press.
14. Evans, D.A. and et al., *CuPc on InSb(111)A—interface bonding, growth mode and energy band alignment.* Journal of Physics: Condensed Matter, 2003. **15**(38): p. S2729.
15. Zemek, J., et al., *Photoelectron escape depth.* Journal of Electron Spectroscopy and Related Phenomena, 1995. **76**: p. 443-447.
16. Theis, W. and K. Horn, *Temperature-dependent line broadening in core-level photoemission spectra from aluminum.* Physical Review B, 1993. **47**(23): p. 16060.
17. Knapp, J.A., et al., *Temperature dependence of bulk and surface energy bands in copper using angle-resolved photoemission.* Physical Review B, 1979. **19**(6): p. 2844.
18. Woodruff, D.P. and T.A. Delchar, *Sputtering and depth profiling*, in *Modern techniques of surface science*. 1999, Cambridge University Press: Cambridge, UK.
19. Theis, W. and K. Horn, *SURFACE PREMELTING IN AL(110) OBSERVED BY CORE-LEVEL PHOTOEMISSION.* Physical Review B, 1995. **51**(11): p. 7157-7159.
20. Lide, D.R., ed. *CRC Handbook of Chemistry and Physics*. 73rd ed., CRC Press.
21. Seo, J.H., et al., *Energy level alignment between C60 and Al using ultraviolet photoelectron spectroscopy.* Applied Surface Science, 2006. **252**(22): p. 8015-8017.
22. Molodtsova, O.V. and M. Knupfer, *Electronic properties of the organic semiconductor interfaces CuPc/C60 and C60/CuPc.* Journal of Applied Physics, 2006. **99**: p. 053704.
23. Mitchell, E.W.J. and J.W. Mitchell, *The Work Functions of Copper, Silver and Aluminium.* Proceedings of the Royal Society of London. Series A, Mathematical and Physical Sciences, 1951. **210**(1100): p. 70-84.
24. Eastment, R.M. and C.H.B. Mee, *Work function measurements on (100), (110) and (111) surfaces of aluminium.* Journal of Physics F: Metal Physics, 1973. **3**(9): p. 1738.
25. Evans, S., et al., *Ultra-violet and X-ray photoelectron spectroscopy studies of oxygen chemisorption on copper, silver and gold.* Faraday Discussions of the Chemical Society, 1974. **58**: p. 97-105.

5. Diamond

In this section investigations into the surface processing of single crystal diamond is presented. Of interest is the preparation of hydrogen and oxygen terminated surfaces in-situ with a microwave plasma and monitoring their transition to the clean reconstructed surface through high temperature annealing.

5.1. Introduction

Diamond is an allotrope of carbon and therefore part of the group IV elements. Thermodynamically it is less stable than graphite however the activation energy for conversion from diamond to graphite is large resulting in the apparent stability. While graphite is a semi-metal, diamond is a wide band-gap semiconductor, it exhibits extreme mechanical, optical and electronic properties, and is of great interest to material scientists. Of particular interest are the electronic properties compared to other semiconductors, as summarised in Table 5.1.

Property	Si	4H-SiC	GaN	Diamond
Bandgap (eV)	1.1	3.2	3.44	5.47
Breakdown field ($MVcm^{-1}$)	0.3	3	5	10
Electron mobility ($cm^2V^{-1}s^{-1}$)	1450	900	440	4500
Hole mobility ($cm^2V^{-1}s^{-1}$)	480	120	200	3800
Thermal conductivity	1.5	5	1.3	24

Table 5.1 Selected room temperature properties of semiconductor materials suitable for electronic applications. Taken from [1].

Diamond has a crystalline structure, shown in Figure 5.1, similar to that of other group IV elements such as silicon and germanium consisting of tetrahedral sp^3 bonds in a face centred cubic lattice, with a cubic edge length of 3.567 Å [2].

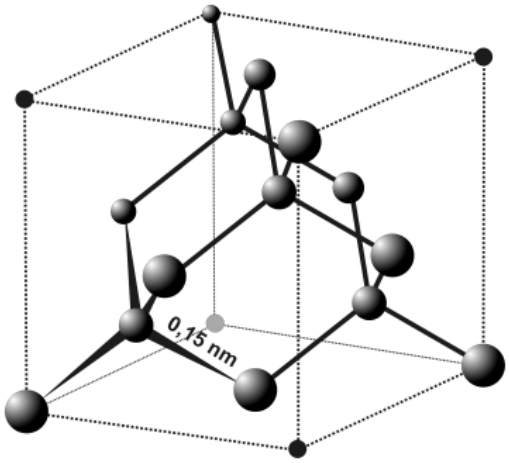

Figure 5.1 Diamond cubic structure. Illustration from [3].

As with all crystalline materials bulk samples may be monocrystalline (single crystal), or polycrystalline (several crystals separated by grain boundaries). The transport properties of single crystals are superior to polycrystalline samples however the chemistry is very similar.

5.1.1. Types

Diamond is formed naturally in the earth where carbon is present at high pressures and temperatures. Natural diamonds contain a variety of impurities, significantly nitrogen, and often have a range of defects resulting in a wide array of characteristics, most strikingly a range of colours from transparent to blue, brown, and pink [4].

Diamond synthesis with high pressures and temperatures was first demonstrated in the 1950's by General Electric where graphite was compressed in the presence of a metallic catalyst forming diamond crystals [5]. Today the process has advanced to produce large

single crystal specimens [6]. Chemical Vapour Deposition (CVD) synthesis of diamond is also possible and was also demonstrated in the 1950's but was not pursued until the 1980's due to the low growth rates [7]. Large single crystal growth is now possible with CVD with a high degree of control over the chemical content [8].

Optical techniques have been used extensively to characterise diamonds and a classification system developed by Robertson et al based on nitrogen concentration is used to classify natural stones [9]. Type I diamonds represent 98% of all natural diamonds and have nitrogen contents up to 2000 ppm, while type II diamonds have a nitrogen content less than 10 ppm. Type I diamond is further divided into several sub-types depending on the form of the nitrogen. Certain type II diamonds were found to exhibit electrical conduction and these were classified as type IIb by Custers [10], non-conducting diamonds assigned as type IIa. The impurity associated with the electrical conduction was later identified as being boron, present up to 1 ppm.

5.1.2. Conduction

For diamond with a bandgap of 5.47 eV and a density of states at the conduction band of $2x10^{19}$ cm^{-3} the calculated intrinsic carrier concentration at room temperature is 1 electron km^{-3} [11]. Such a low carrier concentration has never been observed experimentally due to presence of impurities that act as dopants.

For the purest diamond samples (type IIa or synthetic) there exists some level of nitrogen impurity. Nitrogen is an electron donor for diamond resulting in n-type conductivity with an activation energy of 1.7 eV, however this is a large energy compared to room temperature

(0.026 eV) and consequently the room temperature conductivity is very low. Phosphorus is a known donor for diamond and with an activation energy of 0.52 eV.

Boron is an electron acceptor resulting in p-type conductivity and was identified as the reason why type IIb diamonds are conductive. The activation energy is typically between 0.2 eV and 0.4 eV for boron concentrations of up to 10^{19} cm^{-3}. The conductivity of boron doped diamonds has been measured by several workers and a relationship between the boron concentration and the room temperature conductivity has been observed [12].

5.1.3. Surfaces

At the surface of diamond the bulk structure is interrupted producing an unstable surface with dangling bonds. The surface will therefore terminate by adopting an energetically favourable configuration either through termination of the dangling bonds with an adsorbate or through a surface reconstruction [13, 14]. The number of dangling bonds per surface carbon atom depends on the crystallographic orientation. For the (111) surface there exists one dangling bond per atom while the (100) has two dangling bonds per surface atom [15]. For both the (111) and (100) surface three terminations of diamond are commonly encountered; hydrogen terminated, oxygen terminated and the reconstructed surface, each of which will be discussed in detail.

Producing smooth diamond surfaces is not trivial due to the extreme hardness and chemical inertness. A review of polishing methods may be found by Malshe et al which includes mechanical, thermo-chemical, reactive ion, laser and abrasive liquid jet methods [16]. Mechanical polishing, a traditional method developed by jewellers, involves removal of surface material by abrasive particles, and typically the diamond would be pressed onto a

rotating cast iron wheel with a mixture of diamond grit and oil as a binder. Removal rates are slow with typical values of the order of 10 nm / h [16] due to the large activation energies required for the detachments of carbon atoms. The activation energies are also dependent on the crystallographic orientation and 730 kJ / mol and 1060 kJ / mol has been measured for the (110) and (111) surfaces respectively [17]. For the final surface finish fine diamond grit of < 1 μm would be used.

Hydrogen

Hydrogen chemisorbs to a single dangling bond with a bond strength of 415 kJ / mol, greater than the C-C bond, 344 kJ / mol [13]. For the (111) surface the termination is monohydride (C-H) with a 1x1 surface structure, while the (001) surface may be terminated by monohydride (H-C) in a 1x1 surface structure or dihydride (H-C-H) in a 2x1 surface structure [15].

Hydrogen terminated surfaces exhibit a remarkable property, that of negative electron affinity (NEA). In most circumstances the conduction band minimum (CBM) at the surface lies above the vacuum level and the electron affinity, measured from the CBM to the vacuum level, is termed positive. However for hydrogen terminated diamond the vacuum level lies below the CBM at the surface giving a negative affinity. A consequence of this is that any electron promoted into the conduction band near the surface is above the vacuum level and can leave the sample without any additional energy.

An additional property of hydrogen terminated surfaces is that of p-type surface conductivity when exposed to air. This property was first identified by Landstrass and Ravi who noted a substantial decrease in the conductivity when as-prepared diamond films were

mildly annealed [18]. Ristein et al proposed that the effect was due to an interaction between surface water vapour and the hydrogen producing surface acceptors resulting in a highly conductive surface [19]. The effect, surface transfer doping, has been investigated for various materials on diamond including fullerenes [20] and other organic molecules [21].

For preparing hydrogen terminated diamond surfaces two principal methods are reported; mechanical polishing in oil and in-situ exposure to atomic hydrogen [22]. During mechanical polishing the oil acts as a source of hydrocarbons and hydrogen is chemisorbed onto the dangling bonds. The act of polishing (removal of diamond material) is therefore not important and a 'light' polishing procedure may be used as discussed by Lurie and Wilson [23]. In-situ hydrogenation is performed by exposing a clean diamond surface to atomic hydrogen, and as little as 5% of a monolayer of hydrogen is reported to convert the reconstructed (111) surface to a 1x1 structure [15].

Oxygen

Oxygen having two dangling bonds may bond to carbon in a variety of configurations. The basic components are thought be C=O, C-O-C and O-C-O, resulting in complicated chemistry at the oxygen terminated diamond surface [13]. Of the three principal low index faces the (111) surface is unique in having a single dangling bond and this prevents the formation of O-C-O structures. Oxygen desorption from the (111) surface is therefore uniquely in the form of CO, while the (100) and (110) surfaces may desorb CO and CO_2. An illustration of two oxygen structures, ether bonded (C-O-C) and ketone bonded (C=O) on the (100) surface is presented in Figure 5.2, both having a 1x1 surface structure.

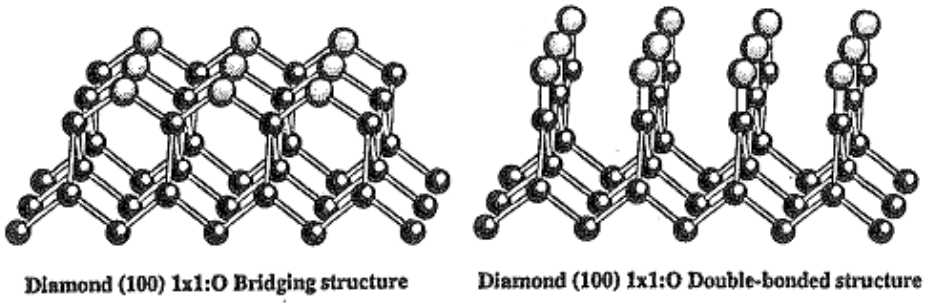

Figure 5.2 Two possible oxygen configurations on (100) diamond. Bridging oxygen, also known as ether structure, and double-bonded, also known as ketone structure. Illustration from [22].

Due to the different chemical environments of the different bonding configurations, chemically shifted components are present in the oxygen core-level, allowing for identification. Wilson et al report for CVD diamond samples +2.75 eV for C=O and +1.4 eV for C-O-C [24], and similar results are reported by many other workers [22]. In contrast to the hydrogen terminated surface oxygen terminated diamond surfaces have a positive electron affinity and do not exhibit p-type surface conductivity. An increased surface conductivity has been reported on smooth oxygen terminated (111) surface but not on the rough surface [25]. The surface conductivity was not observed on the (001) surface [25].

Two principal methods of preparing oxygen terminated diamond surfaces reported are etching with strong oxidizing acids and exposure to atomic oxygen. Acid treatments include nitric acid with potassium nitrate [26] and nitric/sulphuric acid [27]. Atomic oxygen exposure of diamond has been reported by Evans [28] and Klauser [29] where full monolayer oxygen coverages were obtained.

The carbon to oxygen ratio and the atomic concentration of a monolayer of oxygen on the (111) diamond structure as expected in XPS are given in Table 5.2 by following a similar approach to that of Evans and Thomas [28].

Bond configuration	**C : O**	**O (%)**
C=O	18: 1	5
C-O-C	36 : 1	2.5

Table 5.2 Carbon to oxygen molar ratio and oxygen atomic concentrations in XPS for different oxygen bonding configurations on (111) surface diamond.

Since the oxygen bonding environment is detectable using XPS the amount present at the surface may be quantified and the bonding configuration evaluated. For the (111) surface where all dangling bonds are bonded in ketone or ether configuration to oxygen, two chemically shifted components are expected in the O 1s core-level and (5.1) and (5.2) must be satisfied,

$$\mathrm{A}(5\%) + \mathrm{B}(2.5\%) = \text{oxygen } \% \tag{5.1}$$

$$\mathrm{A} + \mathrm{B} = 1 \tag{5.2}$$

where A is the fractional amount of ketone bonded oxygen and B the fractional amount of ether bonded oxygen. For example a full coverage of 5% requires a single oxygen component (A = 1) while a mixed coverage (A = 0.5, B = 0.5) would result in a 3.5% oxygen concentration.

Reconstructed

An adsorbate-free diamond surface can self-terminate to reduce surface energy by forming a dimerized π-electron configuration, known as a reconstructed surface [13]. On the (111) surface the bonds form rows of π-bonded chains, as modelled by Pandey [30], with a doubling of the surface unit cell (2x1 structure). There are only a few reports of an actual 2x1 reconstruction on (111) diamond [31]. What is generally observed is a three domain 2x1 pattern, each domain rotated by 30°, giving the appearance of a 2x2 surface. This is possible due to the equivalence of the three directions on the (111) surface, and such a pattern is labelled as 2x2/2x1 to distinguish from a single domain 2x1 [13, 14]. The quality of the reconstruction may be evaluated with LEED by noting the relative intensity of the second order diffraction spots compared to the first order diffraction spots and the lowest energy the diffraction pattern is observed [32]. The domain size has been associated with the surface roughness and a smooth surface is reported to be a requirement for the reconstruction [33].

Two defining electronic characteristics of the reconstructed surface are a surface state and a chemically shifted component in the C 1s core-level due to the π-electron bonding [22]. On the (111) surface the surface state is observed at around 1 eV below the Fermi level and the chemically shifted component around 1 eV to lower binding energy, while for the (100) surface the surface state is around 2 eV below the Fermi level [34]. A similar surface state is also observed on graphite, however the momentum distribution is quite different [22, 35].

5.1.4. Literature review

A review of relevant published results on hydrogenated and oxygenated surfaces of (111) diamond and their transition to the reconstructed surface through high temperature annealing, focusing on photoelectron spectroscopy results, will now be given.

Hydrogen terminated

Pate performed a series of soft x-ray experiments (hv = 320 eV) aimed at comparing polished diamond surfaces with in-situ hydrogenated diamond surfaces [14]. For the as-polished diamond surface a C 1s core-level composed of a bulk component at 284.3 eV and a small chemically shifted component 1.4 eV to higher binding energy was reported. Following annealing to 1300 K to desorb the hydrogen and produce a reconstructed surface the C 1s peak was found to be shifted to a higher binding energy of 284.8 eV, indicating a 0.5 eV shift in the Fermi level, along with the emergence of a chemically shifted component 0.95 eV to lower binding energy from the bulk peak. The LEED pattern exhibited a change from a 1x1 structure to a 2x1 structure following annealing. Upon re-hydrogenation with an atomic hydrogen source the chemically shifted component was removed, no change occurred to the position of the bulk C 1s peak, and a change in the LEED pattern to a 1x1 pattern. Subsequent annealing at 1300 K caused the re-emergence of the low binding energy component, however the LEED pattern remained 1x1. The removal and emergence of the low binding energy component was fully reversible for re-hydrogenation and 1300 K annealing. Valence band measurements of the re-hydrogenated and 1300 K annealed surface show fully reversible behaviour as well with the emergence of a surface state peak after annealing and the characteristic secondary electron cut-off indicating negative electron affinity. Pate reasons that the re-hydrogenation is not complete but is sufficient to remove

the π-bonded chains and create a NEA but with some surface state density remaining leading to a pinning of the Fermi level. It was also proposed that the hydrogenation prevented the formation of a 2x2/2x1 LEED pattern due to small domain sizes or surface roughening. A similar result where photoelectron spectroscopy results are characteristic of a reconstructed surface but LEED are not was also observed by Küttel et al [33]. Nemanich and van der Weide reported that NEA and the reconstructed surface state of (111) diamond were fully reversible with cycles of hydrogen plasma and argon plasma, the argon plasma removing hydrogen from the surface [36]. However they noted that the 1x1 LEED pattern would remain throughout and estimated from the spectral features that only 15% of the surface had undergone reconstruction. They also compared the position of the Fermi level after plasma treatment and found a reversible increase in band-bending of 0.3 eV with plasma treatment, the reconstructed surface with the higher band-bending. Saby and Muret observed an increased band-bending of 0.9 eV between hydrogen terminated and reconstructed (100) diamond surface, the reconstructed surface with the higher band-bending [37].

Cui et al reported the C 1s core-level width of their in-situ hydrogenated (111) and their reconstructed surface to be similar at 1.1 eV [38], Pate reported 1.2 eV [14], and Evans reported the ex-situ prepared (110) to be 1.2 eV [13].

The group of Ley at Erlangen have investigated the desorption of hydrogen and reconstruction of the (111) diamond surface [38-40]. In a paper by Cui et al [38] a hydrogen terminated surface was prepared in-situ with a microwave plasma and the C 1s core-level of the in-situ hydrogenated diamond surface was reported to be located at 284.8 eV with an electron affinity of -1.27 eV. No changes to the surface characteristics were measured when

annealed up to 850 K. Above this temperature the C 1s core-level binding energy, electron affinity and LEED pattern was found to depend on annealing conditions. A surface annealed at 1000 K for 9000 s (2.5 h) had a C 1s binding energy of 285.0 eV, electron affinity of 0.38 eV and a 2x1 LEED diffraction pattern with second order spots of similar intensity to the first order spots was measured. This reconstructed surface was considered to be a low-temperature phase and was found to be the same as a surface annealed at 1150 K for 10 minutes. For a surface annealed at 1300 K for 10 minutes the C 1s binding energy was observed to saturate at 285.5 eV, the electron affinity saturate at 0.80 eV and the intensity of the second order spots to increase further with an increase to the background. They propose that a partial graphitisation has occurred and that the Fermi level would be semi-metallic and pinned. Graphitisation of diamond is known to occur at temperatures above 1500 K, however graphite has a lower binding energy than diamond (284.3 eV) a distinct C 1s core-level and a 1x1 LEED pattern. Ristein et al report the position of the valence band maximum relative to the Fermi level on the hydrogen terminated surface as measured to be 0.9 eV [41].

Oxygen terminated

Reports in the literature on the oxygen terminated surface of (111) diamond are scarce even today.

Klauser et al in 1996 investigated with synchrotron radiation and LEED the adsorption of oxygen from a microwave discharge onto the reconstructed surface of a type IIa (111) diamond [29]. The clean reconstructed surface was found to have a C 1s core-level with two components, one at 285.0 eV and the other at 284.2 eV, due to sp^3 and π-bonded carbon respectively. Upon exposure to atomic oxygen for 40 minutes at 40 W, 7 x 10^{-5} mbar oxygen,

a third component at high binding energy (286.0 eV) was observed, assigned to C-O. Interestingly the oxygen coverage was estimated to have saturated at 0.5 ML, with further exposure being ineffective in increasing the coverage. LEED measurements revealed the 2x1 structure to be preserved under the half monolayer oxygen coverage, indicating that the oxygen was bonded in a bridging configuration between the Pandey chains in an ether (C-O-C) configuration. Further evidence towards this was obtained from temperature programmed desorption (TPD) studies where only CO was detected.

The work of Kaluser was re-addressed in 2002 by Loh et al with UPS and density functional theory (DFT) calculations of oxygen adsorption [42] onto the reconstructed surface of CVD grown (111) diamond with boron doping.

A 10 minute exposure to oxygen plasma with the diamond at room temperature was found to give 0.45 ML coverage of oxygen. A further exposure of 30 minutes was required to achieve saturation coverage of 0.5 ML of oxygen. The 2x1 LEED pattern retained with saturation coverage, reproducing the results of Klauser. However if the diamond were at an elevated temperature during the oxygen plasma treatment coverage levels attained were higher. At a optimum sample temperature of 670 K a 10 minute exposure to oxygen plasma produced 0.9 ML coverage of oxygen. A complete monolayer was formed after a further 30 minute exposure, with a 1x1 LEED pattern. This was interpreted as of an activation barrier for lifting the 2x1 reconstruction, requiring the diamond to be at an elevated temperature of 670 K during oxygen exposure.

The results were successfully modelled with DFT which showed that the bonding configuration up to 0.5 ML coverage of oxygen with retention of the 2x1 surface was

bridging oxygen (C-O-C) between the Pandey chains. Full oxygen coverage is possible with the removal of the reconstruction with the oxygen in a ketone configuration (C=O).

The Evans group at the University of Wales, Aberystwyth have investigated the interaction of atomic oxygen with the low index faces of single crystal diamond [17, 28, 43-45]. They report that oxygen is present primarily in two forms; ketone bond structure (C=O) and ether bond structure (C-O-C), deduced by component fitting the C 1s and the O 1s core-levels. In one publication [45] they report on the interaction of atomic oxygen with damaged diamond surfaces following argon ion bombardment. They note that the FWHM of the C 1s peak was composed of two distinct components; a bulk component at 285.6 eV (sp^3 bonded carbon) and a surface enhanced component at 284.4 eV (disordered carbon), with a C 1s FWHM of 2.0 eV. Exposure to atomic oxygen resulted in the removal of the component at 284.4 eV, with a narrowing of the C 1s FWHM from 2.0 eV to 1.2 eV proceeding at 0.25 eV / 10 min exposure. Below 1.2 eV the rate of narrowing was much lower with several hours required to achieve a saturated width of 1.0 eV. Oxygen coverages of greater than 1 ML were reported, depending on the atomic oxygen exposure time. The O 1s core-level was measured to be at 531.5 ± 0.4 eV. The valence band maximum of the oxygen terminated (110) diamond was found to be 1.5 eV below the Fermi level [28].

A UPS study by Saby and Muret of a (100) boron-doped CVD diamond having been exposed to oxygen plasma reported the valence band maximum to be 1.0 eV below the Fermi level, while the reconstructed surface following annealing at 1170 K was 1.3 eV below the Fermi level [37].

5.2. Experimental

The diamond was a natural type IIb single crystal, measuring 8.75 mm x 5.05 mm x 1.50 mm, cleaved and polished along the (111) plane, with a doping concentration of $1x10^{15}$ cm^{-3}. The sample has been measured by other workers and publications may be found by Lübbe [46], Langstaff [47], Fyfe [43] and Bushell [48]. The sample was chosen as it is known to produce a reconstructed surface by high temperature annealing with a 2x2/2x1 LEED pattern.

Surface preparation

The diamond must first be prepared ex-situ to remove gross contamination. The surface may then be prepared by ex-situ or in-situ methods. After preparation conventional XPS is performed to evaluate the surface, at which point the surface may be further prepared in-situ (and re-evaluated) or may undergo a real-time annealing cycle. At the completion of the cycle the surface is evaluated. It is then possible to perform a further real-time annealing cycle or to prepare the surface in-situ again.

Initial cleaning was performed by ultrasonic agitation in acetone, 5 min dip in boiling nitric acid, agitation in de-ionized water, and agitation in acetone.

If an ex-situ hydrogen terminated surface was required then mechanical polishing in olive oil was then performed. A Buehler EComet 3 polisher was used, the diamond being pressed with the thumb onto a mixture of 1 μm polishing grit and olive oil on a cast iron wheel rotating at 80 rpm for 5 minutes. A certain orientation and pressure was found to produce the least resistance and this combination was maintained. Following this the diamond was cleaned by agitation in acetone.

A layer of gold was evaporated onto the back of the diamond, estimated to be 10 nm, to produce a good thermal and Ohmic contact with the sample holder, using a Polaron Bio Rad E5200 automatic sputter coater operating for 80 seconds with a current of 15 mA in a pressure of 0.2 mbar. The diamond was then affixed to a pre-annealed sample holder, flushed with acetone, dried with nitrogen gas, and loaded into the vacuum system.

Following loading into the vacuum system ex-situ hydrogenated surfaces were annealed in-situ to 680 K to remove atmospheric contamination. Surfaces that were to be prepared in-situ with microwave plasma were firstly cleaned in-situ, the first step being the removal of adventitious carbon and atmospheric contamination with oxygen plasma exposure for 5 minutes. In-situ annealing up to 1200 K was then performed to produce a clean surface and a fully degassed sample holder. If required further oxygen plasma treatment and 1200 K annealing could be performed until the pressure rise when annealing was minimized ensuring a clean working environment. Following this the required surface termination could be prepared with in-situ microwave plasma.

For in-situ oxygen termination the surface was exposed for 10 minutes. For hydrogen termination a 30 minute exposure was given.

For depositing thin layers of silver a silver Knudsen cell was operated at 60 W power with a thermocouple voltage of 13.2 mV producing a measured rate of 0.34 nm / min. During deposition the pressure was $2x10^{-9}$ mbar.

For real-time spectroscopy the analyser parameters are given in Table 5.3.

Peak / Parameters	C 1s	O 1s
Kinetic Energy (eV)	962	715
Pass Energy (eV)	100	100
Acquisition time (s)	2	4

Table 5.3 Parameters used for the analyser during the real-time annealing

5.3. Results

Results on the in-situ processing of the (111) diamond surface are given in this section.

5.3.1. In-situ hydrogen terminated diamond

The chemical composition of an in-situ hydrogenated surface (that had not recently been mechanically polished) and after annealing at 960 K and 1200 K is given in Table 5.4. C 1s and O 1s core-levels with the LEED patterns of the surfaces inset are presented in Figure 5.4, with the parameters given in Table 5.5. The surface was found to be reproducible with little variation in the fitting parameters. The LEED pattern as-prepared was 1x1 and after 1200 K annealing was 2x2.

An in-situ hydrogenated surface that had been mechanically polished before-hand was measured at 300 K and 800 K and C 1s core-levels are presented in Figure 5.5 right hand panel. The FWHM was slightly less than the surface without mechanical polishing and the C 1s binding energy measured at room temperature was the same as the surface without mechanical polishing. LEED was performed at room temperature, at 700 K, and at room temperature after annealing to 1200 K, and the patterns are presented in Figure 5.5 left hand panel.

Element	Chemical Composition (%)		
	As-prepared	960 K	1200 K
C	97.3	98.1	100
O	2.7	1.9	0

Table 5.4 Chemical composition of in-situ hydrogen terminated diamond surfaces determined from XPS.

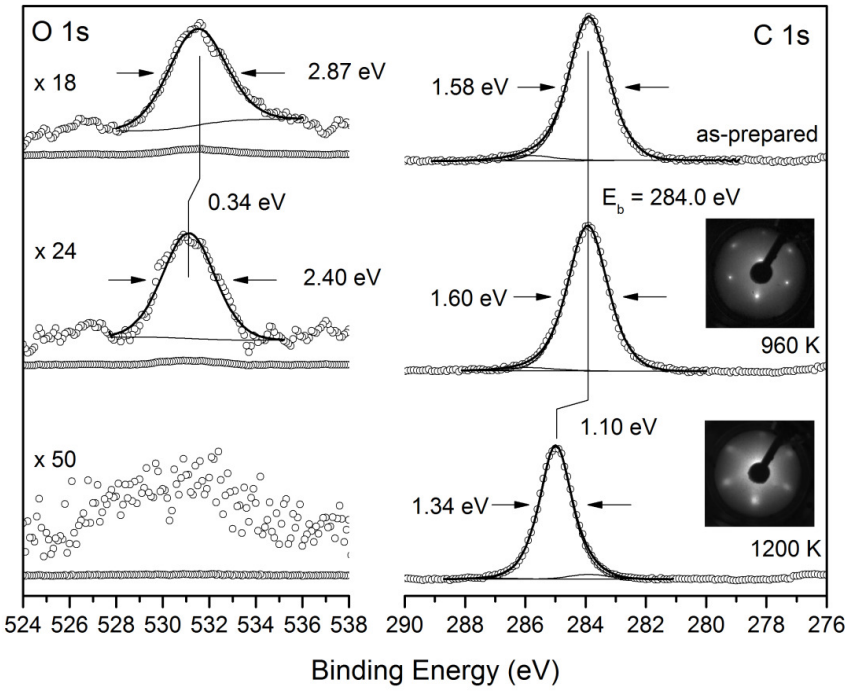

Figure 5.4 O 1s and C 1s core-level peaks for the as-prepared in-situ hydrogenated surface, the 960 K and the 1200 K annealed surfaces. LEED pattern taken at 100 eV for the hydrogen terminated surface and 65 eV for the reconstructed surface.

Core-level / component			Surface		
			As-prepared	960 K	1200 K
C1s	sp^3	BE	284.00	284.03	285.10
		FWHM	1.56	1.56	1.26
		Lineshape	GL(60)	GL(60)	GL(70)
		Ratio	1	1	1
	C-O / C-H	BE	286.00	286.03	-
		FWHM	2.02	2.03	-
		Lineshape	GL(60)	GL(60)	-
		Ratio	0.05	0.03	-
	π	BE	-	-	284.00
		FWHM	-	-	1.29
		Lineshape	-	-	GL(30)
		Ratio	-	-	0.04
O1s		BE	531.59	531.25	-
		FWHM	2.87	2.40	-
		Lineshape	GL(30)	GL(30)	-

Table 5.5 Fitting parameters for the C 1s and O 1s core-levels of the in-situ hydrogenated surface.

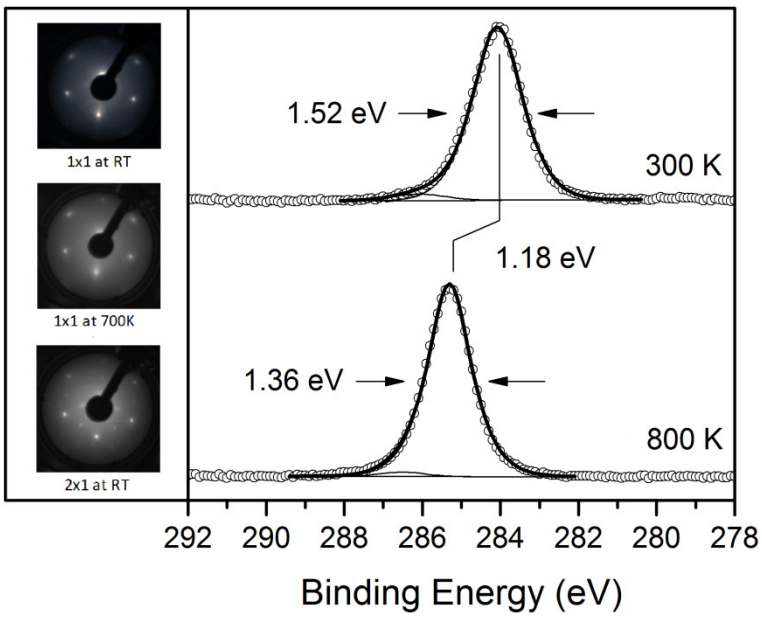

Figure 5.5 Left hand panel are LEED measurements taken of hydrogenated surface at room temperature, at 700 K, and after 1200 K annealing and cooling to room temperature. All measurements taken at 100 eV. No evidence of reconstruction is observed by performing LEED at 700 K. Right hand panel are C 1s core-levels of in-situ hydrogenated surface at 300 K and 800 K.

Several real-time XPS annealing cycles were performed in succession on a freshly prepared in-situ hydrogenated diamond surface. The results of two cycles are included here; 960 K and 1200 K cycle.

First annealing cycle (960 K)

The inset in Figure 5.6 shows the series of C 1s snapshots collected during the cycle, with the peak visibly shifting reversibly to higher binding energy and back to the starting position. The main figure shows the binding energy of the C 1s core-level and the sample temperature as functions of time. Due to the non-linear temperature-time relationship the trend of the C 1s core-level with temperature is difficult to evaluate. To assist in this the binding energy (along with the FWHM and chamber pressure) have been plotted as a function of temperature in Figure 5.7.

The binding energy of the C 1s core-level of the hydrogenated surface shifts with temperature from a room temperature position of 284.0 eV at a rate of 60 meV / 10 K to higher binding energy, saturating at 285.2 eV at 600 K. The core-level maintains this binding energy during heating to 960 K and during cooling to 600 K. Below 600 K a shift to lower binding energy at a similar rate back to the stating value is observed.

The line-width of the core-level changes with temperature, increasing slightly with temperature during the first 50 K, before narrowing at a rate of 9 meV / 10 K up to 600 K. Above 600 K the peak continues to narrow, reaching a minimum of 1.3 eV at the maximum temperature of 960 K. During cooling the peak maintains this value down to 600 K where the peak undergoes rapid broadening at a rate of 32 meV / 10 K, reaching a maximum of width of 1.7 eV at 400 K, and narrowing to the starting value of 1.55 eV with further cooling.

Second annealing cycle (1200 K)

The fitting parameters of the C 1s core-level during the second annealing cycle (1200 K) as a function of temperature is presented in Figure 5.8.

The binding energy of the C 1s core-level with temperature mirrors the first annealing cycle perfectly. Above 960 K the peak position is more variable shifting to higher and lower binding energy by around 0.2 eV. At 1200 K the C 1s was located at 285.1 eV and during cooling shifts slowly to higher binding energy, saturating at 285.2 eV at 600 K.

The line-width follows a similar increase up to 400 K but decreases at a rate of 20 meV / 10 K up to 600 K. Between 600 K and 1200 K the linewidth decreases at a lower rate of 3 meV / 10 K, reaching a value of 1.1 eV. While cooling the line-width increases at a slow rate of 1.5 meV / 10 K, reaching a value of 1.3 eV at room temperature.

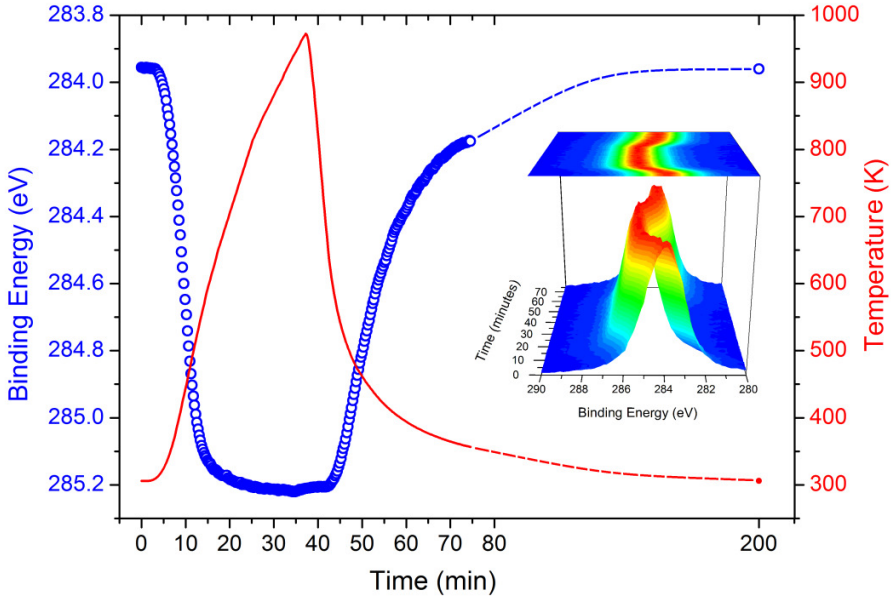

Figure 5.6 Series of C 1s core-level snapshots collected during 960 K annealing cycle on in-situ hydrogenated diamond (111) surface. Open blue circles represent the binding energy of the C 1s core-level as determined by fitting sequentially fitting the snapshots. Red line is the sample temperature during the cycle.

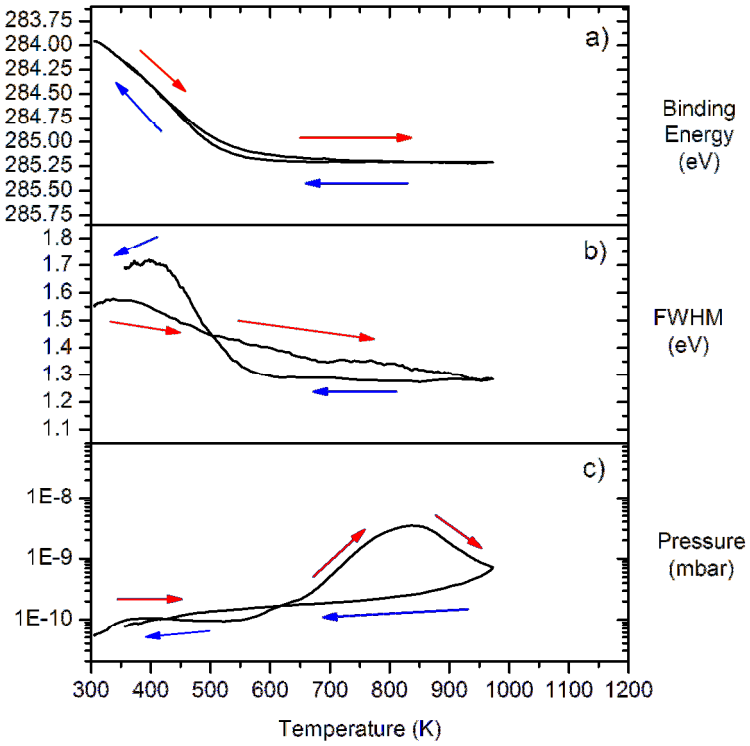

Figure 5.7 C 1s core-level of in-situ prepared (111):H surface during 960 K annealing cycle. Shown is the C 1s a) binding energy, b) FWHM and c) the chamber pressure.

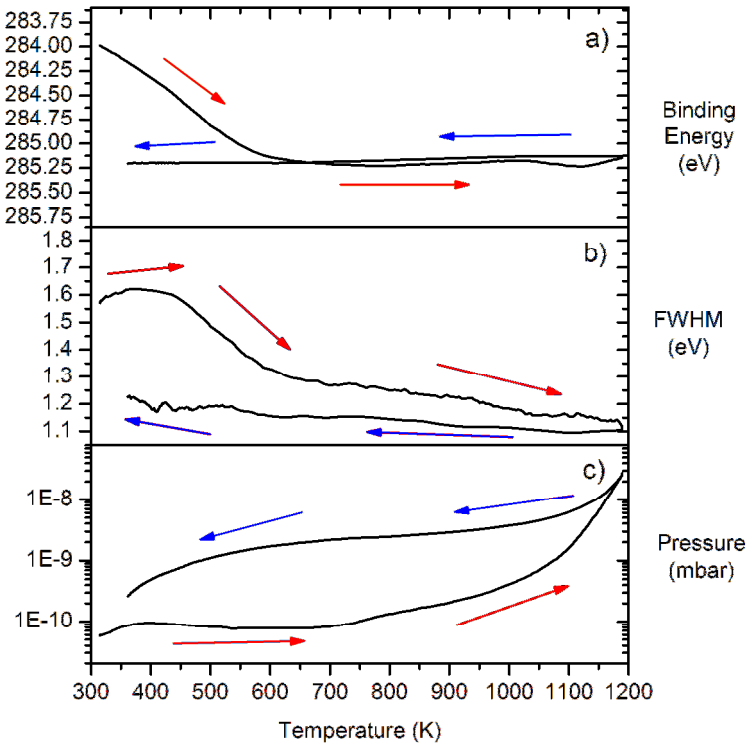

Figure 5.8 C 1s core-level of in-situ prepared (111):H surface during 1200 K annealing cycle. Shown is the C 1s a) binding energy, b) FWHM and c) the chamber pressure.

5.3.2. In-situ oxygen terminated diamond

A survey scan of the as-prepared oxygenated surface is presented in Figure 5.9 revealing no species other than carbon and oxygen being present. The surface had not been recently mechanically polished. The C 1s and O 1s core-levels of the as-prepared surface and after annealing at 680 K and 1200 K are presented in Figure 5.10, the chemical compositions in Table 5.6 and the core-level fitting parameters in Table 5.7. Figure 5.11 shows the total oxygen concentration as a function of annealing temperature. A 1x1 LEED pattern was observed on the oxygen terminated surface with no evidence of second order diffraction spots. After 1200 K annealing a 2x2 LEED pattern was measured.

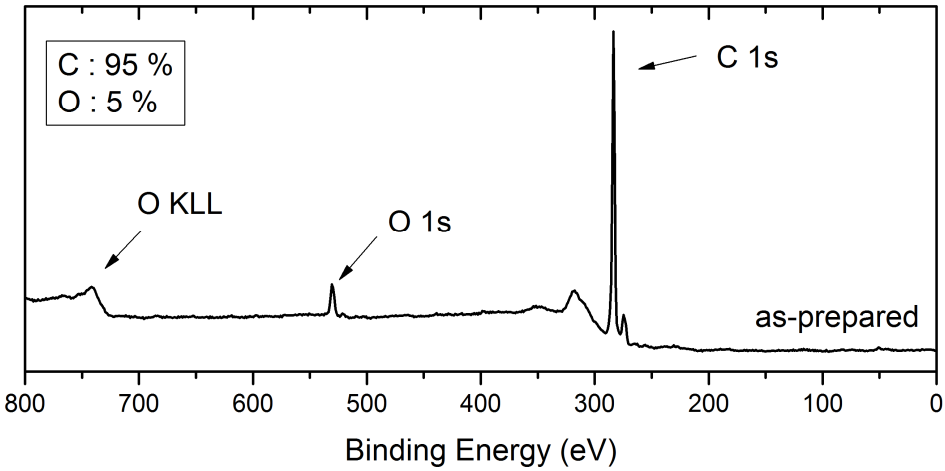

Figure 5.9 Survey scan of the as-prepared in-situ oxygenated diamond surface.

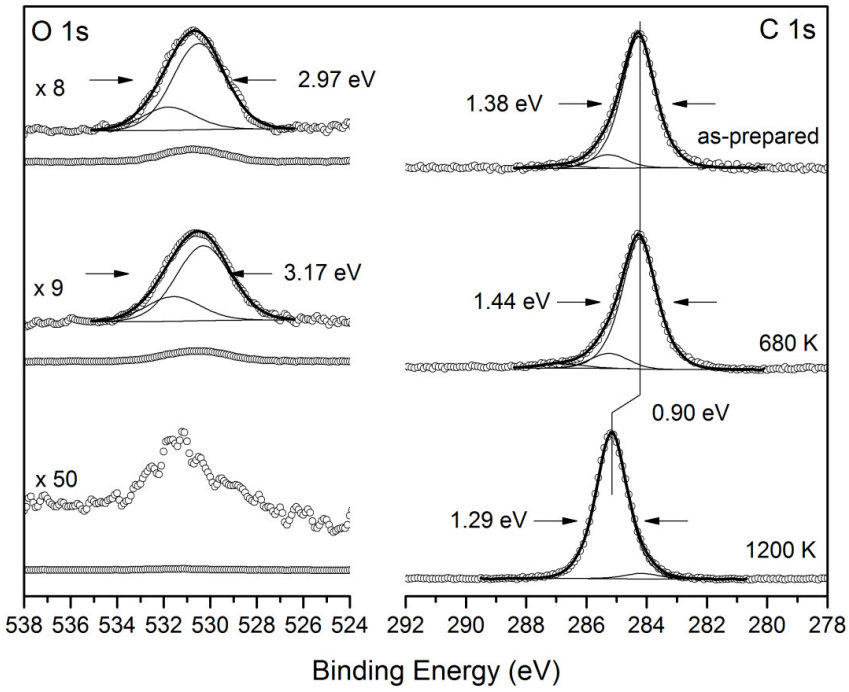

Figure 5.10 C 1s and O 1s core-levels for in-situ oxygenated diamond surfaces.

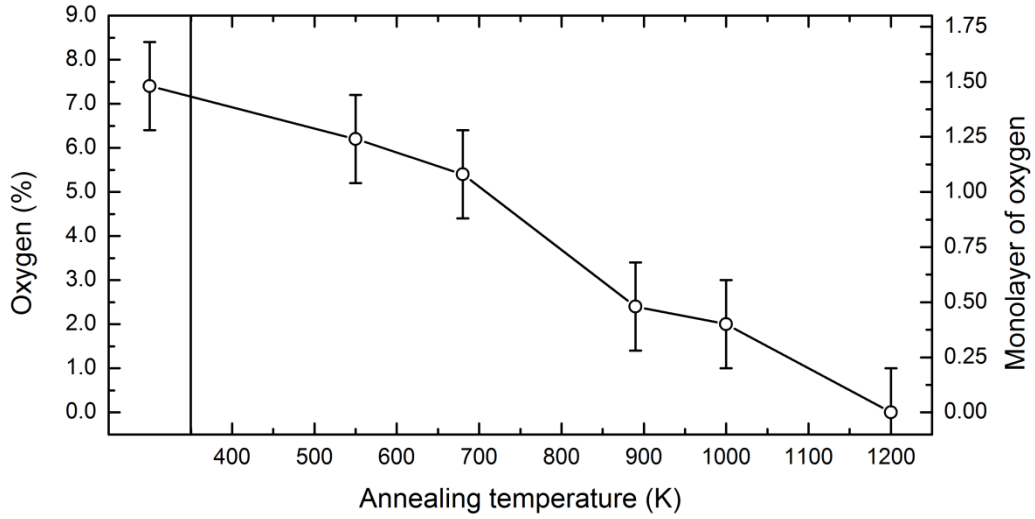

Figure 5.11 Total oxygen concentration of the as-prepared in-situ oxygenated (111) surface and after annealing. Monolayer thickness is calculated for a full saturated ketone bonding configuration.

Element	Chemical Composition (%)		
	As-prepared	680 K	1200 K
C	92.8	93.9	100
O	7.2	5.0	0

Table 5.6 Chemical composition of in-situ oxygen terminated diamond surfaces

Core-level / component			Surface		
			As-prepared	680 K	1200 K
C1s	**sp^3**	BE	284.27	284.35	285.27
		FWHM	1.30	1.34	1.22
		Lineshape	GL(70)	GL(70)	GL(70)
		Ratio	1	1	1
	C-O	BE	285.37	285.35	-
		FWHM	1.42	1.48	-
		Lineshape	GL(30)	GL(30)	-
		Ratio	0.11	0.12	
	C=O	BE	286.87	286.95	-
		FWHM	1.68	1.77	-
		Lineshape	GL(30)	GL(30)	-
		Ratio	0.04	0.04	-
	π	BE	-	-	284.27
		FWHM	-	-	1.34
		Lineshape	-	-	GL(70)
		Ratio	-	-	0.04
O1s	**C-O**	BE	530.59	530.30	-
		FWHM	2.65	2.50	-
		Lineshape	GL(30)	GL(30)	-
		Ratio	1	1	-
	C=O	BE	531.89	531.60	-
		FWHM	2.65	2.50	-
		Lineshape	GL(30)	GL(30)	-
		Ratio	0.27	0.33	-

Table 5.7 Fitting parameters for the C 1s and O 1s core-levels of the in-situ oxygenated diamond surface.

Four real-time annealing cycles were performed in succession on a freshly prepared in-situ oxygenated surface; 680 K, 920 K, 1020 K and 1200 K with conventional XPS spectroscopy performed at the start and finish of each cycle. Figure 5.12 is a composite of the binding energy of the C 1s core-level during each cycle shown in series. The full real-time data for each the 680 K, 920 K, 1020 K and 1200 K are presented in Figures 5.13, 5.14, 5.15 and 5.16 respectively.

The binding energy of the C 1s core-level during the first cycle, 680 K, was found to be fully reversible. During heating the core-level shifted from the room temperature value of 284.3 eV reaching a saturated binding energy of 285.7 eV at 600 K. During cooling the core-level mirrored the heating path and returned to the start position when cooled to room temperature. The rate of shift was not constant being around 18 meV / 10 K at room temperature, reaching a maximum of 67 meV / 10 K at 475 K, decreasing to zero at 600 K.

During the second cycle, 920 K, the C 1s core-level mirrored the previous cycle up to 680 K, with the saturated binding energy of 285.7 eV persisting up to 725 K. Above 725 K the binding energy starts to reverse at a rate of 4 meV / 10 K. This reversal continued up to 920 K reaching a final value of 285.5 eV. During cooling the peak position of 285.5 eV was maintained down to 500 K, before shifting to lower binding energies at a rate of 65 meV / 10 K. However the peak position did not return to the original value, but a binding energy of 284.5 eV, 0.15 eV to higher energy.

The binding energy of the C 1s core-level during the third cycle, 1040 K, shifted from 284.5 eV at a rate of 47 meV / 10 K up to 650 K, where a saturated C 1s binding energy of 285.5 eV was measured. This saturated value was maintained up to 920 K where the peak again started to shift towards lower binding energy at a rate of 4 meV / 10 K. At 1040 K the C 1s

had reached a binding energy of 285.4 eV, which was maintained during cooling down to 500 K. Below 500 K the peak shifted at a rate of 47 meV / 10 K towards a room temperature position of 284.6 eV, offset from the starting value by 0.11 eV to lower binding energy (0.26 eV from the original as-prepared surface).

For the fourth cycle, 1200 K, C 1s core-level was found to shift to higher energy from room temperature at a rate of 35 meV / 10 K, reaching a saturated value of 285.4 eV at 750 K. This value was maintained up to 1040 K, where the peak again started to reverse towards lower binding energy. At 1120 K the rate of shifting increased to 26 meV / 10 K, reaching a binding energy of 285.2 eV at the maximum temperature. During cooling the binding energy was maintained down to 400 K, where the peak started to shift to lower binding energy, reaching a value of 285.0 eV at room temperature.

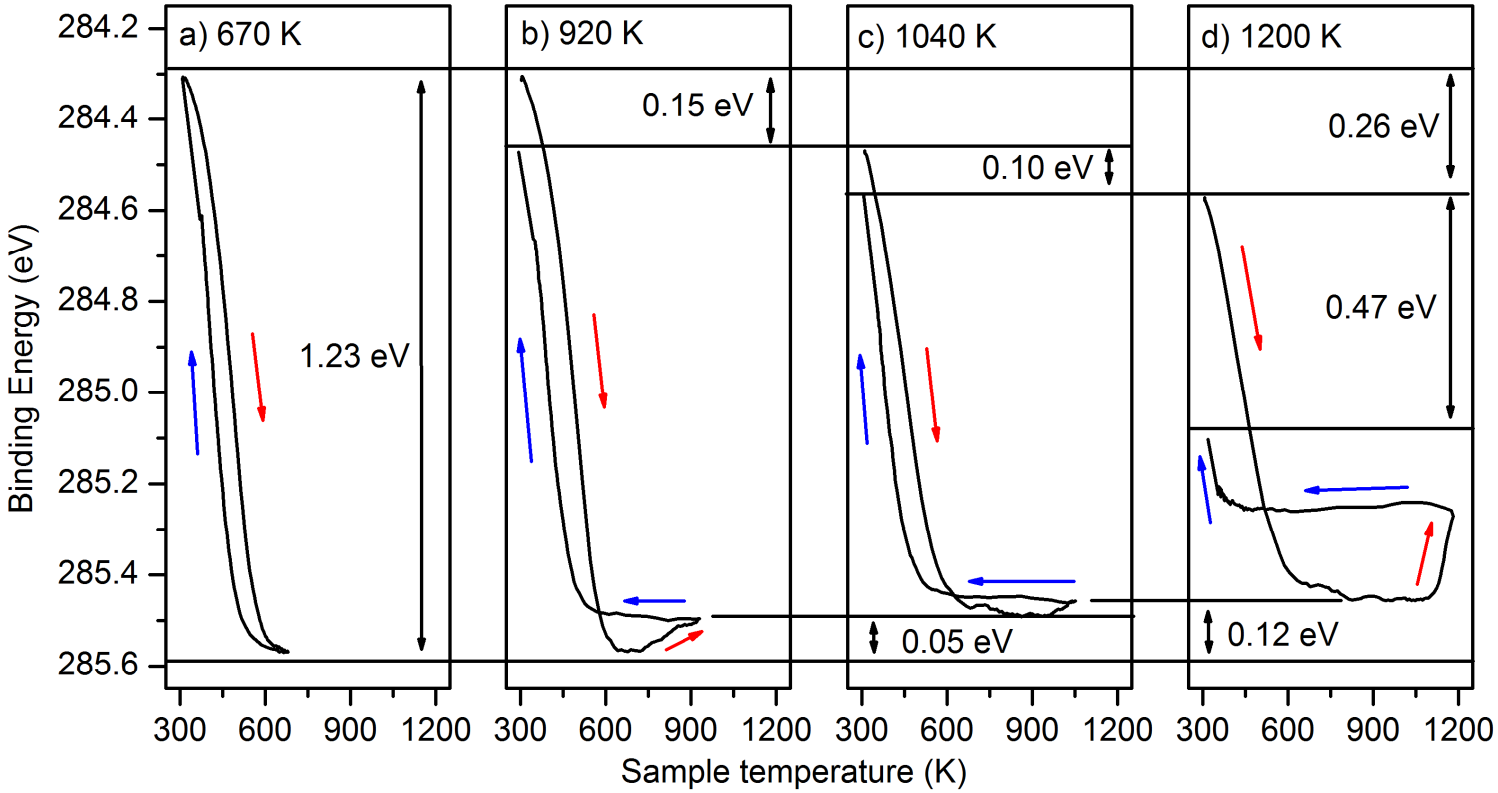

Figure 5.12 Successive annealing cycles on an in-situ oxygen terminated surface with the binding energy of the C 1s core-level as a function of temperature. Cycle a) is fully reversible while the C 1s core-level at the end of cycles b) and c) is to higher binding energy. Cycle d) is desorption of all remaining oxygen and reconstruction.

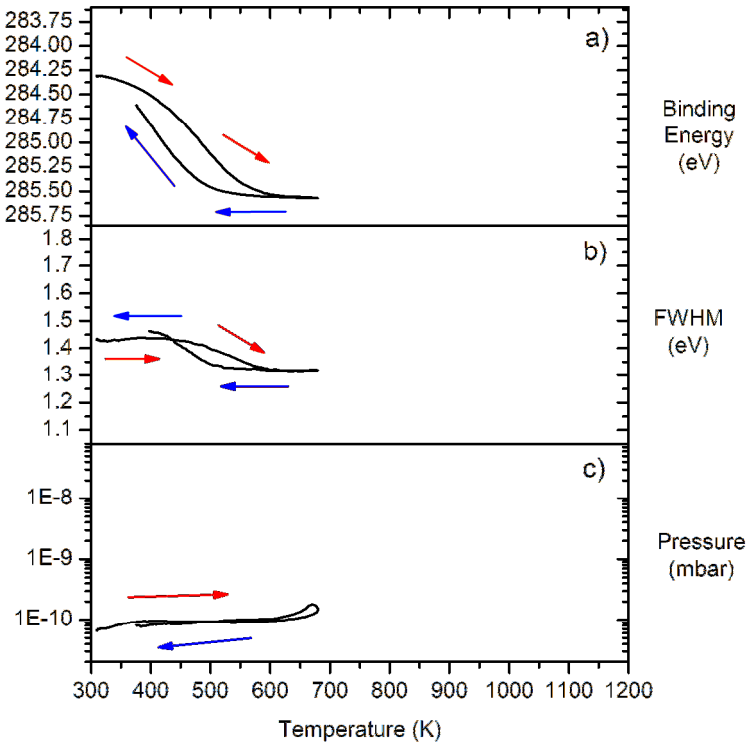

Figure 5.13 C 1s core-level of an in-situ prepared (111):O surface during a 680 K anneal cycle. Shown is the C 1s a) binding energy, b) FWHM and c) the chamber pressure.

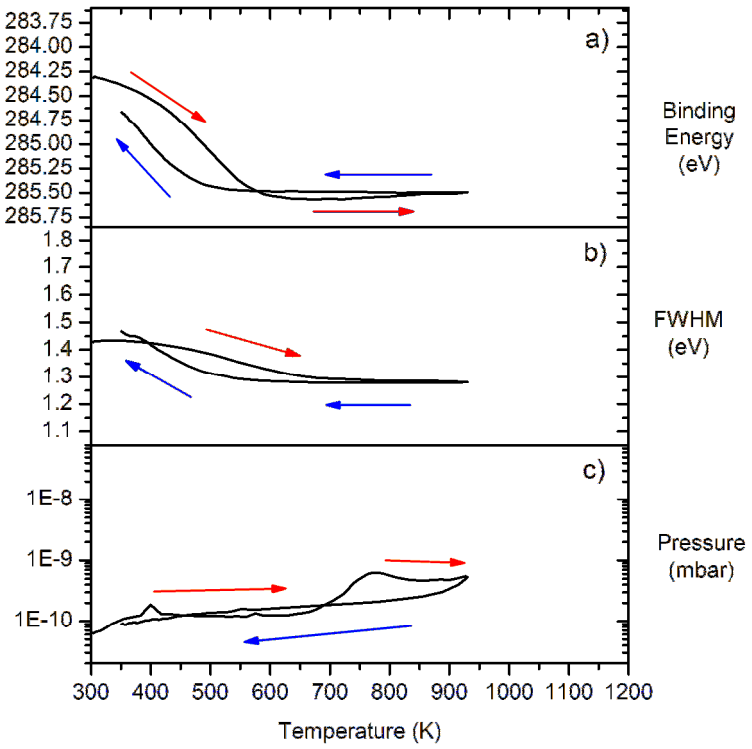

Figure 5.14 C 1s core-level of in-situ prepared, 680 K annealed, (111):O surface during 960 K anneal cycle. Shown is the C 1s a) binding energy, b) FWHM and c) the chamber pressure.

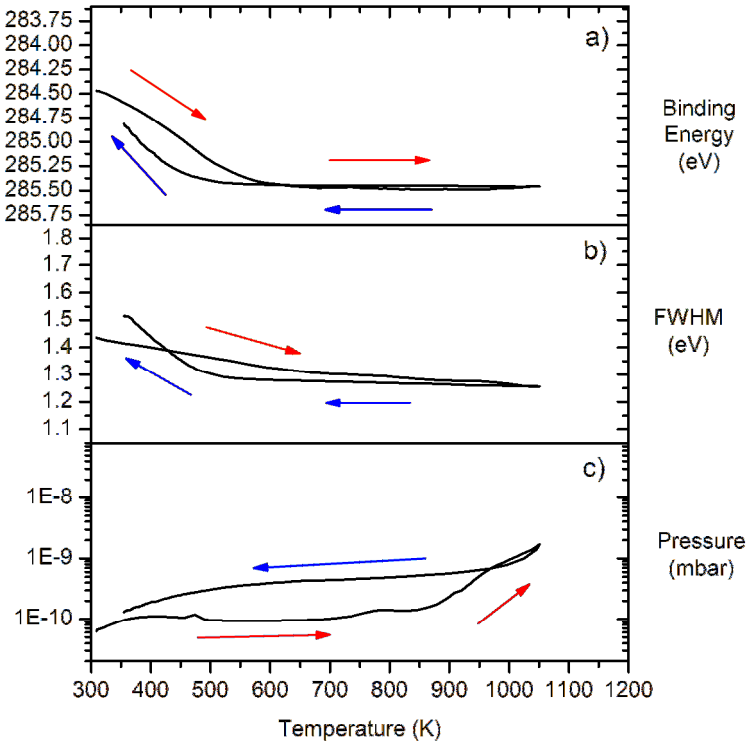

Figure 5.15 C 1s core-level of in-situ prepared, 960 K annealed, (111):O surface during 1040 K anneal cycle. Shown is the C 1s a) binding energy, b) FWHM and c) the chamber pressure.

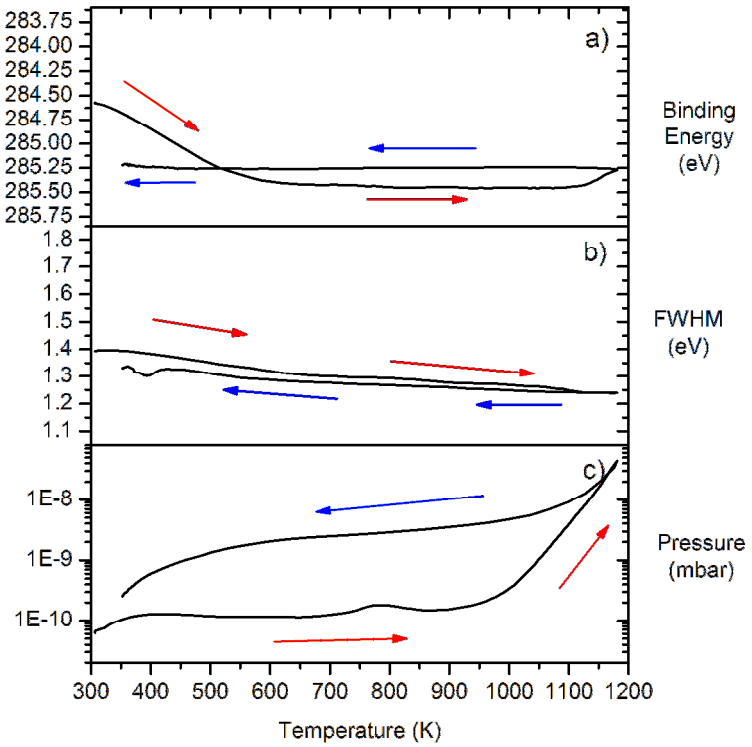

Figure 5.16 C 1s core-level of in-situ prepared, 1040 K annealed, (111):O surface during a 1200 K anneal cycle. Shown is the C 1s a) binding energy, b) FWHM and c) the chamber pressure.

5.3.3. Ex-situ hydrogen terminated

A survey spectrum of the ex-situ hydrogenated surface after annealing at 620 K and 960 K is presented in Figure 5.17. Some oxygen contamination was detected on the 620 K surface however this was removed after annealing at 960 K. C 1s and O 1s core-levels of the 620 K, 960 K and 1200 K annealed surfaces are presented in Figure 5.18, with the fitting parameters in Table 5.8. Clean ex-situ hydrogenated surface and reconstructed surface are also reported in Section 5.3.5, Table 5.10.

Some variations in the C 1s core-level binding energy were measured on different surfaces after 960 K annealing, typically with binding energies in the range of 283.87 eV to 284.29 eV, however the FWHM of the C 1s was constant at 1.36 eV.

The C 1s core-level was measured while grounded (usual configuration) and with different applied bias, from +5 V to -5 V, the results are presented in Figure 5.19. The surface was a 960 K annealed surface and the data was measured in snapshot mode. The core-level was also measured with different x-ray flux values, Table 5.9 gives the measured binding energy against the measured drain current.

Annealing the surface to 1200 K resulted in a large shift in the C 1s core-level position and narrowing in the line-width, with values in the range of 285.1 eV to 285.5 eV and line-widths in the range of 1.17 eV to 1.25 eV. A 2x2 LEED pattern was measured on this annealed surface with the intensity of the second order spots the greatest for the surfaces with higher binding energy, lower width C 1s core-levels. The core-level of the reconstructed surface was also measured with different x-ray flux values and Table 5.8 gives the measured binding energy against the measured drain current.

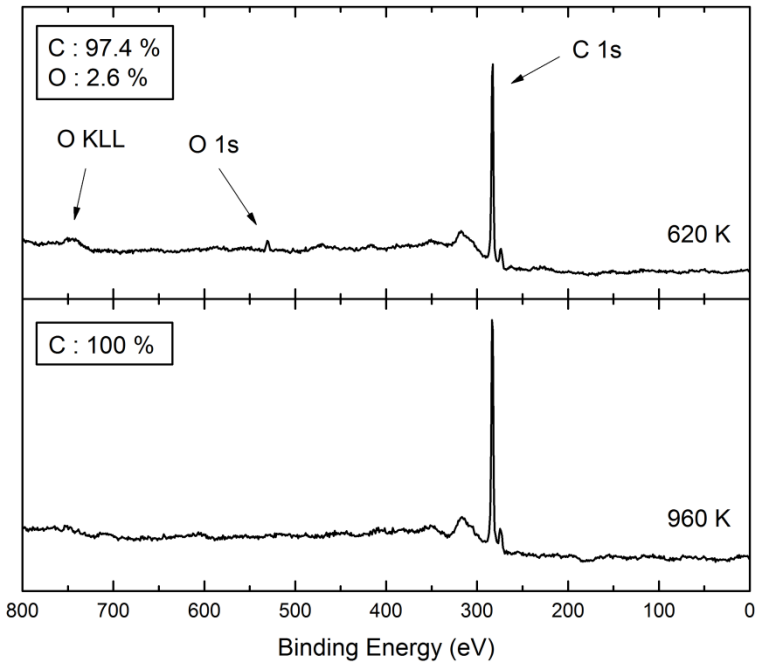

Figure 5.17 Survey spectrum of the ex-situ hydrogenated diamond surface after 600 K and 960 K annealing. All oxygen contamination is removed by the 960 K anneal.

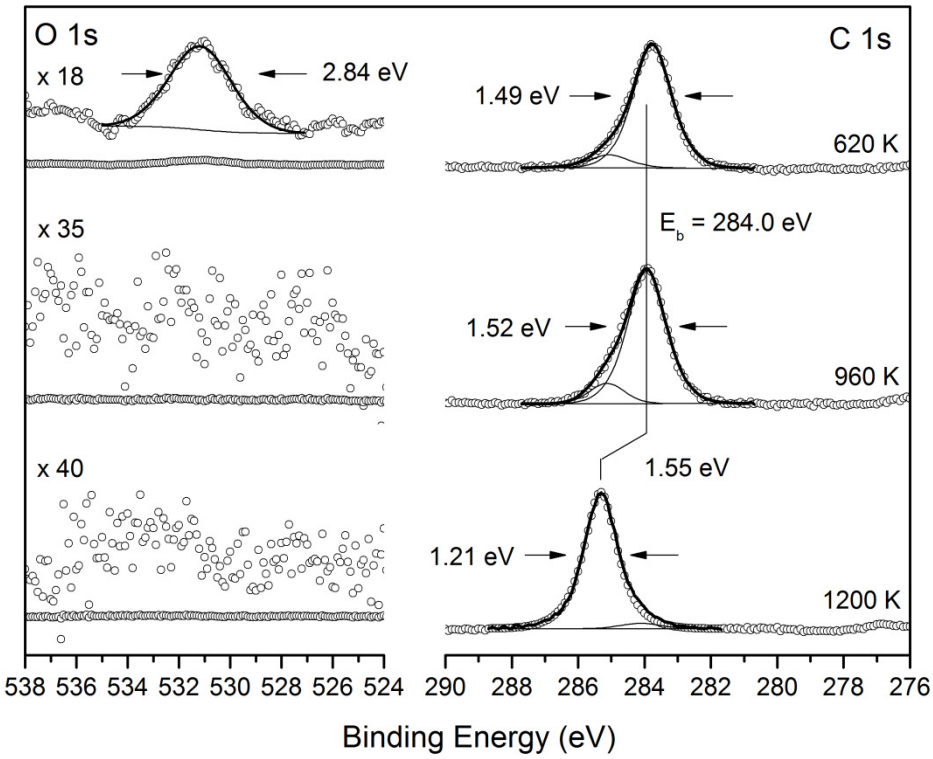

Figure 5.18 C 1s and O 1s core-levels of the ex-situ hydrogenated diamond surface. Spectrum taken after annealing at 620 K, 960 K and 1200 K.

Core-level / component			Surface		
			620 K	960 K	1200 K
C1s	sp^3	BE	283.87	284.03	285.42
		FWHM	1.36	1.36	1.19
		Lineshape	GL(60)	GL(60)	GL(80)
		%	86.28	86.59	95.24
	C-O / C-H	BE	285.05	285.23	-
		FWHM	1.45	1.51	-
		Lineshape	GL(30)	GL(30)	-
		%	11.22	13.41	-
	π	BE	-	-	284.22
		FWHM	-	-	1.42
		Lineshape	-	-	GL(30)
		%	-	-	4.14
O1s	C-O	BE	531.28	-	-
		FWHM	2.84	-	-
		Lineshape	GL(30)	-	-
		%	2.5	-	-

Table 5.8 Fitting parameters for the C 1s and O 1s core-levels of the ex-situ hydrogenated diamond surface.

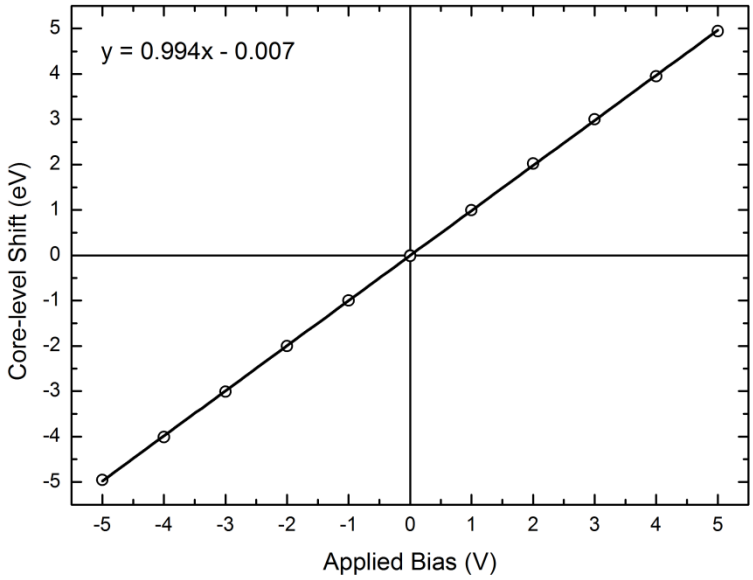

Figure 5.19 Applied sample bias against peak shift for clean ex-situ hydrogenated diamond after annealing at 620 K. The linear fit parameters are included inset.

Drain Current (nA)	C 1s peak position (eV)	
	Hydrogenated	Reconstructed
80	284.34	285.43
14	284.52	285.44
8	284.62	285.43

Table 5.9 Carbon 1s binding energy of the hydrogenated diamond surface with varying x-ray flux.

5.3.4. Reconstructed surface

Real-time XPS annealing was performed on reconstructed surfaces formed after 1200 K annealing of both in-situ and ex-situ prepared hydrogen terminated surfaces and in-situ prepared oxygen terminated surfaces. Two reconstructed surfaces are reported in this section; an in-situ oxygen terminated surface (that had not been recently mechanically polished) that was held at 1200 K for 10 s, and an ex-situ hydrogenated surface that was held at 1200 K for 100 s.

Figure 5.20 shows the binding energy and FWHM of the C 1s core-level of both surfaces as a function of temperature for a 600 K real-time XPS annealing cycle, panel a) for the brief annealing and panel b) for the extended annealing.

The binding energy of the C 1s core-level of the briefly annealed reconstructed surface increased from a room temperature value of 285.0 eV at a rate of 20 meV / 10 K, reaching a saturated value of 285.25 eV at 500 K. The cooling cycle mirrored the heating cycle. The width of the C 1s core-level decreased during heating from 1.50 eV to 1.25 eV and mirrored this behaviour during cooling.

For the extendedly annealed surface the binding energy of the C 1s core-level did not exhibit any shift during heating, remaining fixed at 285.3 eV from room temperature up to 580 K and cooling to room temperature. The width of the C 1s core-level also remained fixed during annealing at 1.37 eV.

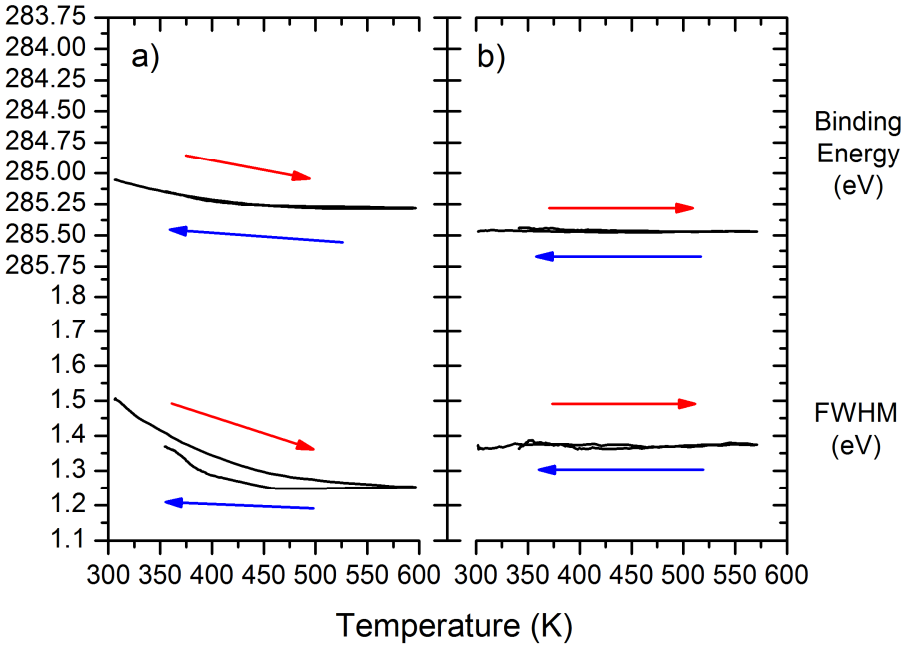

Figure 5.20 Binding energy and FWHM of the C 1s core-level of two reconstructed (111) surfaces. Panel a) was an in-situ oxygenated surface (without ex-situ mechanical polishing) that was annealed at 1200 K for 10 s (brief annealing). Panel b) was an ex-situ hydrogenated surface that was annealed at 1200 for 100 s (extended annealing).

5.3.5. Silver / diamond interface

Thin silver coverages were evaporated onto the clean hydrogen terminated and reconstructed diamond surfaces. The hydrogenated surface was prepared by mechanical polishing and the reconstructed surface by 1200 K annealing (holding at 1200 K for 100 s) of a mechanically polished surface. The fit parameters for the C 1s core-level of the clean surfaces are given in Table 5.10. The fitted C 1s and Ag $3d_{5/2}$ core-levels with silver coverage are presented in Figure 5.21 for the hydrogenated and Figure 5.22 for the reconstructed surface.

A plot of the natural logarithm of the fractional intensity change of the C 1s core-level of diamond with silver to clean diamond against accumulated silver deposition time is presented in Figure 5.23. Two distinct linear regions are present with a point of inflexion at 146 seconds (2.43 min). By fitting the two linear regions to (2.23) the rate of material deposition may be evaluated.

$$r_1 = m_1\lambda = (0.0054\ s^{-1}) \times 0.98\ nm = 0.32\ nm / min$$
$$r_2 = m_2\lambda = (0.0006\ s^{-1}) \times 0.98\ nm = 0.03\ nm / min$$

Core-level / component			Surface	
			Hydrogenated	Reconstructed
C1s	sp^3	BE	284.03	285.52
		FWHM	1.41	1.17
		Lineshape	GL(60)	GL(88)
		Ratio	1	1
	C-H	BE	285.23	-
		FWHM	1.55	-
		Lineshape	GL(30)	-
		Ratio	0.18	-
	π	BE	-	284.42
		FWHM	-	1.4
		Lineshape	-	GL(88)
		Ratio	-	0.05

Table 5.10 Fitting parameters for clean diamond surfaces

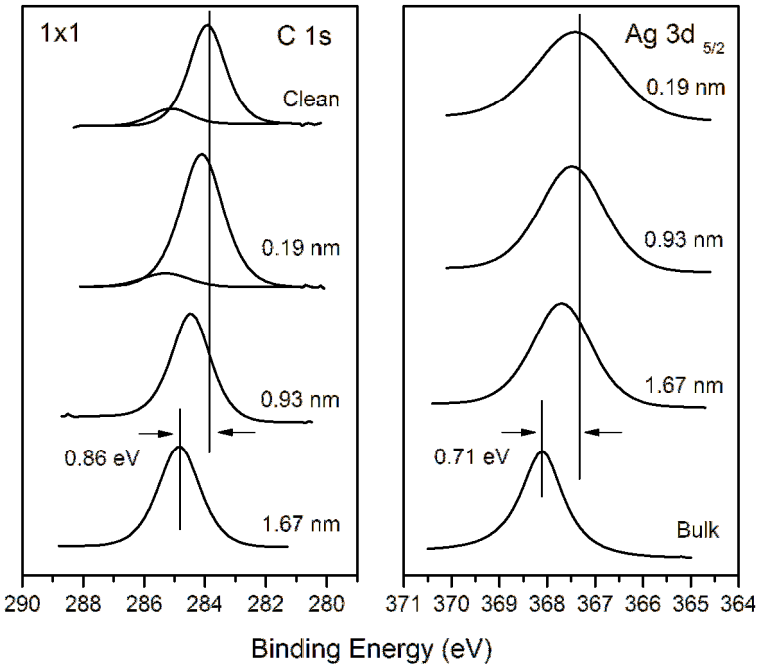

Figure 5.21 Fitted C 1s and Ag $3d_{5/2}$ core-levels data for the diamond hydrogenated / silver interface. Left hand panel shows the C 1s core-levels, right hand panel the Ag $3d_{5/2}$ core-levels, all normalized.

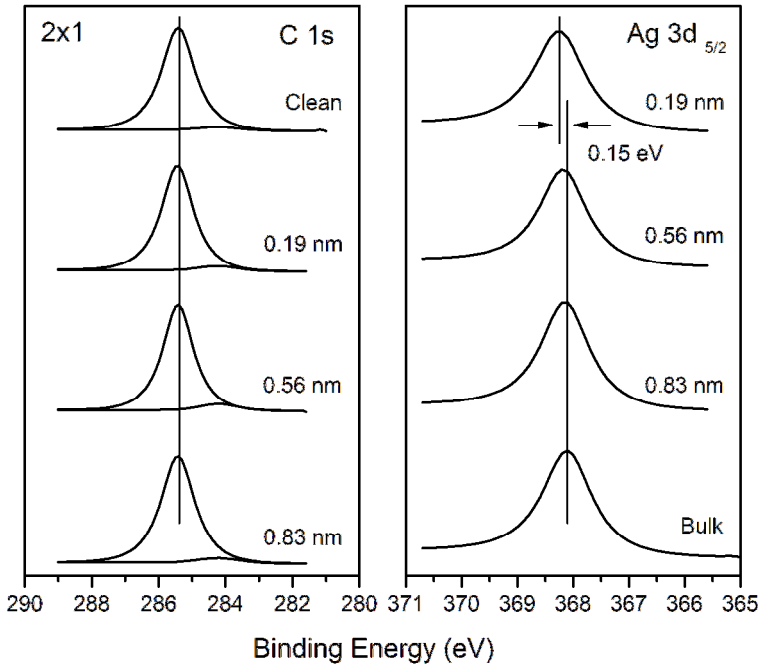

Figure 5.22 Fitted C 1s and Ag $3d_{5/2}$ core-levels data for the diamond reconstructed / silver interface. Left hand panel shows the C 1s core-levels, right hand panel the Ag $3d_{5/2}$ core-levels, all normalized.

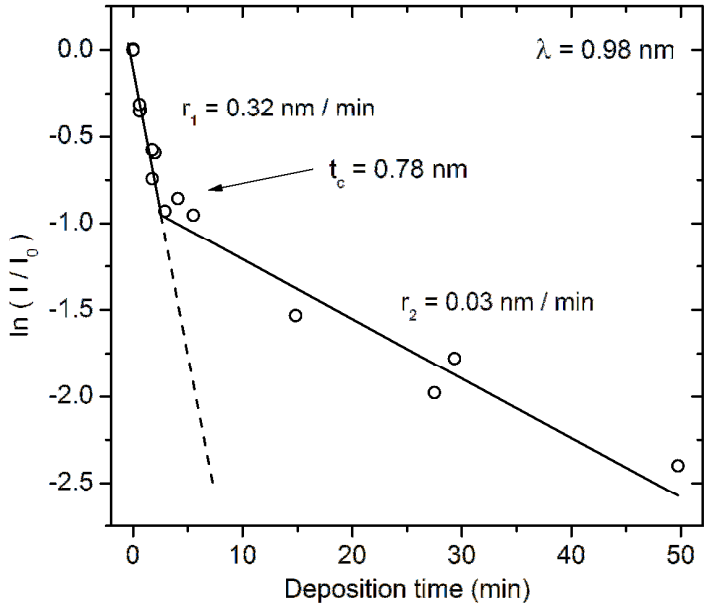

Figure 5.23 Attenuation of the C 1s core-level with silver overlayers. Transition from layer-by-layer growth to island growth occurs at a thickness of 0.78 nm. Data is a composite of three deposition experiments.

5.4. Discussion

Before discussing the individual surfaces it is pertinent to discuss the overall phenomenon of binding energy shifts to higher binding energy for diamond surfaces during real-time XPS annealing.

A perturbation of the bulk Fermi level due to a thermal expansion effect is discounted here as the shift is towards high binding energy rather than low binding energy. The semiconductor band gap is temperature dependent however as the change is a few 10 meV in the temperature range measured this effect may also be discounted.

Changes to the surface chemistry such as removal of hydrogen or oxygen or the creation of π-bonded carbon would result in a change to the band-bending. However these changes would be irreversible and would require the correct temperatures to occur. Evidence discounting the formation of π-bonded carbon at moderate temperatures includes the measurement of LEED at moderate temperatures showing absence of surface structure change (Figure 5.5), allowing chemical change to be discounted.

The room temperature point contact resistance of the diamond was measured to be quite high at 284 kΩ, however the LEED patterns of the reconstructed surfaces were observable at low energy (16 eV) which would not be possible if the sample were too resistive. A significant reduction in the contact resistance may be discounted for several reasons, primarily that the binding energy shift is to towards higher binder energy rather than lower. The preparation of surfaces in-situ was key in eliminating contact resistance effects as it was possible to anneal the samples at high temperature (ensuring correct contact formation, but with desorption of surface species), and to re-prepare the surfaces in-situ with microwave

plasma. A poor contact (non-ohmic) after annealing may be discounted as the C 1s core-level was found to shift symmetrically with applied bias (Figure 5.19), indicative of an Ohmic contact.

The remaining mechanism, that of surface photovoltage, is therefore proposed to be the responsible for the shifting of the C 1s core-level of diamond with temperature. The photovoltage results in a shift of the surface Fermi level towards the bulk Fermi level (flattening of the bands) resulting in erroneously low binding energies being reported. This has serious consequences for the interpretation of diamond photoelectron spectroscopy data as the effect is dependent on the bulk properties (resistivity), surface properties (depletion width and surface conductivity), and the measurement conditions (x-ray flux and sample temperature). The surface photovoltage effect offers a clear explanation on the wide range of values reported by different workers on similar surfaces. The actual Fermi level position of the surfaces may be measured by performing spectroscopy at elevated temperatures (> 600 K) through thermal removal of the photovoltage. In addition to reporting erroneously low binding energies the surface photovoltage results in a significant broadening of the core-levels giving the appearance of a more disordered surface.

The real-time XPS annealing results are very similar to those of Long and Bermudez [49] on gallium nitride. From these investigations an additional mechanism that the standard Hecht model does not incorporate, that of the bulk resistance of the semiconductor, has been identified. This is proposed to be the unknown mechanism mentioned by Long and Bermudez in their work.

Evidence for the surface photovoltage will be presented with reference to real-time XPS annealing of the surfaces, the formation of diamond / silver interfaces and the variable bias

and x-ray flux measurements. A model for the photovoltage effect incorporating the bulk resistance of the diamond will also be given. To complete the discussion the energy band diagrams with corrections for the photovoltage are included.

5.4.2. Clean surfaces

The characterisation of the clean surfaces prepared in this work will be discussed this section. Four surface preparation methods were investigated in this work; in-situ hydrogen plasma, in-situ oxygen plasma, ex-situ mechanical polishing, and in-situ annealing.

The C 1s core-level fits were found to be similar for all surfaces measured and the chemical shifts are reproduced in Table 5.11 with the assignments determined from comparison with literature.

Assignment	Chemical shift (eV)	Surfaces
sp^3-bonded	–	All
C-O	+ 1.1	Oxygen terminated
C-O / C-H	+ 1.2	Ex-situ hydrogenated
	+ 2.0	In-situ hydrogenated
C=O	+ 2.6	Oxygen terminated
π-bonded	– 1.1	Reconstructed

Table 5.11 C 1s component chemical shifts and assignments.

Before discussing the individual surfaces it is pertinent to show the results of real-time XPS annealing of the clean surfaces (heating portion of the annealing cycle only) together in a composite plot, and this is presented in Figure 5.24. The right hand scale shows the position

of the valence band maximum relative to the Fermi level and the barrier height has been determined by referencing to the flat-band binding energy, determined to be 283.84 eV from the real-time annealing data, the diamond-silver interface and the photovoltage model. Further discussion on this value may be found in Section 5.4.4 where the energy band diagrams of the surface are presented. Table 5.12 includes the valence band maximum position relative to the Fermi level and the barrier height for each of the surfaces at room temperature and high temperature.

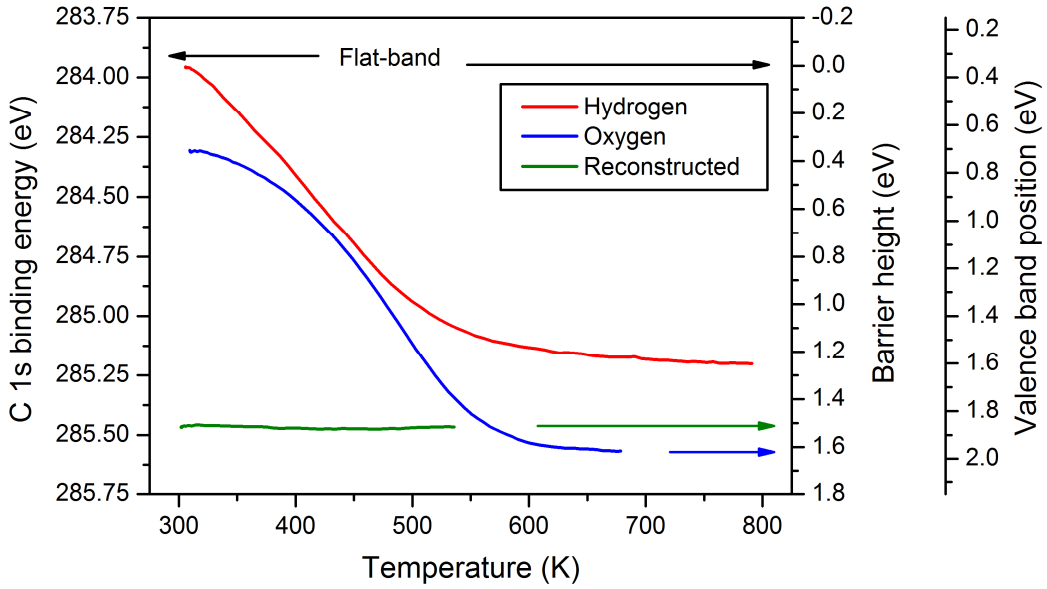

Figure 5.24 Composite plot of the real-time XPS annealing results for the hydrogen terminated, oxygen terminated and reconstructed surfaces of (111) diamond. The curves show the heating part of the annealing cycles. The barrier height and valence band position were calculated by reference to the flat-band binding energy (zero barrier).

Surface termination	$E_F - E_{VBM}$ (eV)		Barrier (eV)	
	RT	HT	RT	HT
H	0.48	1.58	0.16	1.26
2x1	2.00	2.00	1.68	1.68
O	0.75	2.18	0.43	1.86

Table 5.12 Values for the three diamond surfaces at room temperature and at high temperature

Hydrogen terminated surface

A comparison of the survey spectrum of the in-situ prepared surface and the ex-situ prepared surface after annealing at 960 K showed oxygen contamination to have dropped to 1.9% on the in-situ prepared surface but had dropped to zero on the ex-situ prepared surface. This compares favourably with measurements by Pate which showed a small oxygen intensity on ex-situ polished (111) surface after annealing at 800 K [14]. The measurements suggest that oxygen on the in-situ prepared surface was more resistant to removal than on the ex-situ prepared surface. Since the ex-situ preparation method involved mechanical polishing of the surface this would lead to a reduced surface roughness and the removal of defect sites, both of which are known to be associated with increased oxygen uptake [43].

The source of oxygen contamination on the in-situ prepared surfaces is unclear. Surfaces were checked prior to in-situ hydrogen plasma and were found to be clean of oxygen. The operating gas was found to be clean of contamination through residual gas analysis and the primary components of the base vacuum were found to be hydrogen and water. For a base pressure of 1×10^{-8} mbar the monolayer adsorption time is of the order of 100 s and adsorption of oxygen through microwave plasma dissociation of residual water over the 30 min exposure time is therefore possible.

The C 1s core-level on the in-situ and ex-situ prepared surfaces were fitted with two components; sp^3 bonded carbon and a chemically shifted C-O/C-H component to higher binding energy. The chemical shift of the C-O/C-H was different on the two surfaces; 2.0 eV on the in-situ hydrogenated and 1.2 eV on the ex-situ hydrogenated. The different shift may be associated with the surface roughness introducing more chemical environments on the surface of the in-situ hydrogenated. For the in-situ prepared surface the relative intensity of the C-O/C-H component to the sp^3 component (1 : 0.05) suggests it is wholly related to oxygen on that surface, however on the ex-situ prepared surface there is zero oxygen but the relative intensity of the component is larger (1 : 0.08). It is possible that the hydrogen coverage is much larger on the polished surface resulting in the larger relative intensity, or that the line-shape is anomalous. Measurement of thin layers of silver on the ex-situ prepared surface revealed the component to vanish with 0.93 nm coverage, suggesting it is a surface adsorbate (hydrogen) reacting with the silver. This is discussed further in Section 5.4.3.

The in-situ prepared surface had a room temperature as-prepared binding energy of 284.00 eV, while the ex-situ prepared surface had a lower binding energy (283.87 eV) that increased with annealing reaching 284.03 eV after 960 K. Both surfaces therefore have the same valence band maximum position relative to the Fermi level after annealing. A sharp 1x1 LEED pattern was measured on both surfaces, the pattern being sharper with a lower background on the ex-situ prepared surface suggesting a higher quality surface. As mentioned previously a large surface photovoltage has been observed on the hydrogen terminated surface and the actual value of the C 1s core-level was found to be 285.18 eV by measuring the C 1s core-level at 800 K (Figure 5.5), this moves the binding energy from one end of reported values in

the literature to the other. For example Cui et al and Pate report the binding energy to be 284.8 eV [22, 38] and Maier et al report 284.2 eV for an as-prepared film that shifted to 284.8 eV after 720 K annealing [50]. In particular the 284.2 eV result of Maier et al appears to be shifted due to photovoltage, however annealing the surface resulted in the removal, possibly through some surface modification.

The actual shift of the C 1s core-level to higher binding energy was measured with real-time XPS annealing. The data could be easily separated into two regions of interest; below 600 K where a shift of 60 meV / 10 K was observed and above 600 K where the binding energy remained fairly constant. For the 960 K cycles the behaviour was reproduced perfectly implying that no chemical change had occurred. This is consistent with the desorption temperature of hydrogen being around 1000 K and that as little as 5% of a monolayer of hydrogen is sufficient to prevent surface reconstruction. Annealing to 1200 K resulted in a deviation to the shift, but only during the final cooling below 600 K. No significant change was observed at the point of reconstruction, merely a fluctuation in the binding energy which may be noise. Below 600 K the binding energy followed a new path to the room temperature value of the reconstructed surface.

The binding energy shift is similar to that reported by Bushell on the same surface following the ex-situ preparation method, however only the relative values are available for comparison [48]. The real-time Bushell data reveals the C 1s core-level to shift to higher binding, however the temperature-binding energy relationship is not the same. The point of reconstruction appears to be more clearly defined in the Bushell data as a sudden increase in the binding energy. This allowed Bushel to report 923 K as the reconstruction temperature. This temperature is certainly lower than the reconstruction temperature in this work being

that 960 K annealing cycles did not reconstruct the surface. It is also lower than the minimum reported by Cui et al with accurate non-contact temperature measurement [38, 51], suggesting the Bushell temperature readings to be too low.

Close inspection of binding energy of the hydrogen terminated surface around room temperature suggests the shift will continue to lower temperatures. However it should be noted the shift gradient had decreased significantly when approaching room temperature suggesting that the shift was near saturation point. This has been taken into account when assigning the position of flat-bands since this is the saturated low binding energy position of the surface.

Variable x-ray flux measurements were performed on the ex-situ hydrogenated surface and a shift to higher binding energy (+0.28 eV) was measured (Table 5.9), consistent with the reduction of a surface photovoltage through a reduction in the number of e-h pairs produced.

The FWHM of the C 1s core-levels were narrower on the ex-situ prepared surface than the in-situ prepared surface, with a slight broadening occurring after annealing. In general the FWHM values are higher than expected (around 1.5 eV), and this is a consequence of surface photovoltage broadening. The true FWHM is measured at high temperature to be around 1.3 eV, as shown in Figure 5.5, much closer to the expected FWHM for single crystal diamond. Even with photovoltage broadening the lower width indicates a more homogeneous chemical environment on the ex-situ prepared surface, consistent with a higher quality surface.

The narrowing of the FWHM is clearly evident in the real-time XPS annealing. At first this counterintuitive as a thermal broadening of a few 10 meV's would have been expected. The value of the FWHM at high temperature is similar to the FWHM measured with conventional spectroscopy at 800 K (1.36 eV, Figure 5.5) and is closer to the FWHM of the C 1s core-level of the reconstructed surface.

Comparing the binding energy and FWHM of the C 1s core-level of the in-situ prepared hydrogen terminated surface to the ex-situ prepared surface reveals that the in-situ preparation was successful. While it was not possible to detect hydrogen with XPS the similarities of the surfaces and dissimilarity to the oxygen terminated and reconstructed surfaces nevertheless was evident.

Oxygen terminated surface

Three components were necessary to fit the C 1s core-level; sp^3 bonded carbon, ether bonded oxygen (C-O-C) and ketone bonded oxygen (C=O), the ketone group at the higher binding energy. The O 1s core-level was fitted with two components in the same ratio as the components in the C 1s core-level, as required chemically.

The oxygen content of the as-prepared surface (7%) was estimated to be around 1.4 monolayers if a complete monolayer is composed of ketone groups. However from the O 1s core-level the oxygen environment is known to be in a 1 : 0.3 ratio of ether to ketone. Applying (5.1) and (5.2) with A = 0.75 and B = 0.25 the expected oxygen content is calculated to be 3%. Although this is much lower than the measured value, it is consistent with an increased oxygen uptake due to an increased surface area as a result of the rough surface compared to the perfectly flat surface modelled by the equations. For the as-prepared

surface the ratio of the ether group to ketone group was approximately 3 : 1 whilst after annealing at 680 K the ratio dropped to 2 : 1, suggesting preferential desorption of the ether group. The total oxygen concentration was found to decrease linearly with temperature, as shown in Figure 5.11, which mirrors the results of Fyfe on the same surface [43]. However the maximum oxygen concentration measured (7%) is lower than the maximum reported by Fyfe (16%), implying that the oxygen uptake in this work was lower. However this is consistent with the short exposure time (10 minutes while Fyfe exposed for more than one hour). The in-situ microwave plasma is therefore effective in producing oxygen termination of the diamond surface.

The binding energy of the sp^3 component in the C 1s core-level at room temperature (284.3 eV) is higher than that measured on the hydrogen terminated surface indicating a higher position of the Fermi level above the valence band. The binding energy of the O 1s peak (530.6 eV) is lower than that reported by Evans (531.5 eV), however Evans reported the C 1s peak in the same system to be 285.6 eV [28]. As reported earlier it is believed that a photovoltage is present at the surface giving erroneously low binding energies. Figure 5.25 shows the measured value and true value of the C 1s core-level binding energy, the true value being determined by measuring the surface at high temperature with real-time XPS annealing. The true C 1s core-level binding energy of the as-prepared surface is around 285.6 eV, the same as determined by Evans [28]. Subtracting the same photovoltage from the O 1s core-level gives 531.9 eV which is also close to the Evans value.

The presence of more than a monolayer of oxygen at the surface and the different binding energy of the C 1s core-level to the hydrogen terminated and the reconstructed surfaces reveals a successful preparation of an oxygen terminated surface. In contrast to the work of

Klauser [29] and Loh [42] it was not necessary to have the diamond at an elevated temperature, and this is consistent with the results of Fyfe [43].

Interestingly the measured C 1s binding energy was found to increase with successive annealing cycles suggesting a negative correlation between the Fermi level and the surface oxygen content, however after photovoltage correction the true C 1s binding energy is found to have a negative correlation with oxygen content. This result, a correlation between the position of the valence band maximum relative to the Fermi level and the surface oxygen content, is unapparent in the conventional spectroscopy. A linear trend was found where the true binding energy shifts at a rate of 30 ± 6 meV / % oxygen. The shift is small but not insignificant; a shift of 0.2 eV to lower binding energy was observed with a decrease in oxygen concentration from 7% to 2%.

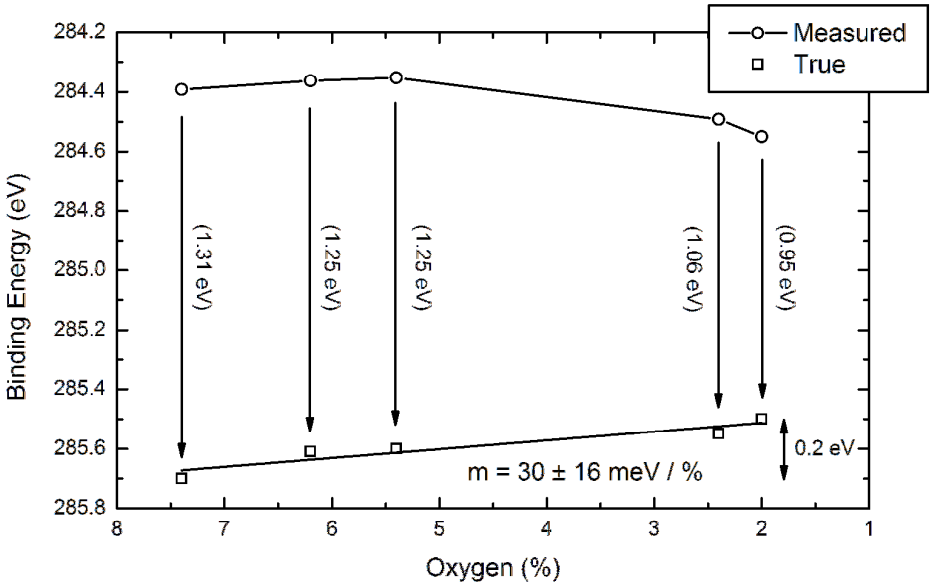

Figure 5.25 Measured and true binding energies of the C 1s core-level of in-situ prepared (111):O surface. The true binding energies were determined by measuring the surface at high temperature. The value of the room temperature photovoltage was then determined by subtraction and is given in parenthesis. The true binding energies have been fitted with a linear curve and the gradient is given inset.

Roberts performed similar measurements on an oxygen terminated (001) diamond and found a similar high-temperature binding energy that was dependent on the oxygen concentration [26]. A photovoltage effect was not identified and the high-temperature binding energy was discussed in terms of an intermediate state at elevated temperature causing Fermi level pinning. This work strongly implies that the effect measured by Roberts is a photovoltage, as in this work, and not a changing density of states at elevated temperatures. A linear trend of 82 ± 13 meV / % oxygen has subsequently been fitted to the Roberts data, and this value is twice that measured for the (111) surface in this work. A significant difference between the (001) and the (111) appears to be the room temperature binding energy of surfaces with different oxygen concentrations. For the (001) Roberts reported that the room temperature value remained constant for oxygen coverages from 8% to 1%, while in this work the room temperature value drifted towards higher binding energy as the oxygen concentration decreased. This would seem to suggest that the value of the photovoltage present on the (001) surface remained constant, while on the (111) surface the photovoltage was seen to decrease with decreasing oxygen coverage. This may be associated with changes to surface conductivity since surface conductivity would result in a low resistance path for dissipating photovoltage. An increased surface conductivity has not been reported on the (001) however for the (111) surface conductivity increases have been reported with decreased oxygen content and may therefore explain the decreased photovoltage [25].

The FWHM of the C 1s core-level was narrower than the hydrogen terminated surface, and the value falls at the lower end of the range quoted by Fyfe (1.32 – 1.56 eV) [43]. Fyfe noted that the width was rather large for a single crystal diamond, especially since oxygen on

diamond surfaces has been noted to reduce the FWHM of the C 1s peak. The width is also higher than that reported by Evans and Riley for a (110) surface with a similar oxygen coverage on a (110) surface (1.15 eV), however the largest FWHM reported for the (110) with minimal oxygen coverage was 1.27 eV. Evidence from the real-time XPS annealing suggests that the core-levels have been broadened by the surface photovoltage and that the true width is in fact lower.

The widths of the O 1s core-levels were larger than expected for a single species (2.6 eV) however without sufficient chemical shift data for oxygen on diamond it is impractical to fit more components (such as hydroxide groups). However it is unlikely that hydroxides are present on the surface after oxygen plasma exposure as efficient conversion to volatile compounds such as H_2O would be expected. It is more likely that the increased width of the oxygen components is due to a combination of photovoltage broadening and a heterogeneous chemical environment as a result of the surface roughness giving rise to more bonding environments.

The binding energy of the first cycle appears to be very nearly saturated at room temperature at (284.3 eV). Since the flat-band binding energy has been determined to be 283.8 eV this suggests that the oxygen terminated (111) surface in this work has a pinning state 0.17 eV below the valence band maximum.

Reconstructed surface

For the reconstructed surfaces all C 1s core-levels required an additional chemically shifted component 1 eV to lower binding energy, characteristic of π-bonded carbon at the surface. No oxygen was detected on any of the reconstructed surfaces either in the form of an O 1s

core-level or a chemically shifted carbon-oxygen component in the C 1s core-level. No evidence of a graphitic surface was detected in the C 1s core-level such as the characteristic plasmon loss structure, π* resonance peak. The 2x2 LEED pattern was consistent with the formation of a three domain 2x1 surface (2x2/2x1).

The binding energies of the sp^3 component in the C 1s core-level of the reconstructed surfaces fell in the range 285.10 eV to 285.52 eV, surprisingly in perfect agreement with that reported by Cui et al for (111) reconstructed surfaces [38]. The FWHM was narrower than on the hydrogen and oxygen terminated surfaces, with the narrowest core-level on the surface annealed at 1200 K for 100 s.

The real-time XPS annealing data for 1200 K for 10 s showed a small increase in binding energy (the largest being 0.22 eV), and a narrowing of the FWHM. This is reminiscent of hydrogen terminated surface but with a much lower magnitude of shift. For the surface annealed at 1200 K for 100 s a new type of behaviour was observed where the binding energy and FWHM remained constant throughout the cycle. This behaviour is different to even the polycrystalline metals reported in Section 4 where a small shift to lower binding energy was observed. It is therefore proposed that the 100 s annealed surface is exhibiting characteristics of a pinned surface due to the surface state associated with the formation of π-bonded carbon dimers. In addition no shift to the C 1s core-level with x-ray flux was observed (Table 5.9), and the formation of the silver-diamond interface with the surface showed no shift with silver coverage (discussed in detail in Section 5.4.3.). This behaviour was predicted by Cui et al who proposed that π-bonded carbon pins the Fermi level and induces a high surface conductivity [38].

Surface photovoltage appeared to be minimal on the reconstructed surfaces with values estimated from the real time XPS annealing of less than 0.2 eV on the briefly annealed surfaces and zero on extendedly annealed surface. The true binding energy therefore appears to be around 285.3 eV and this is in perfect agreement with the silver-diamond interface data (Section 5.3.2). Variations in the true binding energy appear to be dependent on whether the surfaces were recently mechanically polished, with recently polished surfaces having higher binding energies and lower FWHM than the surfaces that had not. A simple explanation for this would be a more ordered surface after mechanical polishing resulting in a more ordered reconstruction or incomplete reconstruction where less than a complete monolayer of π-bonded carbon was formed. This is supported by the lower FWHM of the surface after mechanical polish indicating a more complete/uniform reconstruction. In principle it would be possible to relate the area of the π-bonded component in the C 1s core-level to the electron attenuation length to determine the thickness of the layer and compare to the expected monolayer thickness, however this is difficult in XPS as the technique is not sufficiently surface sensitive resulting in a large uncertainty in the area of the component. LEED can be used to estimate the reconstruction coverage however in this work the patterns were only briefly inspected for the presence of second order diffraction to confirm reconstruction. The LEED patterns shown in Figure 5.5 (which were without mechanical polishing) do reveal the intensity of the second order diffraction spots to be lower than the first order, indicating a less than complete monolayer reconstructed surface.

5.4.3. Silver / diamond interface

The composite plot of three deposition experiments of the C 1s intensity with accumulated deposition time (Figure 5.23) are consistent with Stranski-Krastanov film growth of silver on diamond with no dependency on the surface termination. Using the electron attenuation length for 967 eV electrons (C 1s) through silver, 0.98 nm, the deposition rate in the layer-by-layer region was calculated to be 0.32 nm / min. This value is in agreement with the deposition rate measured with the crystal monitor giving confidence in the value of the electron attenuation length, however it is different to the value reported by Pitter et al (0.62 nm) [52]. The transition from layer-by-layer to island growth occurs at 0.78 nm. The monolayer thickness for silver is around 0.38 nm [53] indicating the formation of 2 monolayers before the transition to island formation.

The C 1s core-level during deposition reveals an inert interface for the reconstructed surface, with evidence of the π-bonded carbon component visible after 0.83 nm of silver. This is in agreement with the results of Bushell who probed the reconstructed (111) surface with LEED during silver deposition and found the 2x2/2x1 pattern to be preserved [48]. However for the hydrogen terminated surface there is some evidence of chemical change occurring. The ratio of the C-O/C-H component to the sp^3 component is reduced with silver coverage, reaching zero with 0.93 nm of silver. If hydrogen were reacting with silver a chemically shifted component in the Ag 3d core-level around 1 eV to higher binding energy would be expected. However due to the low intensity of the core-level it is not possible to corroborate this. Maier et al [50] deposited gold on a hydrogen terminated diamond and reported that no additional chemically shifted components appeared indicating that no reaction between

the gold and the hydrogen had occurred. However they do not report on the exact line-shape of the C 1s.

The binding energy of the carbon and silver core-levels during silver deposition has yielded strong evidence supporting a surface photovoltage at the hydrogen terminated surface. The C 1s core-level at 284.1 eV is shifted gradually with silver coverage to a final value of 285.0 eV at 1.5 nm at a rate of 0.53 eV / nm. Strikingly the Ag 3d core-level also shifts towards higher binding energy with coverage with a similar relative shift to the C 1s towards the bulk film value of 368.2 eV. The shifting of the metal core-level is not expected for conventional metal interface formation. For the reconstructed surface (100 s annealed surface), the C 1s core-level of 285.5 eV does not shift with silver coverage, while there is a small shift to lower binding energy of the Ag 3d core-level. This surface appears free from photovoltage, suggesting the presence of a low resistance path, consistent with a high surface conductivity. This is in agreement with the prediction of Cui et al that the 1400 K reconstructed surface would be semi-graphitic and exhibit metal-like characteristics [38]. The data when plotted together (Figure 5.26), suggests that the Fermi level on the hydrogen terminated surface has been shifted from the real position, and is returned with increasing coverage of silver. This is consistent with the reduction of a photovoltage due to attenuation of x-rays with silver coverage. Further deposition of silver on the surface would be expected to reveal the true location of the C 1s core-level on the hydrogen terminated surface. As an approximation for this work the true location may be evaluated by noting the remaining shift in the Ag 3d towards the bulk value (0.44 eV). This suggests the true value of the C 1s core-level to be 285.3 eV, which agrees with the value from the real-time annealing.

Attenuation of x-rays is dependent on the x-ray absorption coefficient of the overlayer. Roberts monitored the deposition of aluminium, which has an absorption coefficient 26 times less than silver at 1256 eV, on oxygen terminated (001) diamond [26]. A shift to higher binding energy with coverage was measured, however the data is difficult to evaluate as the shift precedes the deposition of aluminium, (this is consistent with the photovoltage theory as heat from the high temperature k-cell increases the diamond temperature and reduces the photovoltage thermally). A maximum shift of 0.28 eV / nm is observed in the data, which is half the rate measured in this work and therefore not in agreement with the x-ray absorption coefficient work. However aluminium is a reactive metal and a surface reaction with the oxygen and carbon is expected which may result in changes to the surface conductivity resulting in the higher rate of peak shift.

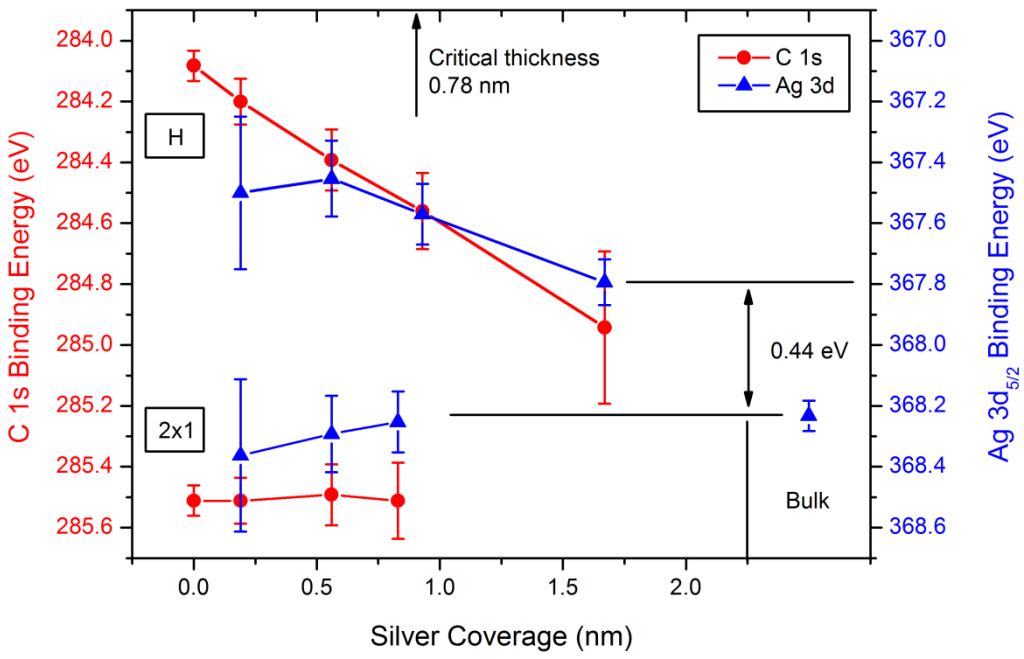

Figure 5.26 Peak positions of the C 1s core-level and Ag $3d_{5/2}$ core-levels for the hydrogen terminated and reconstructed diamond surface. The final hydrogen terminated data point (1.67 nm) has been corrected for the growth mode. Error bars are proportional to the core-level intensity.

5.4.4. Photovoltage model

The real-time XPS annealing data, silver-diamond interface and variable x-ray flux measurements are all consistent with the presence of a surface photovoltage. The photovoltage, due to the accumulation of electrons at the surface from dissociated electron-hole pairs in the depletion region, is removed either thermally (heating), electrically (silver thin films or reconstruction), or by reducing the number of electron-hole pairs (x-ray flux). The photovoltage model published by Hecht [54] requires the maximum photovoltage to be equal or less than the barrier height of surface and this is consistent with reports in the literature for the barrier heights of the hydrogen and oxygen terminated surfaces (≤ 1.3 eV). However the retention of the photovoltage at temperatures greater than room temperature suggests that a mechanism different to that described by Hecht is present.

An additional voltage source may be easily incorporated into the Hecht model by considering the bulk resistance of the diamond, as the product of the photocurrent and the bulk resistance will generate a voltage. An additional parallel resistance will allow the surface conductivity to be taken into account; this will provide a low resistance path for the photocurrent, generating a negligible photovoltage, on the reconstructed surface. Figure 5.27 shows a schematic of the modified electrical circuit that incorporates the bulk and surface resistance.

Point contact current-voltage measurements on the (111) diamond have been made by Roberts [55], the data is shown in Figure 5.28, panel b) along with additional analysis in panel a). As expected for a semiconductor a dependence on the bias is observed; at room temperature the forward and reverse bias resistances are 284 kΩ and 1.3 MΩ respectively.

A simple model where a constant photocurrent generates a voltage through the bulk resistance is presented in Figure 5.30. The model deviates from the data at low temperature but approximates the data well above 600 K. A refinement to the model is possible by considering the photocurrent to be variable due to a dependence on the depletion width. Since the depletion width is a function of the barrier height and the barrier height changes with the amount of photovoltage the photocurrent will vary with temperature.

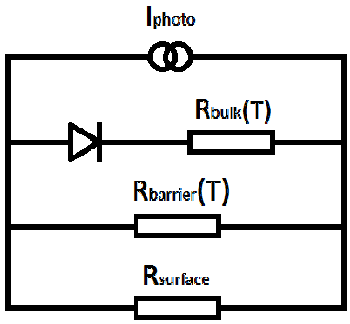

Figure 5.27 Modified SPV model where a series resistance is included to account for the bulk resistance of the diamond and a parallel resistance to account for the surface conductivity.

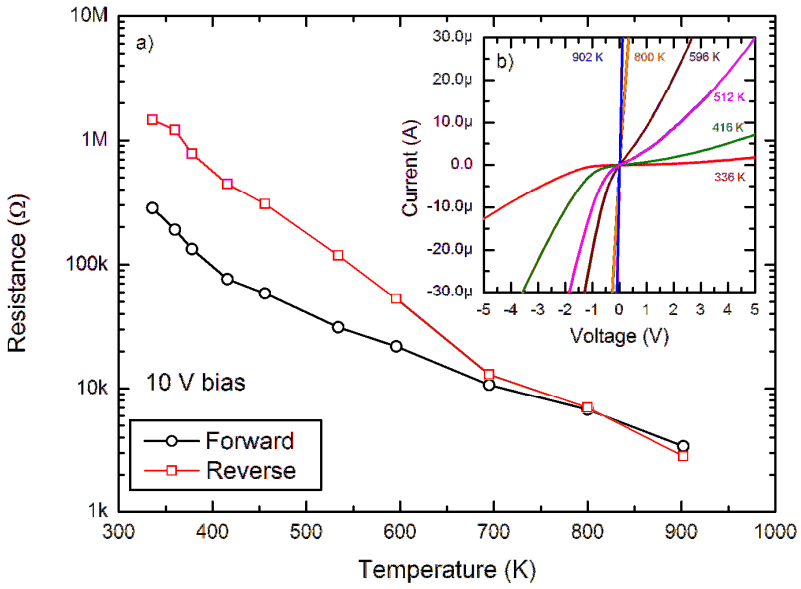

Figure 5.28 Current voltage data for (111) diamond. Panel a) shows the resistance of the diamond against temperature under a forward and reverse bias of 10 V. The IV data, measured by Roberts [55], is shown in panel b).

For a semiconductor the depletion width, given in (5.3), is a function of the band-bending, V_0 – V_{SPV}, where V_{SPV} is a surface photovoltage. The photocurrent is the product of an intrinsic current due to the creation of e-h pairs, the depletion width, and a proportionality constant, as given in (5.4).

$$\mathrm{d} = \sqrt{\frac{2\varepsilon_0\varepsilon_\mathrm{r}(\mathrm{V}_0 - \mathrm{V}_{\mathrm{SPV}})}{\mathrm{qN}_\mathrm{A}}} = \mathrm{B}(\mathrm{V}_0 - \mathrm{V}_{\mathrm{SPV}})^{1/2} \tag{5.3}$$

$$\mathrm{I}_{\mathrm{ph}} = \mathrm{KdI}_0 \tag{5.4}$$

The photocurrent developed by a semiconductor as a function of an intrinsic current (I_0) and the depletion width is given in (5.5). For the photovoltage developed by the semiconductor as a function of the bulk resistance this is simply the photocurrent times the resistance (V = IR), given in (5.6).

$$\mathrm{I}_{\mathrm{ph}} = \mathrm{KBI}_0(\mathrm{V}_0 - \mathrm{V}_{\mathrm{SPV}})^{1/2} \tag{5.5}$$

$$\mathrm{V}_{\mathrm{SPV}} = \mathrm{KBI}_0\mathrm{R}(\mathrm{V}_0 - \mathrm{V}_{\mathrm{SPV}})^{1/2} \tag{5.6}$$

A numerical solution to (5.6) may be found by calculating an initial photovoltage and then using this value to represent the voltage in the next iteration. The photovoltage value of this iteration can then be used as the initial value for the next iteration, and so forth. We therefore have an initial condition (5.7) and an iterative equation for the photovoltage (5.8). As the value of V_{SPV} increases the absorbed current drops to zero at flat-band condition, terminating the model.

$$\mathrm{V}(0) = \mathrm{KBI}_0\mathrm{R}(0)\mathrm{V}_0^{1/2} \tag{5.7}$$

$$\mathrm{V}_{\mathrm{SPV}}(\mathrm{n}) = \mathrm{KBI}_0\mathrm{R}(\mathrm{V}_0 - \mathrm{V}_{\mathrm{SPV}}(\mathrm{n}-1))^{1/2} \tag{5.8}$$

The model is presnted in Figure 5.30. The following coefficients were used: $KBI_0 = 7x10^{-6}$ $AV^{-1/2}$ and V_0 = 1.5 V. The value of KI_0 may be evaluated since B is known (0.001 $mV^{-1/2}$) [56], therefore $KI_0 = 7x10^{-3}$ Am^{-1}. The value of K is the e-h production within the depletion region and is approximated to be 230 m^{-1} ($h\nu/E_G$ = 1253/5.47) giving I_0 as $3x10^{-5}$ A. However this approximation is for monochromatic x-ray radiation of 1253 eV. In this work non-monochromatic radiation was used, with bremsstrahlung radiation extending to 15 keV, which would be expected to increase the e-h production rate. The flat-band C 1s core-level is determined to be 283.9 eV from the saturation of the model.

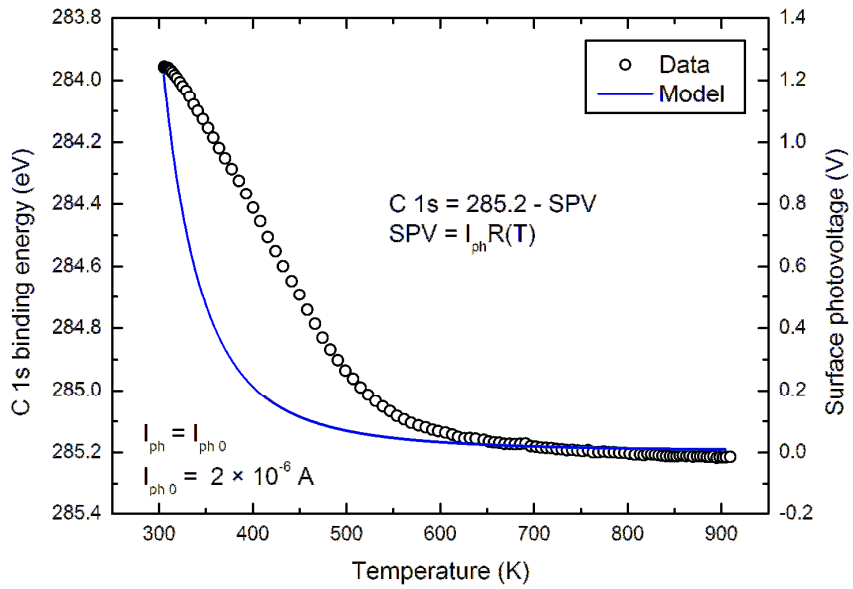

Figure 5.29 Simple V = IR model where the photocurrent is fixed.

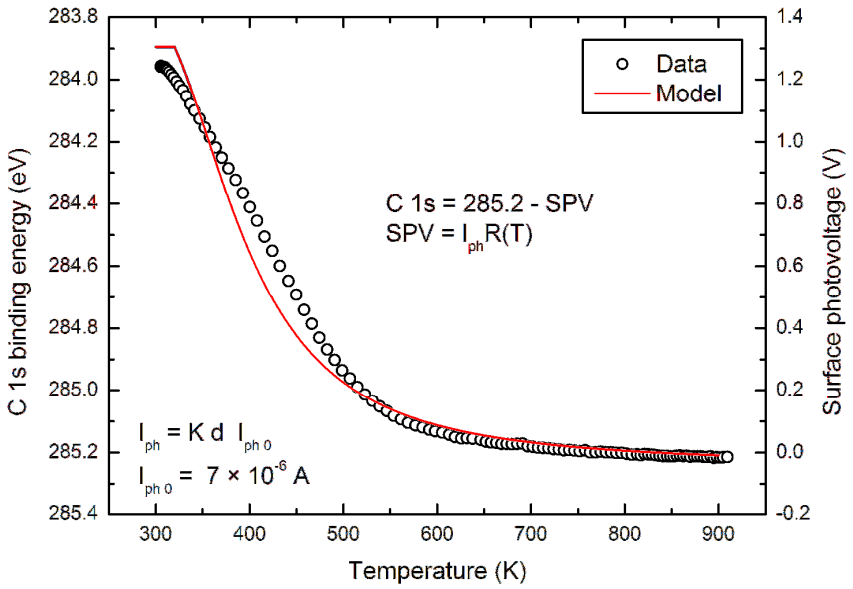

Figure 5.30 Variable photocurrent model where the photocurrent is dependent on the depletion width.

5.4.5. Energy band diagrams

Forming energy band diagrams for the surfaces is problematic as the position of the Fermi level relative to the valence band maximum is not known. This measurement is extremely difficult for diamond as there is a surface state at the same position and the photo-ionization cross-section is not favourable. However the reconstructed surface of this diamond has been measured in the past following a similar preparation method (mechanical polish and 1400 K annealing) by Lübbe et al who reported the Fermi level to be the 2.00 eV above the valence band maximum and the electron affinity to be 0.93 eV [46]. They noted that these values were rather different to those noted by Cui et al for a 1000 K annealed (111) surface (0.88 eV and 0.38 eV for the Fermi level and electron affinity respectively) [40], however Cui et al subsequently published different values for a 1400 K annealed surface, 1.42 eV and 0.83 eV for the Fermi level and the electron affinity respectively [38], closer to the measurement of Lübbe. Using the calculated bulk value of the Fermi level above the valence band (0.32 eV) and the position of the valance band maximum (2.00 eV), the surface band-bending may be calculated (1.68 eV). Furthermore the work function measured by Cui for the reconstructed surface may be used to calculate the value of the electron affinity (1.38 eV) and create an energy band diagram for the surface. The diagram is compared to the energy band diagram measured by Cui for the reconstructed surface in Figure 5.32. The effect of changing the Fermi level has resulted in the flat-band C 1s core-level binding energy changing (or bulk C 1s core-level) from 284.45 eV (determined by Cui) to 283.84 eV in this work.

For the hydrogen terminated surface a comparison of the C 1s core-level to the core-level of the reconstructed surface allows the difference in Fermi level to be calculated. Figure 5.33 a) shows the energy band diagram reported by Cui for an in-situ hydrogenated (111) surface,

with the band diagram of the surface measured in this work in 5.33 b). It is important to note that the value of the bulk C 1s core-level is different in both, as explained in the discussion on the reconstructed surface. If the bulk C 1s core-level reported by Cui (284.45 eV) is applied to the hydrogenated surface used in this work then the hydrogenated surface would have an upwards band-bending of 0.45 eV, which seems highly unlikely. The bulk C 1s core-level value determined from the reconstructed surface (283.84 eV) results in flat-band condition for the hydrogenated surface, which has been reported by workers in the past. This is also in agreement with the model developed for the C 1s core-level binding energy. Figure 5.33 c) shows the energy band diagram of the surface at 700 K where the photovoltage had been removed thermally.

For the oxygen terminated surface the energy band diagram is created with same principle as the hydrogen terminated surface. In Figure 5.34 a) the energy band diagram of the as-prepared surface (7% oxygen content) at 300 K (with photovoltage) is given while Figure 5.34 b) shows the surface at 700 K (without photovoltage).

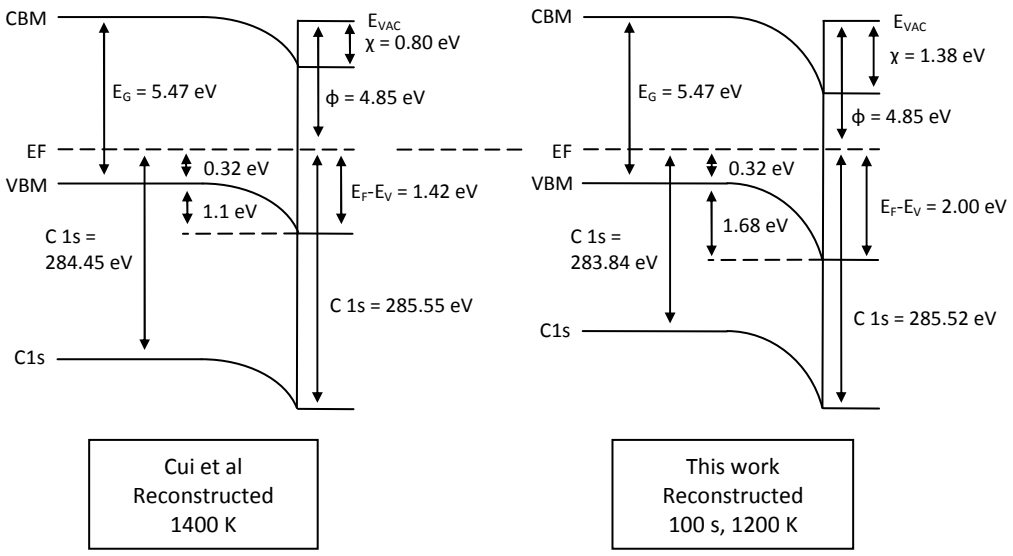

Figure 5.31 Comparison of band-diagram of reconstructed surface reported by Cui et al after 1400 K annealing and the band-diagram for the surface measured in this work. By altering the value of the Fermi level above the valence band at the surface (the band-bending) the same C 1s binding energy is measured in each diagram. The same work function reported by Cui et al is shown on the surface for this work along with the calculated value for the electron affinity.

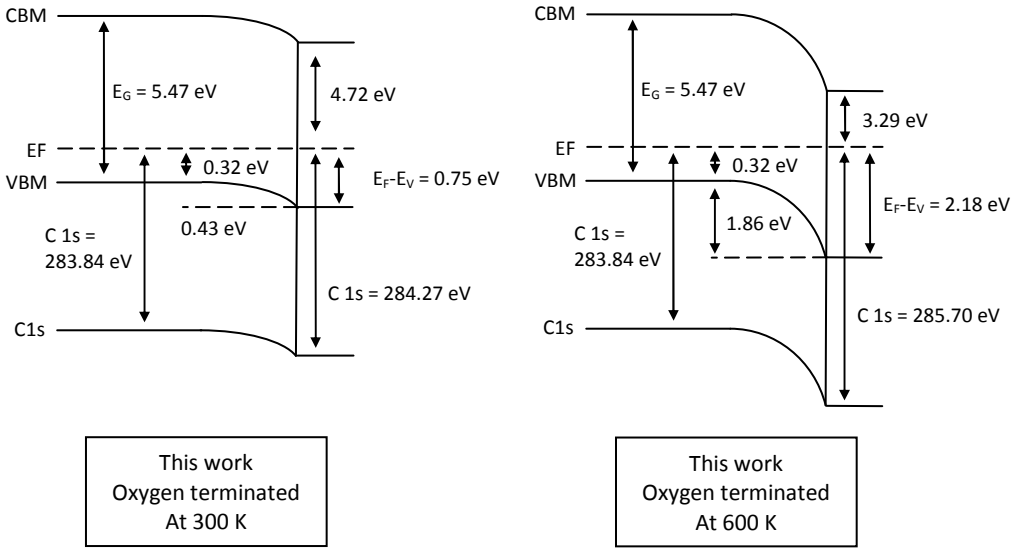

Figure 5.32 Comparison of band-diagram of freshly prepared (not annealed) oxygen terminated surface at room temperature and at 600 K. Work function values are not available for the surface and the position of the vacuum level is therefore unknown.

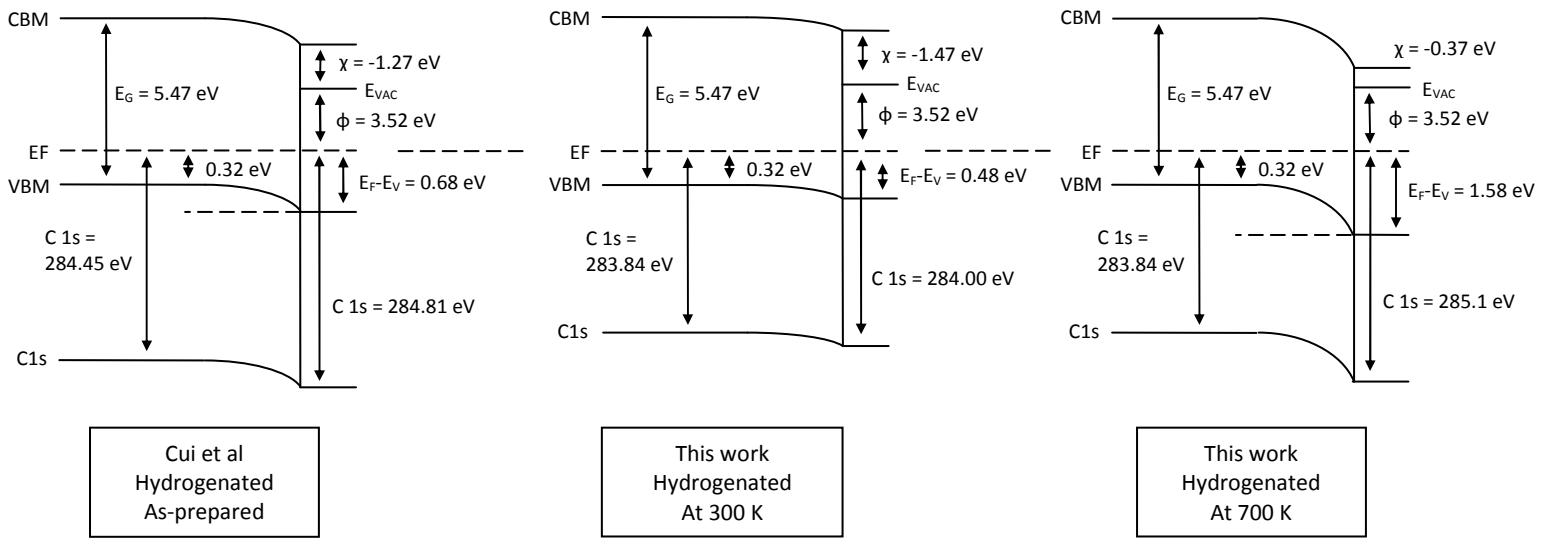

Figure 5.33 Comparison of band-diagram of the hydrogenated surface reported by Cui et al and the band-diagram for the hydrogenated surface measured in this work. By using same bulk C 1s core-level as that determined for the reconstructed surface the valence band at the surface is determined. Assigning the same work function as that determined by Cui et al allows the electron affinity to be calculated.

5.5. Future work

The presence of surface photovoltage could be investigated further through the incorporation of an electrical probe in a chamber equipped with an x-ray source. This would allow the voltage to be directly measured and correlated against the photoelectron spectroscopy data.

The real-time XPS annealing would be greatly enhanced by the addition of a cooling stage for measuring below 300 K. This would allow the saturated binding energy (flat-band condition) to be conclusively determined. A second benefit would be an enhanced cooling rate from 500 K to 300 K which greatly increased the experimental time.

Surface conductivity measurements would be beneficial in identifying the mechanism responsible for the reduced photovoltage on the low oxygen content surfaces. An atomically flat (111) surface would allow the oxygen terminated surface to be investigated in more detail.

For the metal-diamond interface a study of other inert interfaces would be useful for correlating the magnitude of the C 1s core-level shift with metal coverage and x-ray attenuation.

5.6. References

1. Wort, C.J.H. and R.S. Balmer, *Diamond as an electronic material.* Materials Today, 2008. **11**(1-2): p. 22-28.
2. Fong, C.Y. and B.M. Klein, *Electronic and vibrational properties of bulk diamond*, in *Diamond: electronic properties and applications*, L.R. Pan and D.R. Kania, Editors. 1994, Kluwer Academic Publishers: Norwell, USA.
3. Wikipedia commons. *Diamond structure*. Available from: http://upload.wikimedia.org/wikipedia/commons/2/28/Diamonds_glitter.png.
4. Kitawaki, H., *Gem diamonds : causes of colour.* New diamond and frontier carbon technology, 2007. **17**(3): p. 119.
5. Bundy, F.P., *Man-made diamonds.* Nature, 1955. **176**(4471): p. 51-55.
6. Kanda, H. and T. Sekine, *High temperature high pressure synthesis of single crystal diamond*, in *Properties, growth and applications of diamond*, M.H. Nazare and A.J. Neves, Editors. 2000, Short run press: Exeter, UK.
7. Butler, J.E. and D.G. Goodwin, *CVD growth of diamond*, in *Properties, growth and applications of diamond*, M.H. Nazare and A.J. Neves, Editors. 2000, Short run press: Exeter, UK.
8. Balmer, R.S., et al., *Chemical vapour deposition synthetic diamond: materials, technology and applications.* Journal of Physics: Condensed Matter, 2009. **21**(36): p. 364221.
9. Robertson, R., J.J. Fox, and A.E. Martin, *Further Work on Two Types of Diamond.* Proceedings of the Royal Society of London. Series A - Mathematical and Physical Sciences, 1936. **157**(892): p. 579-593.
10. Custers, J.F.H., *Unusual phosphorescence of a diamond.* Physica, 1952. **18**(8-9): p. 489-496.
11. Nebel, C.E. and M. Stutzmann, *Transport properties of diamond: carrier mobility and resistivity*, in *Properties, growth and applications of diamond*, M.H. Nazare and A.J. Neves, Editors. 2000, Short run press: Exeter, UK.
12. Werner, M., et al., *The diamond Irvin curve.* Diamond and Related Materials, 1997. **6**(2-4): p. 308-313.
13. Evans, S., *Surface Properties of Diamond*, in *The properties of natural and synthetic diamond*, J.E. Field, Editor. 1992, Academic: London.
14. Pate, B.B., *The diamond surface - atomic and electronc structure.* Surface Science, 1986. **165**(1): p. 83-142.
15. Kawarada, H., *Hydrogen-terminated diamond surfaces and interfaces.* Surface Science Reports, 1996. **26**(7): p. 205-259.
16. Malshe, A.P., et al., *A review of techniques for polishing and planarizing chemically vapor-deposited (CVD) diamond films and substrates.* Diamond and Related Materials, 1999. **8**(7): p. 1198-1213.
17. Evans, S. and M.R. Ney, *Cobalt-catalysed graphitization of diamond studied by x-ray photoelectron spectroscopy.* Journal of hard materials, 1990. **1**(3): p. 169.
18. Landstrass, I.M. and K.V. Ravi, *Resistivity of chemical vapor deposited diamond films.* Applied Physics Letters, 1989. **55**: p. 975.
19. Ristein, J., et al., *Diamond surface conductivity experiments and photoelectron spectroscopy.* Diamond and Related Materials, 2001. **10**(3-7): p. 416-422.
20. Strobel, P., et al., *Surface transfer doping of diamond by fullrene.* Diamond and Related Materials, 2005. **14**: p. 451-458.
21. Chen, W., et al., *Surface transfer doping of semiconductors.* Progress in Surface Science, 2009. **84**(9-10): p. 279-321.
22. Pate, B.B., *Surfaces and interfaces of diamond*, in *Diamond: electronic properties and applications*, L.R. Pan and D.R. Kania, Editors. 1994, Kluwer Academic Publishers: Norwell, USA.

23. Lurie, P.G. and J.M. Wilson, *The diamond surface: I. The structure of the clean surface and the interaction with gases and metals.* Surface Science, 1977. **65**(2): p. 453-475.
24. Wilson, J.I.B., J.S. Walton, and G. Beamson, *Analysis of chemical vapour deposited diamond films by X-ray photoelectron spectroscopy.* Journal of Electron Spectroscopy and Related Phenomena, 2001. **121**(1-3): p. 183-201.
25. Ri, S.-G., et al., *Surface conductive layers on (111) diamonds after oxygen treatments.* Diamond and Related Materials, 2006. **15**(4-8): p. 692-697.
26. Roberts, O.R., *The Application of Real-Time Photoelectron Spectroscopy to Carbon-Based Semiconductors*. 2009, Aberystwyth University: Aberystwyth.
27. Maier, F., J. Ristein, and L. Ley, *Electron affinity of plasma-hydrogenated and chemically oxidized diamond (100) surfaces.* Physical Review B, 2001. **64**(16): p. 165411.
28. Evans, S. and J.M. Thomas, *The Chemical Nature of Ion-Bombarded Carbon: A Photoelectron Spectroscopic Study of "Cleaned" Surfaces of Diamond and Graphite.* Proceedings of the Royal Society of London. A. Mathematical and Physical Sciences, 1977. **353**(1672): p. 103-120.
29. Klauser, R., et al., *The interaction of oxygen and hydrogen on a diamond C(111) surface: a synchrotron radiation photoemission, LEED and AES study.* Surface Science, 1996. **356**(1-3): p. L410-L416.
30. Pandey, K.C., *New dimerized-chain model for the reconstruction of the diamond (111)-(2x1) surface.* Physical Review B, 1982. **25**(6): p. 4338-4341.
31. Derry, T.E., L. Smit, and J.F. Van Der Veen, *Ion scattering determination of the atomic arrangement at polished diamond(111) surfaces before and after reconstruction.* Surface Science, 1986. **167**(2-3): p. 502-518.
32. Thoms, B.D., et al., *Production and characterization of smooth, hydrogen-terminated diamond C(100).* Applied Physics Letters, 1994. **65**(23): p. 2957-2959.
33. Küttel, O.M., et al., *The preparation and characterization of low surface roughness (111) and (100) natural diamonds by hydrogen plasma.* Surface Science, 1995. **337**(1-2): p. L812-L818.
34. Zheng, J.C., et al., *Oxygen-induced surface state on diamond (100).* Diamond and Related Materials, 2001. **10**(3-7): p. 500-505.
35. Himpsel, F.J., et al., *Surface states on reconstructed diamond (111).* Physical Review B, 1981. **24**(12): p. 7270.
36. van der Weide, J. and R.J. Nemanich, *Argon and hydrogen plasma interactions on diamond (111) surfaces: Electronic states and structure.* Applied Physics Letters, 1993. **62**(16): p. 1878-1880.
37. Saby, C. and P. Muret, *Photoelectron spectroscopy of boron-doped homoepitaxial diamond (100) surfaces with several termination and related Schottky barriers.* Diamond and Related Materials, 2002. **11**: p. 851-855.
38. Cui, J.B., J. Ristein, and L. Ley, *Dehydrogenation and the surface phase transition on diamond (111): Kinetics and electronic structure.* Physical Review B, 1999. **59**(8): p. 5847-5856.
39. Graupner, R., et al., *High-resolution surface-sensitive C 1s core-level spectra of clean and hydrogen-terminated diamond (100) and (111) surfaces.* Physical Review B, 1998. **57**(19): p. 12397.
40. Cui, J.B., J. Ristein, and L. Ley, *Electron affinity of the bare and hydrogen covered single crystal diamond (111) surface.* Physical Review Letters, 1998. **81**(2): p. 429.
41. Ristein, J., W. Stein, and L. Ley, *Defect Spectroscopy and Determination of the Electron Diffusion Length in Single Crystal Diamond by Total Photoelectron Yield spectroscopy.* Physical Review Letters, 1997. **78**(9): p. 1803.
42. Loh, K.P., et al., *Oxygen Adsorption on (111)-Oriented Diamond: A Study with Ultraviolet Photoelectron Spectroscopy, Temperature-Programmed Desorption, and Periodic Density Functional Theory.* The Journal of Physical Chemistry B, 2002. **106**(20): p. 5230-5240.

43. Fyfe, D.J., *The surface properties of diamond and cubic boron nitride*. 2000, University of Wales, Aberystwyth: Aberystwyth.
44. Evans, S. and C.E. Riley, *Angular dependence of x-ray excited valence band photoelectron spectra of diamond.* Journal of the Chemical Society, Faraday Transactions 2: Molecular and Chemical Physics, 1986. **82**: p. 541.
45. Evans, S., *Depth Profiles of Ion-Induced Structural Changes in Diamond from X-Ray Photoelectron Spectroscopy.* Proceedings of the Royal Society of London. A. Mathematical and Physical Sciences, 1978. **360**(1702): p. 427-443.
46. Lübbe, M., et al., *Angular-resolved study of secondary-electron emission from NEA diamond surfaces.* Diamond and Related Materials, 1999. **8**(8-9): p. 1485-1489.
47. Langstaff, D.P., et al., *A fully integrated multi-channel detector for electron spectroscopy.* Nuclear Instruments and Methods in Physics Research Section B: Beam Interactions with Materials and Atoms, 2005. **238**(1-4): p. 219-223.
48. Bushell, A., *A new multi-channel detector for electron spectroscopy and its application to single crystal diamond*. 2005, Univeristy of Wales, Aberystwyth: Aberystwyth.
49. Long, J.P. and V.M. Bermudez, *Band bending and photoemission induced surface photovoltages on clean n- and p-GaN (0001) surfaces.* Physical Review B, 2002. **66**: p. 121308.
50. Maier, F., et al., *Spectroscopic investigations of diamond / hydrogen / metal and diamond / metal interfaces.* Diamond and Related Materials, 2001. **10**: p. 506.
51. Cui, J.B., et al., *Noncontact temperature measurements of diamond by Raman scattering spectroscopy.* Journal of Applied Physics, 1998. **83**(12): p. 7929-7933.
52. Pitter, M., M.B. Hugenschmidt, and R.J. Behm, *Electron spectroscopy study of the silver-diamond(100)-H interface.* Applied Physics Letters, 1996. **69**(26): p. 4035-4037.
53. Seah, M.P. and W.A. Dench, *Quantitative electron spectroscopy of surfaces: A standard data base for electron inelastic mean free paths in solids.* Surface and Interface Analysis, 1979. **1**(1): p. 2-11.
54. Hecht, M.H., *Photovoltaic effects in photoemission studies of Schottky barrier formation.* Journal of Vacuum Science & Technology B: Microelectronics and Nanometer Structures, 1990. **8**(4): p. 1018-1024.
55. Roberts, O.R., *Diamond (111) to Au probe in-situ in the dark*. 2007, Aberystwyth University.
56. Bandis, C. and B.B. Pate, *Room temperature photovoltaic charging in photoemission from diamond.* Surface Science, 1996. **345**(1-2): p. L23-L27.

6. Zinc oxide

In this section investigations into the surface processing of single crystal zinc oxide is presented. Of interest is the interaction of oxygen plasma with the surface, the effect of annealing, and the formation of organic interfaces.

6.1. Introduction

Zinc oxide is a compound composed of equal amounts of zinc and oxygen in the wurtzite crystalline configuration. The material is also thermodynamically stable in the zincblende and rocksalt configuration although these are not found naturally and growth is difficult [1].

ZnO is a wide band-gap semiconductor with a direct band-gap of 3.37 eV, has a high exciton binding energy (60 meV), has high resistance to radiation damage, and has a natural n-type characteristic. The source of the natural doping is still controversial however it is thought to be due to oxygen vacancies and interstitial zinc [2-3]. Oxygen vacancies are suspected of being responsible for the green luminescence centre of ZnO (2.5 eV) and have been found to be concentrated in the sub-surface [4]. Increasing the n-type characteristic may be accomplished by doping with Al, Ga or In [3] or by decreasing the concentration of oxygen vacancies. P-type doping is a major challenge for ZnO and as present reliable methods have not been developed.

Applications

Industrially one of the most important uses of ZnO is as a catalyst in the production of methanol [5]. It is also used as a gas sensor due to surface conductivity change in the presence of hydrogen [6].

Being a wide band-gap semiconductor the most obvious application of ZnO is UV optoelectronics. UV lasing [7], blue electroluminescence [8], and UV photodiodes [9] have been successfully demonstrated. A promising field is photovoltaic applications where the surface conductivity and transparency make ZnO an ideal transparent conducting oxide [10]. Traditional devices based on inorganic semiconductors with high efficiencies have been reported based on cadmium sulphide [11]. Specialized schemes including quantum ZnO/CdSe quantum dots have also been demonstrated [12]. The use of ZnO has also been reported to improve the performance of dye-sensitized solar cells [13-14]. Hybrid organic devices where organic semiconductors are used for photovoltaic action are being extensively investigated, and devices in conjunction with organic materials such as P3HT [15], MDMO-PPV [16], C60 [17], CuPc [18], blends of C60 and CuPc [19], and blends of ZnO:CuPc [20].

ZnO is also suitable for spintronics, electronic devices that utilize the electron spin [21], and room temperature ferromagnetism has been predicted for Mn-doped ZnO [22].

There are two main methods of producing high quality single crystal ZnO; hydrothermal solution growth [23] and pressurized melt growth [24]. The hydrothermal growth produces crystals with lower oxygen vacancies and thus lower intrinsic carrier concentrations ($1x10^{14}$ cm^{-3}) compared to the pressurized melt growth ($1x10^{15}$ cm^{-3}) [25], however the growth rate achieved by the pressurized melt method is much greater than the hydrothermal method.

Polar surfaces

The wurtzite crystalline structure has tetrahedral coordination of the zinc and oxygen atoms, that is each zinc atom is coordinated with four oxygen atoms, and vice versa. An illustration of the unit cell is shown in Figure 6.1. Truncation of the structure results in surfaces with different stoichiometry, for example the $(10\bar{1}0)$ and $(11\bar{2}0)$ surfaces are composed of equal quantities of zinc and oxygen, while the (0001) surface is terminated with zinc only and the $(000\bar{1})$ surface is terminated with oxygen only [5]. The two latter surfaces, shown in Figure 6.2, are known as the polar surfaces and are electronically unstable due to the presence of a periodic dipole moment resulting in an electrostatic field. Such surfaces have been the subject of some interest since they were described by Tasker [26]. To overcome the instability a stabilization mechanism is required and three are often proposed for ZnO; charge transfer between the surfaces, surface reconstruction, and adsorption of hydroxide [27]. Charge transfer has been investigated by Wander et al [28] who performed ab-initio calculations with surface x-ray diffraction. Their model suggested that a charge transfer of 0.17e from Zn to O would stabilize the surfaces and that the charge must be concentrated within the first three bilayers. Band structure calculations reveal that both surfaces would be metallic however the mechanism is slightly different for the two polar faces due to different contributions from zinc 4s and d states and oxygen p states. Reconstruction of the zinc polar face has been observed by Dulub et al [29] who observed triangular shaped islands, indicating that partial surface reconstruction had occurred. It was proposed that a reduction in the surface concentration of zinc resulted in the stabilization. There are no reports of a clean (0001):Zn surface and termination with hydrogen to form zinc hydride, (0001):Zn-H, is also unstable with the formation of a stable hydroxide surface occurring even in UHV giving

(0001):Zn-OH(1x1) [30]. The oxygen is believed to be drawn from the sub-surface resulting in substantial defects [31], and these defects are thought to be responsible for the surface conductivity changes that result from hydrogen exposure [6].

The $(000\bar{1})$ surface is known to have a clean surface $(000\bar{1})$:O(1x3) [32-33] when carefully prepared with a 1x3 surface structure [33]. However the surface is highly reactive towards hydrogen and background hydrogen pressure in UHV environment will result in the formation of the stable hydroxide terminated surface, $(000\bar{1})$:O-H(1x1), in as little as 30 minutes.

Determining the polarity of ZnO surfaces is difficult due to the similar surface chemical composition and surface structure. Two methods reported in the literature are x-ray diffraction [34] and ion scattering spectroscopy [35]. While both methods conclusively determine the polarity, they are difficult and slow to perform. A recent observation of a variation in the intensity of valence band features for the polar surfaces has been reported [27]. However the method is relative and determination of the termination requires measuring both surfaces.

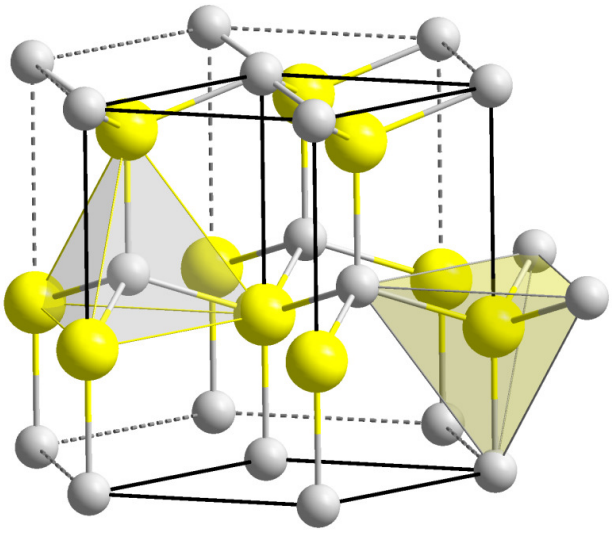

Figure 6.1 Wurtzite ZnO structure. Zinc atoms large and yellow and oxygen atoms small and grey. Illustration from [36].

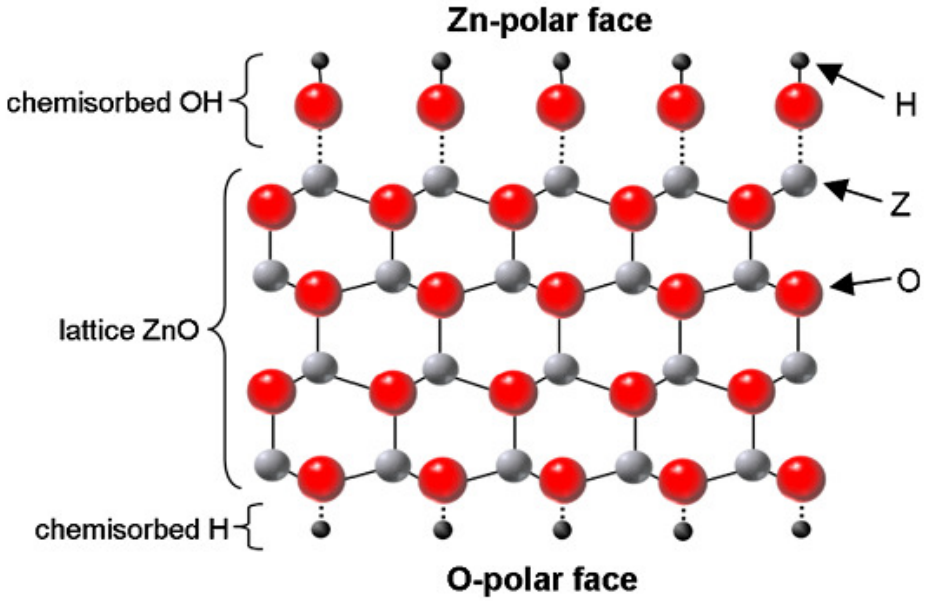

Figure 6.2 Zinc oxide crystalline structure viewed perpendicular to the c-axis. The zinc polar face (top) is shown terminated with hydroxide while the oxygen polar face is shown terminated by hydrogen. Both surfaces therefore have hydroxide character. Illustration from [27].

Work function values for the polar faces are varied in the literature. Allen et al [25] report 4.5 – 4.8 eV for the (0001) surface and 4.7 – 4.9 eV for the $(000\bar{1})$ surface. However these results are at odds with previously reported measurements of ZnO where the (0001) surface was found to have a low work function (3.6 eV) and the $(000\bar{1})$ to have a high work function (4.8 eV) [37]. However it is likely that the difference in sample quality, bulk properties and surface preparation would have a significant effect on the value of the work function. In particular the position of the Fermi level at the surface relative to the position in the bulk is extremely sensitive to the surface adsorbates and bulk crystalline quality [25].

The position of Fermi level relative to the valence band maximum at the surface leads to an interesting effect, that of surface electron accumulation, due to the Fermi level being above the conduction band minimum at the surface. This is illustrated in Figure 6.3 for the two polar faces of ZnO.

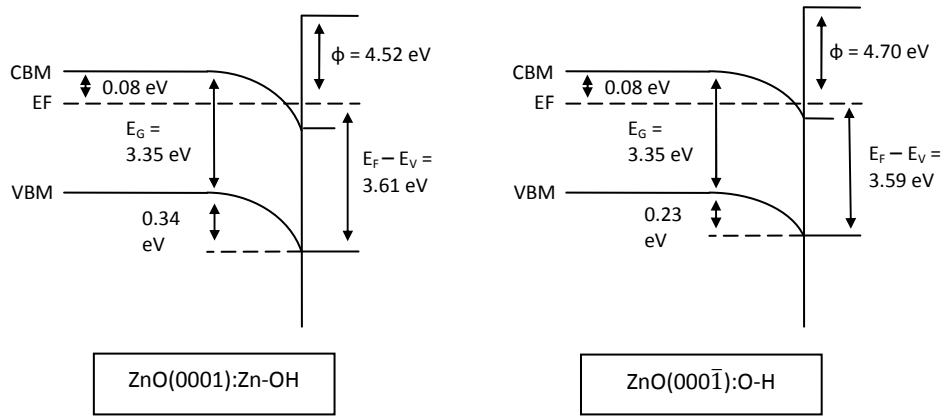

Figure 6.3 Band-diagram for the two polar faces of ZnO. Data for pressurized melt samples from [25].

6.2. Experimental

Several ZnO crystals measuring 10.0 mm x 10.0 mm x 506 µm were provided by Dr. Martin W. Allen of Canterbury University, New Zealand, supplied by Tokyo Denpa Co., with a bulk resistivity of 0.3 Ω-cm and a carrier concentration of $n > 10^{17}$ cm^{-3}.

Sample preparation

The sample was initially cleaned by agitation in acetone. Affixing to a pre-annealed (1200 K) sample holder was done with and without an indium back contact. For preparing an indium back contact the sample holder was heated to 200 °C on a hot plate and a small piece of indium wire was placed onto the holder. The sample was then placed within the holder, the hot plate switched off, and during cooling the sample clips were folded to hold the sample in position. If an indium back contact was not required then the sample was simply placed in the holder and the clips folded to hold in place.

The sample holder and sample were then subjected to an organic solvent cleaning routine; 8 minutes of agitation in acetone, flushing with methanol, flushing with isopropanol, and drying with N_2 gas. Samples were then transferred quickly into the vacuum system. On some occasions the agitation loosened the indium contact. If this occurred the entire procedure was repeated.

For the real-time XPS experiments the analyser parameters are listed in Table 6.1.

A photograph of a ZnO sample under x-ray irradiation in the analysis chamber is presented in Figure 6.4. Green luminescence is visible from the ZnO, while the boron nitride heater produces blue luminescence.

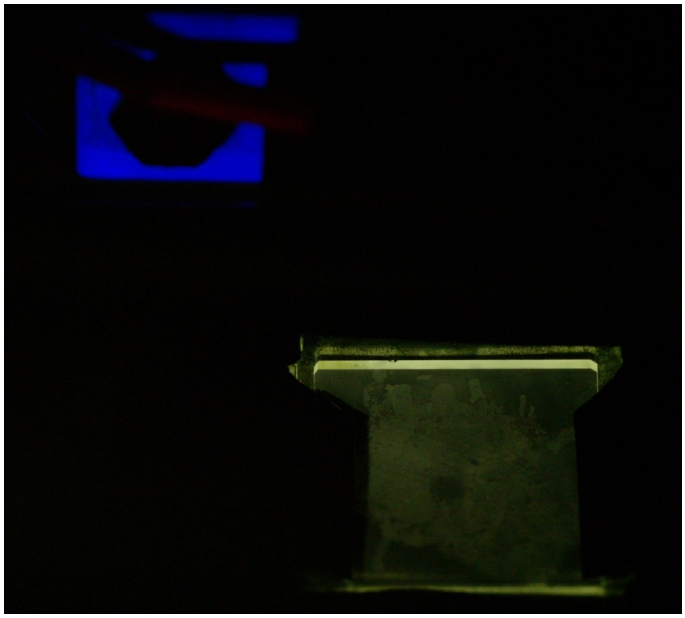

Figure 6.4 Zinc oxide sample under x-ray irradiation with green luminescence. Top left corner shows blue luminescence of boron nitride (BN) heater. Wetted indium is visible behind the ZnO crystal.

Processing	Spectral feature	X-ray source	Energy (eV)		Acquisition time (s)
			Kinetic	Pass	
Annealing	Zn 2p	Mg	227	60	2
	O 1s	Mg	718	60	1
OMBD	C 1s	Al	1201	60	2
	N 1s	Al	1087	60	4
	Zn 2p	Al	465	60	2
	Cut-off	-	5	20	0.1

Table 6.1 Spectrometer parameters for real-time XPS experiments. For the OMBD experiments a bias of -5 V was applied to the sample.

6.3. Results

Results of the surface processing of (0001) and $(000\bar{1})$ surfaces of ZnO are presented here.

6.3.1. Clean surfaces

As-loaded ZnO surfaces were measured to contain 6% carbon and a near equal amount of zinc and oxygen. Exposure to oxygen plasma for 10 minutes removed all carbon giving a clean surface. A survey spectrum of a clean (0001) surface is presented in Figure 6.5 after 12 hours in vacuum. It was necessary to measure the survey spectrum with aluminium Kα x-rays as the zinc auger peaks are close to the C 1s core-level when measuring with magnesium Kα x-rays. In Figure 6.6 the core-levels of the (0001) surface are presented, as-loaded, after 40 minutes oxygen plasma exposure and after annealing at 570 K, with the fitting parameters given in Table 6.2. Changing the x-ray flux did not have any effect on the binding energy of the Zn $2p_{3/2}$ core-level on the (0001) surface. For the $(000\bar{1})$ surface the fitting parameters are given in Table 6.3 for a surface after 20 minutes of oxygen plasma followed by 570 K annealing. Within the experimental uncertainty surfaces exposed to oxygen plasma for 10 minutes or more are identical with a Zn/O ratio of 1.3 ± 0.1.

Several (0001) surfaces were measured following exposure to oxygen plasma and the binding energy of the Zn $2p_{3/2}$ core-level is presented in Figure 6.7 panel a) as a function of oxygen plasma exposure time. An exponential fit has been calculated for the data giving a saturation binding energy of 1021.75 eV. Real-time XPS annealing was performed on oxygenated (0001) surfaces and the Zn $2p_{3/2}$ binding energy during a 575 K and 700 K cycle is presented in panels b) and c) of Figure 6.7. A temperature of 580 ± 20 K was determined from the data for the production of surfaces characteristic of being annealed (up to 1000 K).

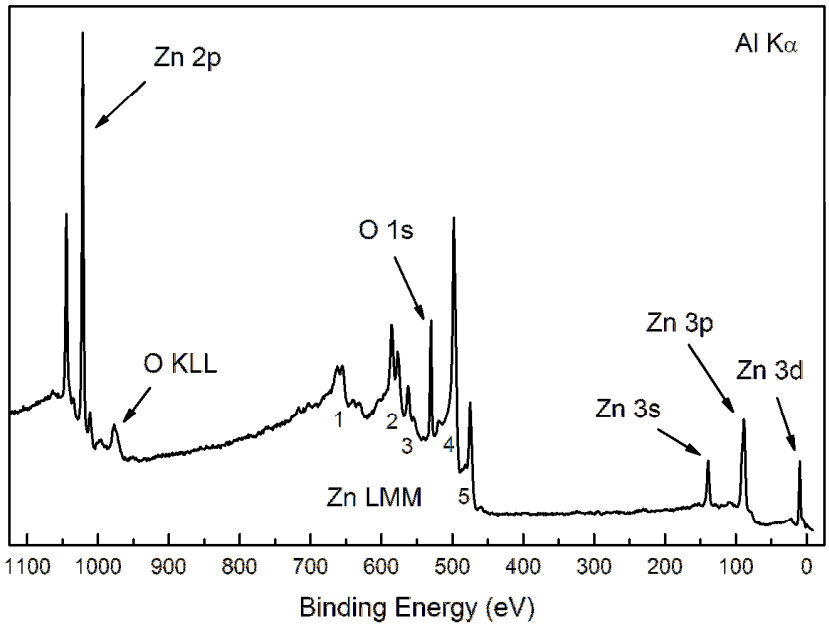

Figure 6.5 Survey spectrum of ZnO(0001). Zinc LMM auger peaks labelled 1, 2, 3, 4, 5.

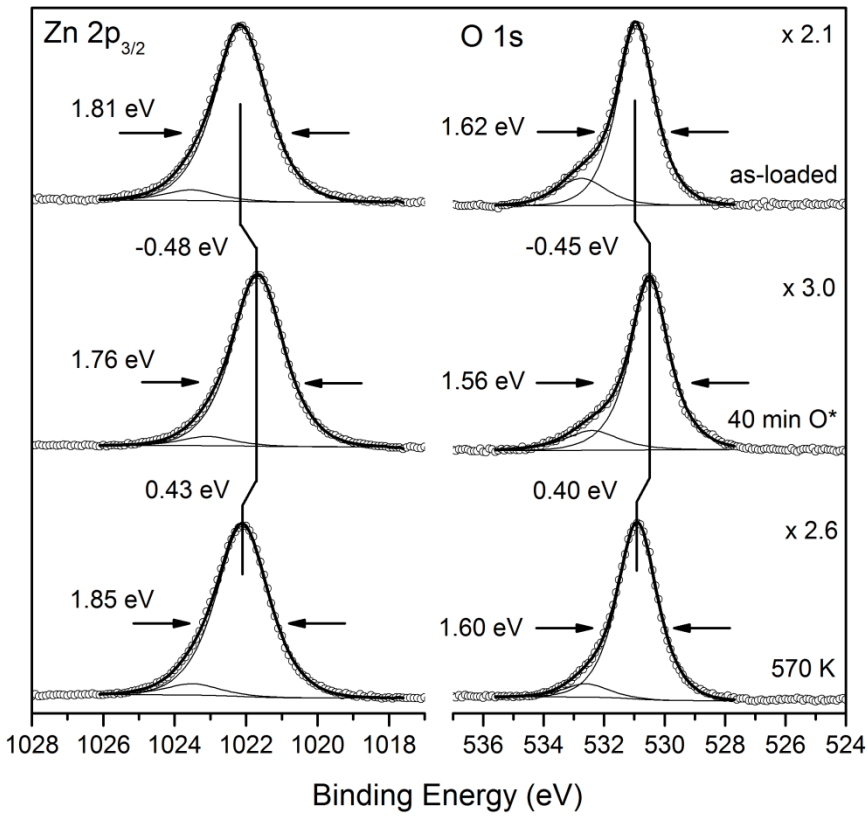

Figure 6.6 Zn $2p_{3/2}$ and O 1s core-levels of ZnO(0001) for the as-loaded surface, after 40 minutes of oxygen plasma exposure and after annealing at 570 K.

Data set	Core-level		Binding energy	FWHM	I / II	Atomic % (± 1)	Zn / O (± 0.1)	Zn I / O I (± 0.1)
as-loaded	O 1s	I II	531.05 532.85	1.46 1.90	1.00 0.19	51.9	0.93	1.04
	Zn 2p3/2	I II	1022.25 1023.65	1.73	1.00 0.06	48.1		
10 min O*	O 1s	I II	530.90 532.70	1.40 2.03	1.00 0.17	45.6	1.19	1.40
	Zn 2p3/2	I II	1022.05 -	1.82 -	1.00 -	54.4		
30 min O*	O 1s	I II	530.65 532.55	1.44 2.16	1.00 0.22	43.2	1.31	1.53
	Zn 2p3/2	I II	1021.80 1023.20	1.69	1.00 0.05	56.8		
40 min O*	O 1s	I II	530.60 532.50	1.49 2.09	1.00 0.16	43.8	1.28	1.41
	Zn 2p3/2	I II	1021.80 1023.20	1.68	1.00 0.05	56.2		
40 min O* + 570 K	O 1s	I II	531.00 532.70	1.55 1.71	1.00 0.08	45.1	1.22	1.24
	Zn 2p3/2	I II	1022.20 1023.60	1.73	1.00 0.06	54.9		
20 min O* + 720 K	O 1s	I II	531.05 532.75	1.47 1.76	1.00 0.11	43.4	1.31	1.37
	Zn 2p3/2	I II	1022.20 1023.60	1.71	1.00 0.06	56.6		

Table 6.2 Chemical composition of ZnO(0001) surfaces following oxygen plasma exposure and annealing. Two samples are included, separated by the heavier line.

Data set	Core-level		Binding energy	FWHM	I / II	Atomic % (± 1)	Zn / O (± 0.1)	Zn I / O I (± 0.1)
20 min O* + 670 K	O 1s	I II	530.90 532.70	1.46 1.75	1.00 0.11	42.2	1.37	1.45
	Zn 2p3/2	I II	1022.10 1023.50	1.8	1.00 0.05	57.8		

Table 6.3 Chemical composition of ZnO($000\bar{1}$) surface following oxygen plasma exposure and annealing.

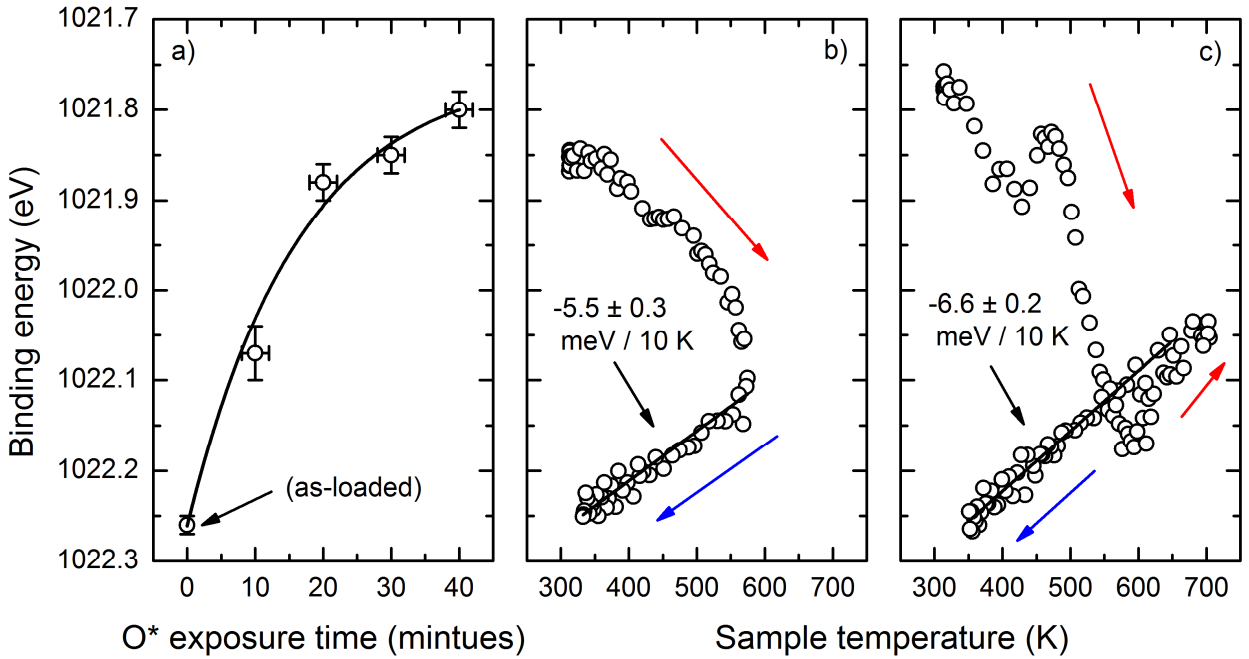

Figure 6.7 Effect of oxygen plasma exposure and annealing on the binding energy of the Zn $2p_{3/2}$ core-level of ZnO(0001). Panel a) shows the effect of oxygen plasma exposure time, zero time being the as-loaded surface. Solid line is an exponential fit. Panels b) and c) show real-time XPS annealing of oxygenated ZnO(0001) surfaces. The cooling sections have been fitted with a linear curve.

Surfaces having been exposed to oxygen plasma and annealed up to 700 K were measured with real-time XPS annealing. Figure 6.8 presents the Zn $2p_{3/2}$ binding energy during real-time XPS annealing of the (0001) and $(000\bar{1})$ surfaces. Regions of interest have been fitted with a linear curve and the gradient given. The binding energy of the Zn $2p_{3/2}$ core-level of the (0001) surface was found to be symmetrical (heating and cooling) and fully reversible (returning to the same binding energy at room temperature). The $(000\bar{1})$ surface exhibited a non-symmetrical shift but was fully reversible when room temperature was reached during cooling. The O 1s core-level was found to shift in the same direction and by the same amount as the Zn $2p_{3/2}$ core-level. The Zn $2p_{3/2}$ core-level for both surfaces exhibited a small broadening during the cycles of less than 100 meV at high temperature that was fully reversible and symmetric.

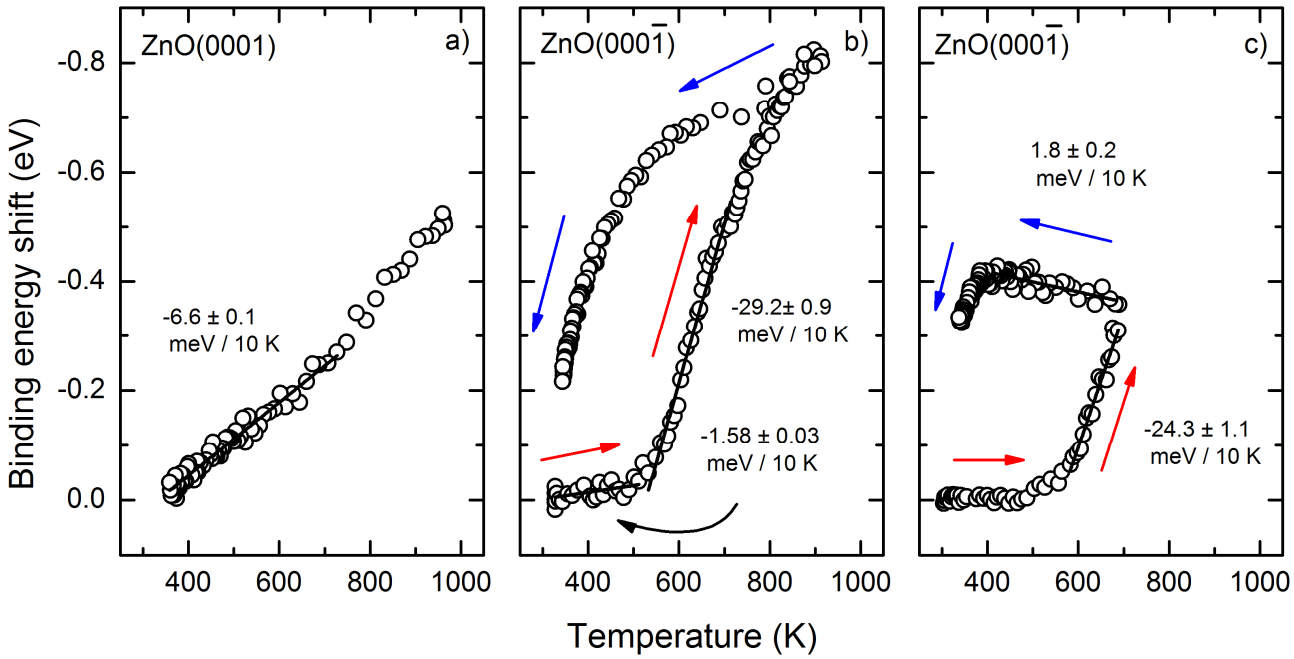

Figure 6.8 Binding energy shift of the Zn $2p_{3/2}$ core-level of the ZnO(0001) and ZnO(000$\bar{1}$) surfaces during annealing. Panel a) shows the heating part of a 900 K annealing cycle on the ZnO(0001) surface. Panel b) shows a 900 K cycle ZnO(000$\bar{1}$) surface. Panel c) shows a 700 K annealing cycle on the same ZnO(000$\bar{1}$) sample subsequent to the 900 K cycle. The data in panels b) and c) were fully reversible (returning to the starting binding energy) however due to the low rate of cooling the data was not collected.

6.3.2. Organic interfaces

ZnO(0001) surfaces, having been prepared by exposure to oxygen plasma and annealing up to 700 K, were exposed to CuPc and C60 (in separate experiments) to form organic interfaces while measuring in real-time. Aluminium Kα x-rays were used for real-time XPS OMBD since the zinc auger peaks are close to the C 1s core-level of CuPc and C60.

The attenuation of the Zn $2p_{3/2}$ core-level during formation of the organic overlayer are presented in Figure 6.9, panel a) for the CuPc and panel b) for the C60. where the attenuation is given by the natural logarithm of the ratio of the intensity to the intensity of the clean surface. The electron attenuation length in CuPc and C60 for 464 eV electrons is 1.1 ± 0.2 nm [38-39], and the deposition rate for CuPc and C60 are calculated as :

$$\begin{aligned} r_{CuPc} = m_{CuPc}\,\lambda &= (0.00296\ s^{-1}) \times 1.1\ nm \\ &= 0.19\ \pm 0.03\ nm/min \\ r_{C60} = m_{C60}\,\lambda &= (0.00145\ s^{-1}) \times 1.1\ nm \\ &= 0.10\ \pm 0.02\ nm/min \end{aligned}$$

For the formation of the ZnO(0001)/CuPc interface the binding energy change of the overlayer and substrate core-levels is presented in Figure 6.10; panels a) and b) for the C 1s and N 1s core-levels of the overlayer and panels c) and d) for the Zn $2p_{3/2}$ core-level of the substrate. The change in the secondary electron cut-off is presented in Figure 6.11, the cut-off snapshots at times t = 0, t = 16 and t = 70 minutes in panel a) and a contour plot of the cut-off during the first 16 minutes in panel b). The work function change of the surface is calculated by noting the change in the secondary electron cut-off and the binding energy change of the overlayer, and this is presented in Figure 6.12. The work function change of the ZnO(0001)/CuPc interface is calculated to be 0.80 eV. Since the work function of CuPc is known to be 4.21 eV the work function of the (0001) surface is calculated to be 5.01 eV.

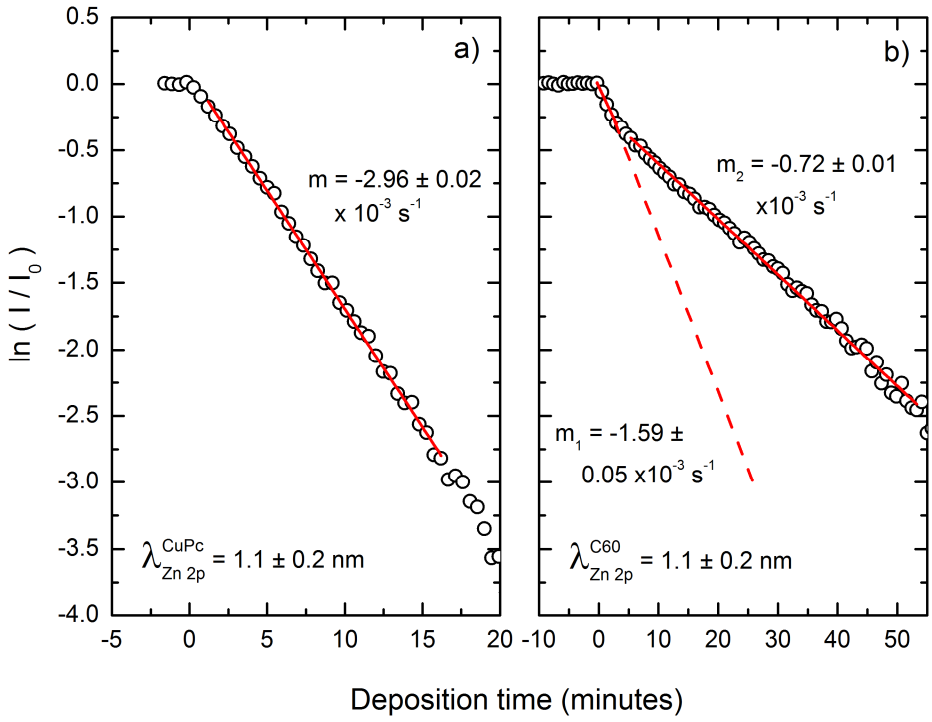

Figure 6.9 Attenuation of the Zn $2p_{3/2}$ core-level during deposition of organic overlayer on ZnO(0001); panel a) CuPc an panel b) C60.

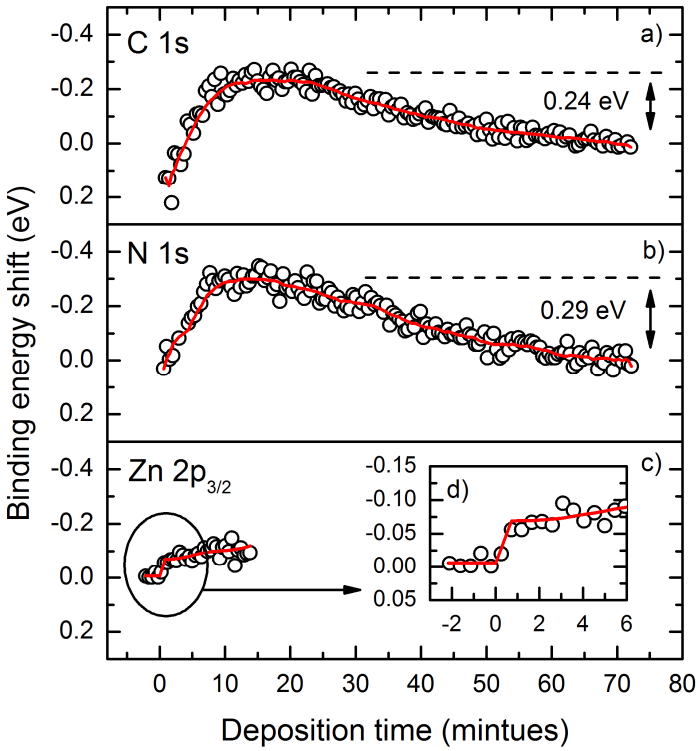

Figure 6.10 Overlayer and substrate core-level shifts during CuPc deposition on ZnO(0001). Panels a) and b) C 1s and N 1s core-level of overlayer, panels c) and d) Zn 2p core-level of substrate.

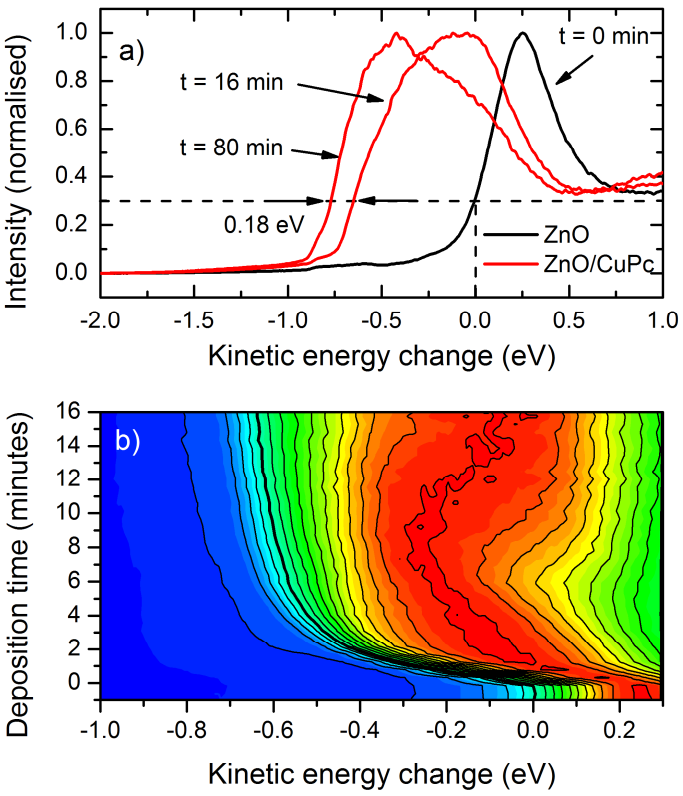

Figure 6.11 Secondary electron cut-off change during deposition of CuPc on ZnO(0001). Panel a) shows snapshots of cut-off at deposition times t = 0, 16 and 80 minutes. Panel b) shows a contour plot of the cut-off between t = -5 and 16 minutes.

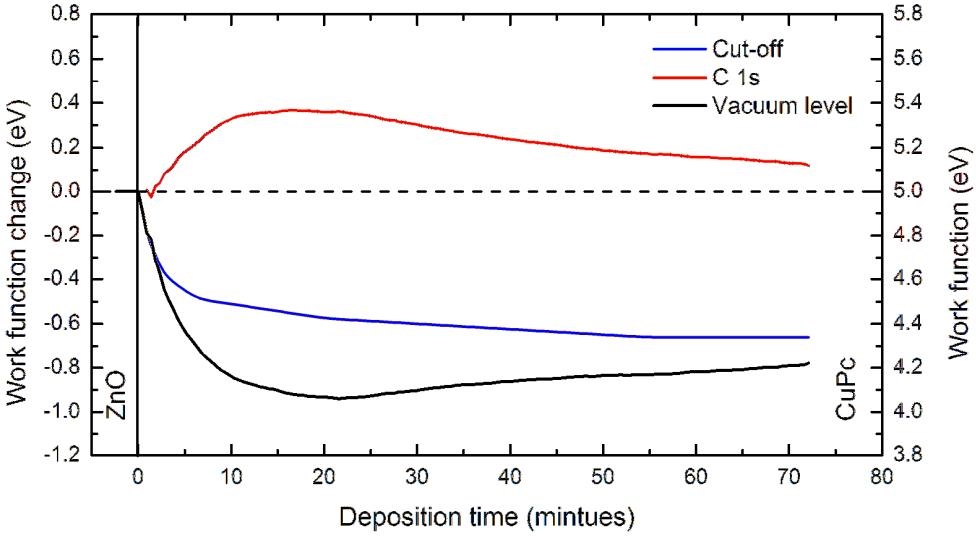

Figure 6.12 Secondary electron cut-off, C 1s core-level and work function change during CuPc deposition on ZnO(0001).

For the formation of the ZnO(0001)/C60 interface a survey spectrum of the C60 overlayer is presented in Figure 6.13 with the associated chemical composition in Table 6.4. The C 1s core-level is presented in Figure 6.14; panel a) for the main core-level and panel b) for the plasmon region. It was necessary to fit the core-level with two main components, each with associated plasmon features (relative position, width and intensity to the core-level component as documented in Section 3). The fitting parameters are given in Table 6.5. In Figure 6.14 panel c) the best fit of the plasmon region is given if plasmon structure from the main core-level component is included only. The binding energy change of the overlayer and substrate is presented in Figure 6.15. The C 1s snapshots were fitted with two components in the same ratio as that determined from the C 1s core-level. In Figure 6.13 the secondary electron cut-off change during the formation of the interface is presented. For the ZnO(0001)/C60 interface the work function change is calculated to be -0.41 eV. Since the work function of C60 is known to be 4.72 eV [40] the work function of the (0001) surface is calculated to be 5.13 eV.

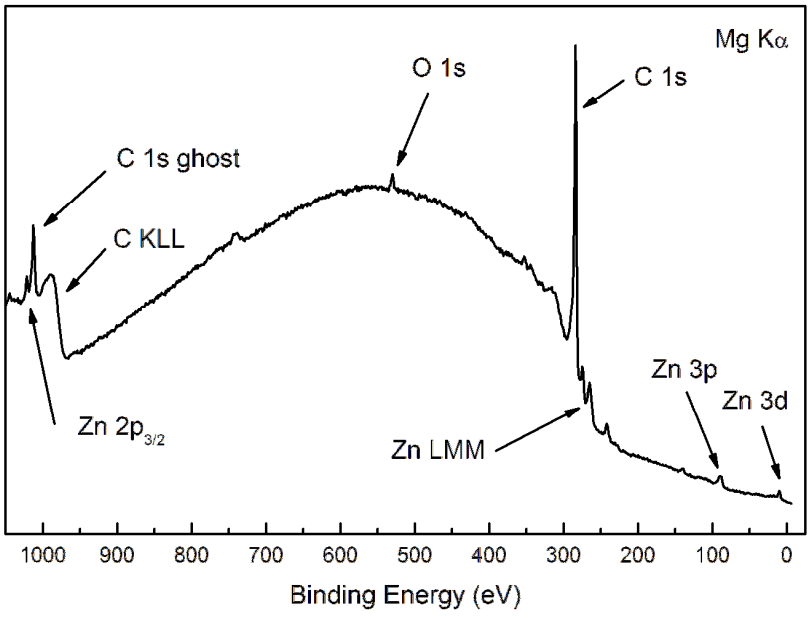

Figure 6.13 Survey spectrum of ZnO(0001)/C60 interface.

Element	Chemical composition (%)
C	97.6
O	1.5
Zn	0.9

Table 6.4 Chemical composition of ZnO(0001)/C60 interface

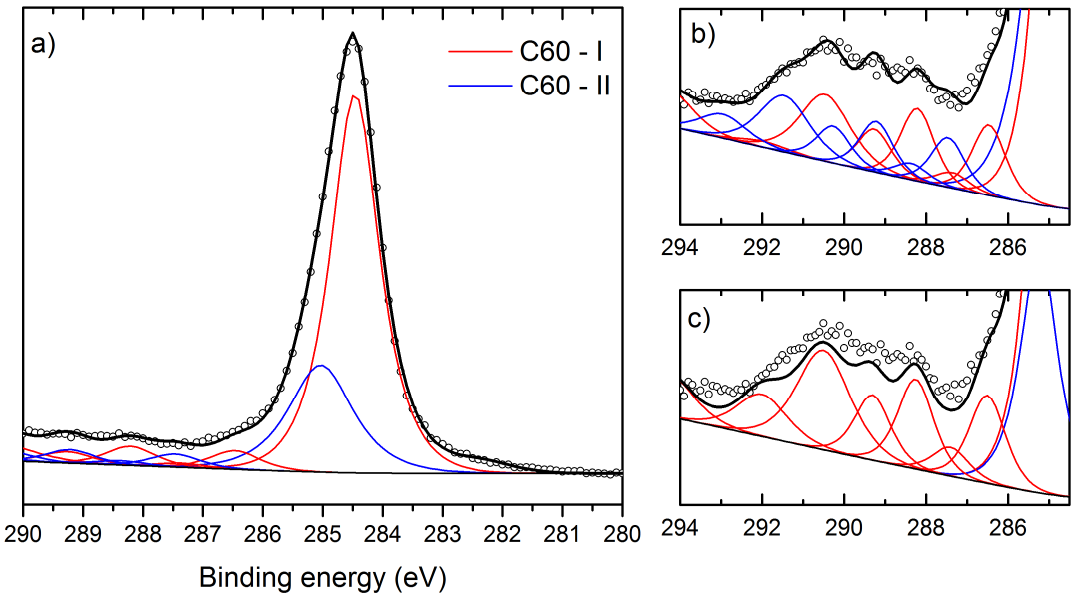

Figure 6.14 Plasmon region of C 1s core-level of ZnO(0001)/C60 interface. Panel a) shows the main C 1s core-level and panel b) the plasmon region with an associated plasmon structure for each core-level. Panel c) is a two core-level component fit but plasmon structure for main component only.

Core-level		Binding Energy	FWHM	Ratio
C 1s	I	284.6	0.93	1.00
	II	285.0	1.20	0.41

Table 6.5 C 1s core-level fitted components for ZnO(0001)/C60 interface.

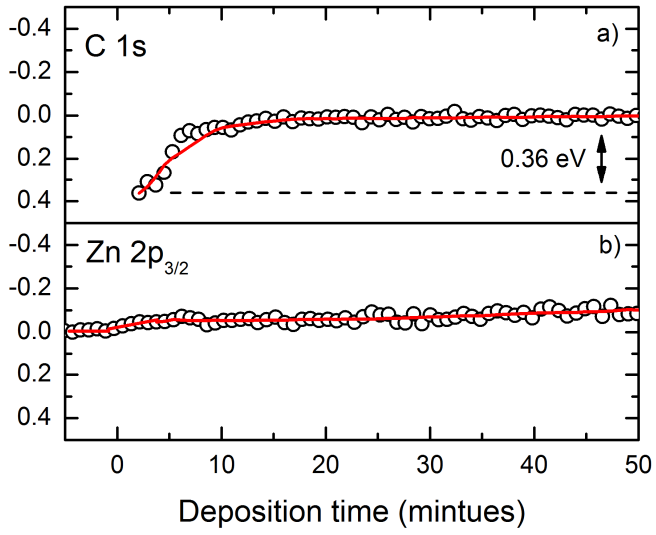

Figure 6.15 Substrate and overlayer core-level binding energy shift during ZnO(0001)/C60 interface formation.

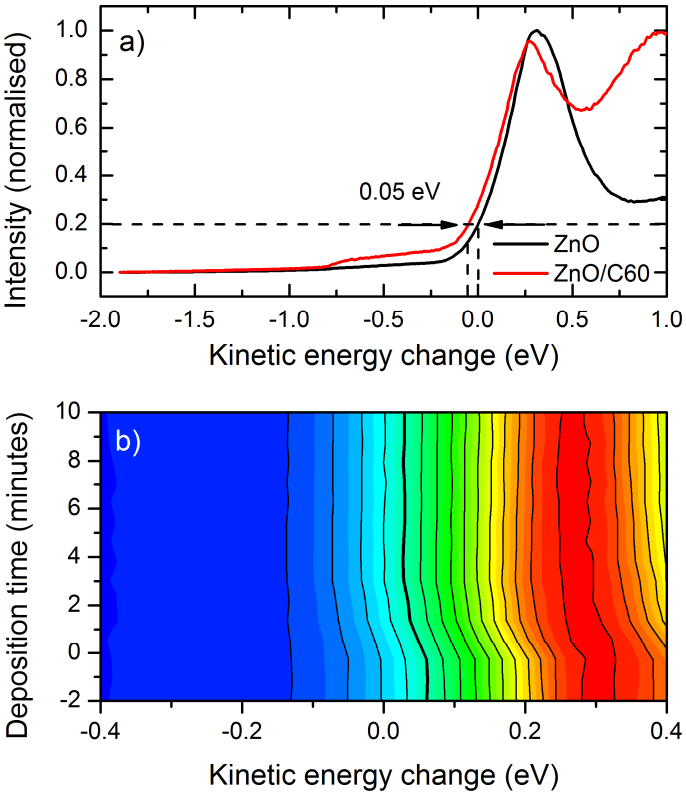

Figure 6.16 Secondary electron cut-off during formation of ZnO(0001)/C60 interface

6.4. Discussion

The organic solvent cleaning procedure produced a clean surface with only 6% detected carbon, better than that reported by Allen et al [27] for a similar ex-situ preparation method where 14% carbon was reported. It is likely that cleaning the entire sample holder with sample affixed rather than cleaning the sample and then affixing it to the sample holder (as is usually done) resulted in lower contamination. The amount of surface hydroxide is also lower than that reported by Coppa et al for their as-loaded samples [41]. Allen et al also reported that 20 minutes of remote oxygen plasma treatment resulted in carbon contamination levels of 2.4%. This is in contrast to 10 minutes of in-situ oxygen plasma treatment which resulted in a surface clean of carbon, also in agreement with Coppa et al [41], highlighting the advantage of in-situ surface processing over ex-situ processing. Experience of using the in-situ oxygen plasma suggests that a few minutes of exposure would be sufficient to remove the surface contaminants.

No effect to the conventional x-ray photoelectron spectrum or the real-time XPS annealing data was observed by not using an indium back contact. Due to the wetting of the sample holders with indium after high temperature annealing and the difficulty in cleaning the sample holders it is preferable to avoid using indium in future.

6.4.1. Surface preparation

Core-level spectra of the (0001) surface after in-situ surface processing revealed an interesting surface chemistry. The as-loaded surface had an O 1s core-level with two components while the Zn $2p_{3/2}$ core-level had two components. Allen et al [27] measured the O 1s core-level of the (0001) and $(000\bar{1})$ surface with soft x-rays and unambiguously

identified a surface and bulk component; bulk at 530.8 eV and a surface 532.3 eV. Kunat et al [32] reported 530.7 eV for the main component in the O 1s core-level of ZnO($000\bar{1}$). These compares perfectly with the measurements and therefore the main O 1s component is assigned as bulk Zn-O and the higher binding energy component as surface hydroxide.

The fitting parameters in Table 6.2 clearly show that the effect of oxygen plasma exposure is to increase the amount of detected zinc and increase the binding energies of the Zn $2p_{3/2}$ and O 1s core-levels.

The Zn/O ratio of the as-loaded surface (0.93 with 6% carbon) is similar to that reported by Allen et al [27] for the remote oxygen plasma treated surface (0.86 with 2% carbon). For the ($000\bar{1}$) surface Allen et al [27] noted that the Zn/O ratio was x1.2 higher than on the (0001) surface. The ($000\bar{1}$) surface measured in this work had been given a 40 minute plasma exposure and annealed at 570 K and a comparison of the Zn/O ratio of this surface (1.47) to the (0001) surface after a similar preparation (1.23) revealed a x1.2 higher ratio, in agreement with Allen et al. The higher Zn/O ratio of the ($000\bar{1}$) surface relative to the (0001) surface is consistent with an oxygen or hydroxyl surface termination, giving (0001):Zn-OH and ($000\bar{1}$):O-H, and a higher Zn/O ratio for the ($000\bar{1}$) surface. This has also been noted by Allen et al [27], and is in agreement with the assignment of the higher binding energy component in the O 1s core-level being hydroxide.

A decrease in the binding energies of both core-levels on the (0001) surface signifies a shift of the Fermi level with oxygen plasma exposure away from the conduction band minimum and closer to the valence band maximum. A maximum shift of -0.5 eV was observed, the shift being exponential with oxygen exposure time as shown in Figure 6.7 panel a). A similar shift has been reported by Coppa et al [41] and Mosbacker et al [42] when (0001) surfaces

were exposed to in-situ oxygen plasma. The surface is also highly sensitive to the presence of adsorbates [6, 43] and below detection limit adsorption of oxygen is possible. After removal of the carbon contamination the only possible interaction between the oxygen plasma and the hydroxyl terminated surface is the removal of hydrogen (in the form of H_2O) leaving :Zn-O, or a sub-surface interaction where oxygen vacancies are filled. Since hydrogen is undetectable in XPS this would be only detectable in the O 1s core-level where a reduction to the hydroxide component and an additional chemically shifted component, O-O, would be expected. Neither is conclusively observed and the ratio of the hydroxide component to the bulk component remains fairly constant at 0.18 ± 0.04. This suggests that if present the chemical change was unresolved within the higher binding energy component. Evidence supporting adsorption of oxygen may be found in the broadening of the O 1s core-level with oxygen plasma exposure, where 1.40 eV was measured for the 10 minute exposed surface compared to 1.49 eV for the 40 minute exposed surface, indicating a slightly more diverse oxygen surface chemistry with increasing exposure time. The filling of sub-surface oxygen vacancies would result in the removal of the n-type characteristic of the surface, the limit of which would be perfectly stoichiometry. The exponential nature of the shift also hints at a saturation of the vacancies within a depth accessible by the activated oxygen. The sub-surface of ZnO is known to have a higher concentration of oxygen defects than the bulk [4] which are believed to be responsible for the n-type characteristic of undoped ZnO.

Turning to the annealed surfaces (both (0001) and $(000\bar{1})$ after oxygen plasma exposure), a dramatic change to the O 1s core-level and the position of the Fermi level occurred while the overall Zn/O ratio remained the same. The Fermi level returned to the original as-loaded position and consequently the mechanism responsible for the shift of the Fermi level was

completely reversed. This is different to the observation of Coppa et al [41] who observed that oxygen plasma exposure at high temperature (800 K), while this work was performed at room temperature, resulted in a lower Zn $2p_{3/2}$ binding energy. It appears that oxygen exposure at elevated temperature results in a more stable surface than exposure at room temperature (this work). The intensity of the hydroxyl component in the O 1s core-level halved compared to the oxygenated surfaces revealing substantial removal of hydroxide. The ratio of the hydroxide component to the main component is lower (0.08) for a surface having been exposed to oxygen plasma for 40 minutes and annealed at 570 K than a surface exposed for 20 minutes then annealed at 720 K (0.11), suggesting that the longer oxygen exposure is responsible, in agreement with Coppa et al [41]. The width of the O 1s core-level for the 40 minute / annealed surface is slightly broader than the 20 minute / annealed surface, 1.55 eV and 1.47 eV respectively, suggesting a slightly more diverse surface oxygen chemistry. These widths are also broader than the minimum measured on the 10 minute oxygen plasma exposed surface (1.40 eV). Hydroxide has been reported to be removed from the (0001) surface at 536 K [31] and the $(000\bar{1})$ surface at 547 K [32], and these values agree with the reduction in hydroxyl observed after annealing at 570 K and above.

The real-time XPS annealing of oxygenated (0001) surfaces revealed a gradual shift of the Zn $2p_{3/2}$ core-level towards higher binding energy, and thus a shift of the Fermi level away from the valence band maximum, with temperature. The gradual shift of the Fermi level with temperature suggest that the oxygen vacancies are extremely mobile and diffuse from the bulk into the sub-surface by annealing. This is consistent with a higher concentration of defects in the sub-surface than in the bulk [4]. The real-time 700 K annealing cycle is reminiscent of the sputtered copper surface in Section 5 and suggests that the completion of

a thermally activated process had completed at 580 ± 20 K. This process is possibly loosely bound hydroxide from the surface. Loosely is used since complete hydroxide removal was not observed indicating that a critical coverage of hydroxide is strongly bound and may be the critical coverage hypothesised to stabilize the (0001) surface. Above this temperature oxygen vacancies diffuse from the sub-surface into the bulk and the binding energy shift of the annealed surface is observed (discussed Section 6.4.2). The real-time 700 K cycle also had an unexpected shift of the Zn $2p_{3/2}$ core-level to lower binding energy at 430 K that was only partially observed on any of the other oxygenated (0001) surfaces. The shift is outside the experimental uncertainty and a possible explanation may be found by noting from the literature that zinc hydride (ZnH) is thermally desorbed at 385 K [32]. While no evidence for the ZnH species is found in the Zn $2p_{3/2}$ core-level, chemical shifts are quite small for the Zn $2p_{3/2}$ [5] and therefore resolving with Mg Kα would not be possible.

6.4.2. Clean (0001) and (000$\bar{1}$) surfaces

The clean (0001) surface (Figure 6.7 panel b), having been processed with in-situ oxygen plasma and annealed above 580 K, exhibited a linear shift of -6.6 meV / 10 K up to 700 K with a slightly more rapid rate of shift at higher temperatures, was symmetrical and also fully reversible. The mechanism behind the shift is difficult to identify. Firstly the effect of contact resistance may be discounted as no effect was found on the real-time XPS annealing if an indium back contact was or was not used. Surface chemistry may also be discounted since the changes are reversible. The bulk resistance of the samples are quite low, 0.3 Ω-cm, and positive sample charging was not expected or observed. The remaining mechanisms are a photovoltage due to irradiation by x-rays, a thermal expansion of the lattice, the diffusion of oxygen vacancies into the sub-surface, and some form of internal charge transfer. Firstly

the material is n-type and a shift towards lower binding energy with temperature, saturating at high temperature, similar to that measured by Long and Bermudez [44] for n-type GaN, and in the opposite direction to a p-type material such as type IIb diamond in Section 6, is expected for n-type materials that have a surface photovoltage. However two observations make this unlikely; no shift was found to the Zn $2p_{3/2}$ core-level binding energy with reduced x-ray flux, and the shift did not exhibit any sign of approaching saturation with temperature (indeed an increase in the gradient at higher temperature was observed). A thermal expansion of the lattice leading to a reduction in core-level binding energy is therefore possible for the (0001) surface, however the diffusion of highly mobile oxygen vacancies, from the sub-surface into the bulk during heating and from the bulk into the sub-surface during cooling, is more likely due to the defective nature of ZnO.

Measurements on the $(000\bar{1})$ surface, which exhibited a markedly different core-level binding energy shift that was non-symmetric yet fully reversible, were different to the (0001) surface and unexpected. A similar mechanism to that on the (0001) surface may not be enough to explain the results. The effect is not due to desorption of surface species since the 700 K cycle measured after the 900 K cycle was effectively the same (during the heating). The shift is reminiscent of a hysteresis loop and suggests that some form of charge transfer was occurring with temperature. The moderate temperature cycle (700 K) shown in Figure 6.7 panel c) is more astonishing than the high temperature cycle (900 K), as 700 K corresponds to the middle of the rapid binding energy decrease of the Zn $2p_{3/2}$ core-level. The shift to lower binding energy continued during cooling, albeit at a much lower rate, and only increased to higher binding energy after the temperature dropped below 410 ± 10 K. This is akin to the surface holding charge and releasing it only when the temperature has

dropped below a critical point. It is also suggested that time is a factor, since the time above a certain temperature drives the core-level shift, and not the actual temperature. This strongly suggests that the charge transfer stabilization mechanism is present on the $(000\bar{1})$ surface, which is disrupted at high temperature. This is in contrast to the (0001) surface where the surface is stable with a hydroxide termination and exhibits a symmetrical binding energy shift with temperature.

The exact nature of the stabilization mechanisms for ZnO surfaces is unknown and these results suggest that a combination of two; hydroxide stabilization and charge transfer stabilization. The charge transfer mechanism appears to be disrupted on the $(000\bar{1})$ surface but not on the (0001) surface. This effect may be extremely useful for first principles analysis of the stabilisation mechanism [5, 29, 45] of ZnO polar surfaces.

A polarity related effect has been noted by Allen et al [27] for ZnO who noted differences in the valence band intensities of (0001) and $(000\bar{1})$ surfaces when measured with Al Kα x-rays at normal emission. They note that the effect may be associated to the lack of inversion symmetry in the wurtzite structure of ZnO and is therefore an intrinsic effect and not a surface chemistry effect. In this work the temperature dependence of the Zn $2p_{3/2}$ binding energy is utterly different for the two polar faces of ZnO, and real-time XPS annealing therefore offers a much simpler method of determining polarity than determining relative intensity of valence band features.

6.4.3. Organic interfaces

ZnO(0001)/CuPc interface

The intensity variation of the substrate core-levels during CuPc deposition is indicative of a layer-by-layer growth mode with a constant deposition rate of 0.19 ± 0.03 nm/min. The precision of the deposition rate is reduced by the uncertainty in the electron attenuation length. The value is derived from Evans et al [38] who monitored substrate core-levels with kinetic energies in the range 700 eV to 1200 eV during deposition of CuPc on InSb. Although an empirical fit is presented for the electron attenuation length variation within this energy range, the Zn $2p_{3/2}$ kinetic energy in this work was 464 eV and outside the Evans data, leading to a conservative uncertainty of 0.2 nm. As the actual deposition rate of CuPc is not known the accuracy of this value cannot be commented upon. However the value is similar to that present in the NIST database for organic compounds [46].

The substrate core-level binding change indicates that some charge transfer of holes from the ZnO to the CuPc layer occurred. The shift was quite small (-80 meV) and occurred during the first minute of exposure to CuPc, corresponding to a thickness of 0.19 nm, and is characteristic of charge transfer. Beyond this coverage the core-level binding energy is constant within the experimental uncertainty. For the overlayer core-levels the binding energy change is more revealing; during the first 15 minutes of deposition (2.85 nm) a shift to lower binding energy is observed in both the C 1s and N 1s core-levels of CuPc of around 200 meV, indicative of band-bending in the overlayer. At coverages beyond 2.85 nm an increase in the core-level binding energy was observed, saturating at 240 meV at full coverage (14 nm). A shift to higher binding energy at increased coverage is characteristic of charging and is expected of thick layers of organic molecules such as CuPc that have low

conductivities. The secondary electron cut-off change during the deposition is also characteristic of interface formation where a rapid change occurred during the first 0.6 nm, corresponding to a monolayer coverage. For coverages greater than this a gradual shift towards lower kinetic energy was observed. As the rate of shift to lower kinetic energy was the same as the core-level shift to higher binding energy, this supports the hypothesis that sample charging was taking place.

The work function change of the (0001) surface with CuPc coverage is the same as that reported in the literature by Komolov et al [47]. Not only is the distinct shape of the work function change the same, but the coverage dependency is also the same; Komolov reports the work function to reach a minimum at 3 nm at to be saturated by 6 nm, and in this work the work function minimum was at 3.8 nm and saturation occurred at 5.7 nm.

The work function of the (0001) surface is indicated to be 5.0 eV from this measurement and this is in agreement with Komolov et al [47] and Allen et al [25]. This is therefore not in agreement with the reports in the literature that the (0001) surface has a low work function, however this is possibly due to differences in the bulk and surface properties of the samples.

ZnO(0001)/C60 interface

The substrate core-level attenuation during deposition of C60 on ZnO was not indicative of layer-by-layer growth but of Stranski-Krastanov growth. Following opening of the shutter a rapid attenuation was measured, corresponding to a deposition rate of 0.11 ± 0.02 nm/min. After 5 minutes of deposition (0.55 nm) the attenuation rate decreased and the decreased attenuation rate was maintained throughout the remaining deposition. The deposition rate during the first 5 minutes agrees with that measured in Section 4 where C60 was deposited

on Al, giving confidence that layer-by-layer growth was observed for the first 5 minutes. A total coverage of 4 nm is calculated taking the reduced attenuation into account.

For the growth mode to change this suggests that some form of chemical reaction had taken place between the C60 and the ZnO, and this is supported by the unusual C 1s core-level measured at the completion of the deposition (Figure 6.14). The C 1s core-level could not be fitted with a single component and associated plasmon structure (as in Section 3), and an additional component was required. The assignment of this component proved difficult at first since some oxygen had been detected in the interface (Figure 6.13). However some zinc is also measured and within the experimental uncertainty the Zn/O ratio is unity and is present due to the overlayer coverage being comparable to the probing depth (3λ). The additional component in the C 1s core-level is due to chemically bonded C60 and this was proven by careful fitting of the C 1s core-level and plasmon structure. In panels b) and c) of Figure 6.14 the effect of incorporating the distinct plasmon structure to only one and to both the components is shown. The fits conclusively show that plasmon structure is required of both components, and therefore two distinct C60 spectra are present. This also proves that whatever chemical reaction occurred at the interface the C60 molecular structure was preserved, since a carbon signal without plasmon structure would else have been expected.

It is interesting to note that the dominant C60 component had a binding energy of 284.6 eV while the smaller C60 component had a binding energy of 285.0 eV; pristine C60 has been measured in Section 3 and shown to have a binding energy of 285.0 eV. A possibility therefore is that pristine C60 was deposited on the surface for the first 5 minutes leading to the component in the C 1s core-level at 285.0 eV. Following this a change to the growth

mode occurred with the C60 in island configuration being in a chemically shifted environment.

It was extremely difficult to fit the C 1s core-level snapshots at low coverages to ascertain which chemical species were present. However above 7 minutes exposure a two component fit was obvious and the relative ratios were preserved throughout the deposition. Since the relative intensity of both is maintained C60 must have continued to be in two chemical environments. This is possible as an island growth mode was observed allowing the first layer of pristine C60 to continue to grow.

Such a complicated chemistry was not expected since perfect layer-by-layer growth was observed on aluminium (with oxide layer) in Section 4 where a C 1s core-level and plasmon structure characteristic of pristine C60 was measured. This therefore suggests that the hydroxide on the ZnO surface was responsible for the different chemistry and not oxygen.

The substrate and overlayer binding energy shift during deposition was quite simple; no change was observed to the substrate core-level within the experimental uncertainty, while a large 0.36 eV shift to lower binding energy was observed to the overlayer core-level. The secondary electron cut-off change was also simple with a small 0.05 eV shift occurring throughout the deposition. This is evidence against a chemical reaction occurring since a more significant change would be expected.

The work function change of the ZnO surface with C60 coverage was -0.41 eV giving a (0001) work function of 5.13 eV. This value is similar to the 5.0 eV determined for the same surface with CuPc deposition, giving confidence that the surface preparation of the (0001) surface leads to a high work function surface.

6.4.4. Energy band diagrams

Having determined the change to the Fermi level for different surface preparations and at different temperatures for the (0001) and $(000\bar{1})$ surfaces, and having determined the work function of the (0001) surface from the formation of an interface with CuPc, band-diagrams may be drawn. Figure 6.17 shows the band diagram for the clean (0001) surface (oxygen plasma and annealed above 580 K) and two possible band-diagrams for the (0001) surface after 40 minutes of oxygen plasma exposure. Assuming the bulk Fermi level position does not change the effect of the oxygen plasma is to shift the position of the Fermi level above the valence band maximum from 3.61 eV to 3.16 eV, and consequently change the 0.34 eV of downwards band bending to 0.11 eV upwards band bending. This change is significant as the Fermi level is now below the conduction band minimum at the surface and therefore the surface should not exhibit electron accumulation. However this situation should not be taken implicitly since the position of the valence band maximum has not been measured merely inferred from the core-level binding energy change. As mentioned previously the position of the bulk Fermi level in undoped ZnO is determined by oxygen vacancies and these were found to be highly mobile. It is therefore likely that the position of the bulk Fermi level changed and thus inferring the valence band maximum position is incorrect. Assuming that saturated oxygen plasma exposure leads to perfect stoichiometry at the surface and therefore to flat-band condition the shift to the bulk Fermi level can be estimated. The two band-diagrams therefore are at the two possible extremes for the surfaces measured.

The work function of the oxygen plasma exposed surface is unknown however it is generally observed that adsorption of oxygen increases the work function and therefore a value greater than 4.5 eV is expected.

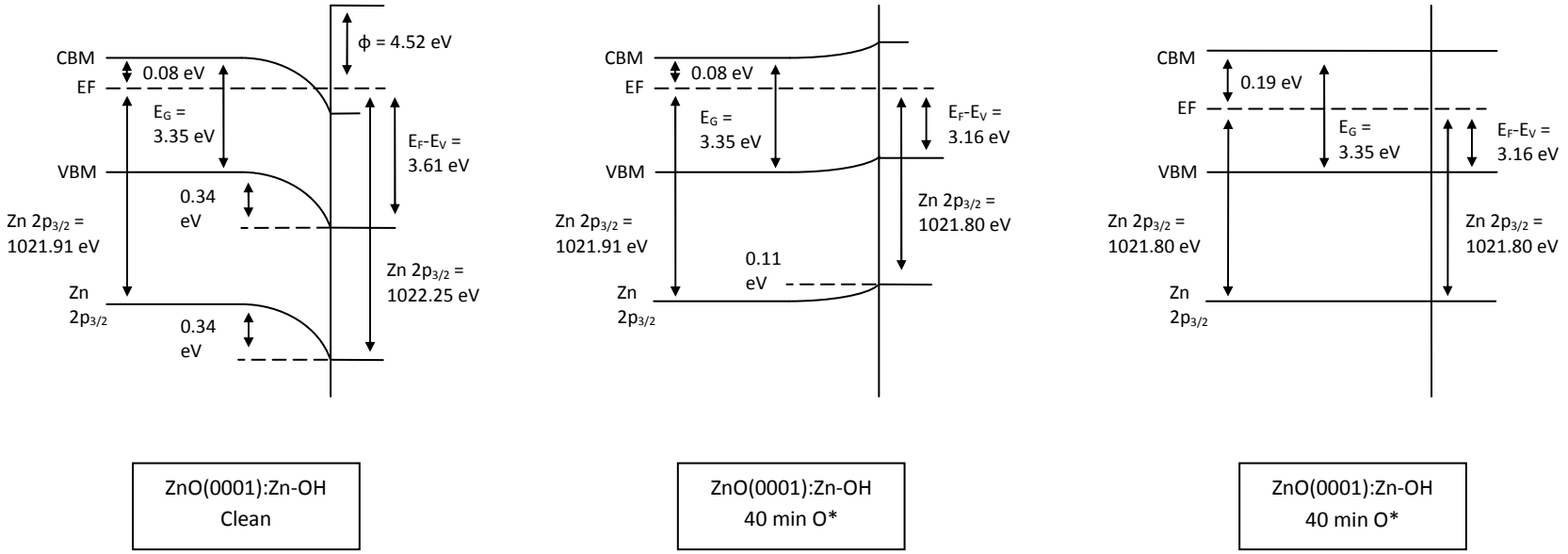

Figure 6.17 Band diagrams for the clean (0001) surface and after oxygen plasma exposure. The same bulk Fermi level position has been used for the plasma exposed surface.

6.5. Future work

The filling of oxygen vacancies with oxygen plasma exposure could be further investigated by investigating low defect samples. This may allow a thermally stable surface to be prepared that maintains the low binding energy Zn 2p core-level after annealing. It may also be possible to perform the oxygen plasma treatment at high temperature allowing oxygen vacancies to be mobile and filled during the treatment. This may produce different real-time XPS annealing results which may be of great assistance in elucidating the mechanisms at work.

Measuring the position of the valence band maximum would be extremely useful for determining the position of the Fermi level in the samples after oxygen plasma treatment. The use of ultraviolet photoelectron spectroscopy would allow the valence band edge to be measured and also the work function of the surfaces to be determined.

An optical measurement of the defects may be of assistance in determining concentration changes after surface processing. X-ray luminescence has been observed from the ZnO and a monitoring changes to the emission spectrum after surface processing would be of assistance in determining changes to sub-surface defects.

6.6. References

1. Ashrafi, A. and C. Jagadish, *Review of zincblende ZnO: Stability of metastable ZnO phases.* Journal of Applied Physics, 2007. **102**(7): p. 071101-12.
2. Look, D.C., J.W. Hemsky, and J.R. Sizelove, *Residual Native Shallow Donor in ZnO.* Physical Review Letters, 1999. **82**(12): p. 2552.
3. Ozgur, U., et al., *A comprehensive review of ZnO materials and devices.* Journal of Applied Physics, 2005. **98**(4): p. 041301-103.
4. Brillson, L.J., et al., *Massive point defect redistribution near semiconductor surfaces and interfaces and its impact on Schottky barrier formation.* Physica B: Condensed Matter, 2009. **404**(23-24): p. 4768-4773.
5. Wöll, C., *The chemistry and physics of zinc oxide surfaces.* Progress in Surface Science, 2007. **82**(2-3): p. 55-120.
6. Hishinuma, N., *High-sensitivity ZnO-semiconductor detector for atomic hydrogen beams.* Review of Scientific Instruments, 1981. **52**(2): p. 313-314.
7. Bagnall, D.M., et al., *Optically pumped lasing of ZnO at room temperature.* Applied Physics Letters, 1997. **70**(17): p. 2230-2232.
8. Alivov, Y.I., et al., *Observation of 430 nm electroluminescence from ZnO/GaN heterojunction light-emitting diodes.* Applied Physics Letters, 2003. **83**(14): p. 2943-2945.
9. Alivov, Y.I., et al., *Photoresponse of n-ZnO/p-SiC heterojunction diodes grown by plasma-assisted molecular-beam epitaxy.* Applied Physics Letters, 2005. **86**(24): p. 241108-3.
10. Tadatsugu, M., *Transparent conducting oxide semiconductors for transparent electrodes.* Semiconductor Science and Technology, 2005. **20**(4): p. S35.
11. Repins, I., et al., *19.9%-efficient ZnO/CdS/CuInGaSe2 solar cell with 81.2% fill factor.* Progress in Photovoltaics, 2008. **16**(3): p. 235-239.
12. Leschkies, K.S., et al., *Photosensitization of ZnO nanowires with CdSe quantum dots for photovoltaic devices.* Nano Letters, 2007. **7**(6): p. 1793-1798.
13. Meng, Q.B., et al., *Fabrication of an efficient solid-state dye-sensitized solar cell.* Langmuir, 2003. **19**(9): p. 3572-3574.
14. Law, M., et al., *ZnO-Al2O3 and ZnO-TiO2 core-shell nanowire dye-sensitized solar cells.* Journal of Physical Chemistry B, 2006. **110**(45): p. 22652-22663.
15. White, M.S., et al., *Inverted bulk-heterojunction organic photovoltaic device using a solution-derived ZnO underlayer.* Applied Physics Letters, 2006. **89**(14): p. 143517-3.
16. Beek, W.J.E., et al., *Hybrid zinc oxide conjugated polymer bulk heterojunction solar cells.* Journal of Physical Chemistry B, 2005. **109**(19): p. 9505-9516.
17. Chen, C.-T., et al., *The effect of C60 on the ZnO-nanorod surface in organic-inorganic hybrid photovoltaics.* Solar Energy Materials and Solar Cells, 2011. **95**(2): p. 740-744.
18. Santanu, K. and M. Biswanath, *Nanostructured organic–inorganic photodiodes with high rectification ratio.* Nanotechnology, 2008. **19**(49): p. 495202.
19. Liu, J.P., et al., *Inverted photovoltaic device based on ZnO and organic small molecule heterojunction.* Chemical Physics Letters, 2009. **470**(1-3): p. 103-106.
20. Sharma, G.D., et al., *Charge generation and photovoltaic properties of hybrid solar cells based on ZnO and copper phthalocyanines (CuPc).* Solar Energy Materials and Solar Cells, 2006. **90**(7-8): p. 933-943.
21. Wolf, S.A., et al., *Spintronics: A Spin-Based Electronics Vision for the Future.* Science, 2001. **294**(5546): p. 1488-1495.
22. Pearton, S.J., et al., *Wide band gap ferromagnetic semiconductors and oxides.* Journal of Applied Physics, 2003. **93**(1): p. 1-13.
23. Katsumi, M. and et al., *Growth of 2 inch ZnO bulk single crystal by the hydrothermal method.* Semiconductor Science and Technology, 2005. **20**(4): p. S49.

24. Nause, J. and B. Nemeth, *Pressurized melt growth of ZnO boules.* Semiconductor Science and Technology, 2005. **20**(4): p. S45.
25. Allen, M.W., et al., *Bulk transport measurements in ZnO: The effect of surface electron layers.* Physical Review B, 2010. **81**(7): p. 075211.
26. Tasker, P.W., *The stability of ionic crystal surfaces.* Journal of Physics C: Solid State Physics, 1979. **12**(22): p. 4977.
27. Allen, M.W., et al., *Polarity effects in the x-ray photoemission of ZnO and other wurtzite semiconductors.* Applied Physics Letters, 2011. **98**(10).
28. Wander, A., et al., *Stability of Polar Oxide Surfaces.* Physical Review Letters, 2001. **86**(17): p. 3811.
29. Dulub, O., U. Diebold, and G. Kresse, *Novel stabilization mechanism on polar surfaces: ZnO(0001)-Zn.* Physical Review Letters, 2003. **90**(1).
30. Kresse, G., O. Dulub, and U. Diebold, *Competing stabilization mechanism for the polar ZnO(0001)-Zn surface.* Physical Review B, 2003. **68**(24): p. 245409.
31. Becker, T., et al., *Interaction of hydrogen with metal oxides: the case of the polar ZnO(0 0 0 1) surface.* Surface Science, 2001. **486**(3): p. L502-L506.
32. Kunat, M., et al., *Stability of the polar surfaces of ZnO: A reinvestigation using He-atom scattering.* Physical Review B, 2002. **66**(8): p. 081402.
33. Schiek, M., et al., *Water adsorption on the hydroxylated H-(1x1) O-ZnO(0001bar) surface.* Physical Chemistry Chemical Physics, 2006. **8**(13): p. 1505-1512.
34. Tampo, H., et al., *Determination of crystallographic polarity of ZnO layers.* Applied Physics Letters, 2005. **87**(14): p. 141904-3.
35. Ohnishi, T., et al., *Determination of surface polarity of c-axis oriented ZnO films by coaxial impact-collision ion scattering spectroscopy.* Applied Physics Letters, 1998. **72**(7): p. 824-826.
36. Wikipedia commons. *Wurtzite polyhedra*. Available from: http://commons.wikimedia.org/wiki/File:Wurtzite_polyhedra.png.
37. Møller, P.J., et al., *Oxygen effect on the conductivity of the CuxO/ZnO(0001) and (0001) systems.* Applied Surface Science, 1999. **142**(1-4): p. 210-214.
38. Evans, D.A. and et al., *Copper phthalocyanine on InSb(111)A—interface bonding, growth mode and energy band alignment.* Journal of Physics: Condensed Matter, 2003. **15**(38): p. S2729.
39. Li, H.-N., X.-X. Wang, and W.-F. Ding, *Electron attenuation lengths in fullerene and fullerides.* Journal of Electron Spectroscopy and Related Phenomena, 2006. **153**(3): p. 96-101.
40. Molodtsova, O.V. and M. Knupfer, *Electronic properties of the organic semiconductor interfaces CuPc/C60 and C60/CuPc.* Journal of Applied Physics, 2006. **99**: p. 053704.
41. Coppa, B.J., et al., *In situ cleaning and characterization of oxygen- and zinc-terminated, n-type, ZnO{0001} surfaces.* Journal of Applied Physics, 2004. **95**(10): p. 5856-5864.
42. Mosbacker, H.L., et al., *Role of near-surface states in ohmic-Schottky conversion of Au contacts to ZnO.* Applied Physics Letters, 2005. **87**(1): p. 012102-3.
43. Heiland, G. and P. Kunstmann, *Polar surfaces of zinc oxide crystals.* Surface Science, 1969. **13**(1): p. 72-84.
44. Long, J.P. and V.M. Bermudez, *Band bending and photoemission induced surface photovoltages on clean n- and p-GaN (0001) surfaces.* Physical Review B, 2002. **66**: p. 121308.
45. Meyer, B., *First-principles study of the polar O-terminated ZnO surface in thermodynamic equilibrium with oxygen and hydrogen.* Physical Review B, 2004. **69**(4): p. 045416.
46. Powell, C.J. and A. Jablonski (2011) *NIST Electron effective attenuation length database*.
47. Komolov, A.S. and P.J. Møller, *Electronic charge distribution at interfaces between Cu-phthalocyanine films and semiconductor surfaces.* Surface Science, 2003. **532-535**: p. 1004-1010.

7. Summary and conclusions

A greater understanding of three materials; metals, boron-doped diamond and intrinsic zinc oxide, has been achieved by monitoring annealing and thin-film deposition.

Clean copper and gold surfaces were found to exhibit a temperature dependent core-level binding energy shift that was fully reversible and symmetric with heating and cooling. The mechanism was identified as a thermal expansion of the metal lattice leading to a change to the local potential and a perturbation to the core-level binding energy. The measurement offers the possibility of measuring lattice expansion of polycrystalline metals with x-ray photoelectron spectroscopy and may prove to be a powerful probe of metals and alloyed metals. The removal of argon ion induced damage to the copper surface was observed for the first time and a critical temperature of 680 ± 20 K was determined.

Hydrogen and oxygen terminated surfaces of boron doped (111) diamond were found to have a large surface photovoltage resulting in erroneously low C 1s binding energies and broadened FWHM being reported at room temperature. Measuring the surface at high temperature allowed the actual binding energies and FWHM to be determined. The presence of the photovoltage was verified by performing measurements at elevated temperatures, with variable x-ray flux and by depositing thin-films of silver. The persistence of the surface photovoltage was identified to be due to the bulk resistance of the diamond and this was successfully incorporated into a model that predicted the temperature-dependence of the surface Fermi level.

Zinc oxide (0001) surface was exposed to oxygen plasma and a shift of the Fermi level towards the valence band edge was measured that was dependent on the exposure time.

Saturation of the shift was observed and the mechanism was identified as a filling of sub-surface oxygen vacancies. The clean (0001) surface was found to exhibit a temperature-depended Fermi level shift that was reversible and symmetrical with heating and cooling. The mechanism was identified as being due to the diffusion of oxygen vacancies into the bulk at elevated temperature leading to a reduction in vacancies in the sub-surface. The clean $(000\bar{1})$ surface was found to exhibit a different temperature-dependent Fermi level shift that was reversible but not symmetric with heating and cooling. The mechanism was identified as being a disruption of a charge transfer mechanism that stabilizes the surface. This different temperature-dependence of the polar surfaces allows the surface polarity to be determined much easier than other methods currently known. The formation of an interface with copper phthalocyanine (CuPc) and buckminsterfullerene (C60) was measured revealing layer-by-layer growth of CuPc and island growth of C60. C60 was found to be in two distinct chemical environments at the surface.

Real-time XPS has been shown to be an extremely powerful technique capable of monitoring annealing and thin-film deposition. The analysis chamber was setup to allow the monitoring of annealing up to 1200 K and the deposition of three k-cell sources without the need to move the sample. The ability to alternate between conventional XPS and real-time XPS without the need to move the sample, change the electron analyser settings or x-ray gun flux was found to be extremely important in terms of reliability and confidence in the data. The fitting routine used in CasaXPS to fit the hundreds of snapshots collected during an annealing cycle was fast and easy to use. Collecting ancillary data during real-time monitoring (temperatures, pressure, heater voltage and current) was extremely useful in the data analysis.

An in-situ microwave plasma was built for activated gas processing of solid surfaces. Activated oxygen was used for preparing surfaces clean of contamination, terminating (111) diamond, and filling sub-surface oxygen vacancies in zinc oxide. Activated hydrogen was used for preparing hydrogen terminated (111) diamond.